Superconducting Electromechanical and Nanophotonic Devices for Quantum Measurement and Conversion

Thesis by

Mahmoud Kalaee

In Partial Fulfillment of the Requirements

for the Degree of

Doctor of Philosophy

California Institute of Technology

Pasadena, California

2019

(Defended August 27, 2018)

Acknowledgements

To my advisor, Oskar Painter, who guided me and supported me throughout my grad school. It has not been an easy journey. There were lot of ups and downs and it was your brilliance and encouragement that helped me shape what I have achieved. Thank you.

To Taofiq Paraiso, my first mentor in Painter's group. It was you who eased my way into the group and helped me function in the lab. To Johannes Fink. I'll never be able to thank you enough for mentoring me and supporting me as I came up to speed on working with superconducting microwave circuits, fabrication and cryogenic measurements. This thesis literally would not have been possible without you. To Paul Dieterle and your aptitude for hard work. I am fortunate to have had the opportunity to work with you as we developed the SOI process together. To Mohammad Mirhosseini, for being patient with me and helping through the hardships of these past two years. To Barry Baker for being supportive and the go-to guy when we needed something for the lab. To Gregory MacCabe, for being supportive when I needed his help. To Hengjiang (Jared) Ren for putting up with my incessant (sometimes inappropriate) sarcasm. I was also particularly lucky to work along side an amazing group of people where I consider them to be very good friends. It's been an honor for me. Thank you all present and past Painter group members: Alessandro Pittanti, Mathew Matheny, Alex Krause, Tim Blasius, Justin Cohen, Sean Meenehan, Kejie Fang, Andrew Keller, Micheal Fang, Vinicius Ferreira, Eunjong Kim, Jie (Roger) Luo, Szilard Szoke, Xueyue (Sherry) Zhang, Jash Banker and Hannes Pfeifer. I also have to acknowledge Oskar's first generation of student who helped build up the cleanroom and the labs. None of the work that I have done would be possible without my ability to walk into lab which already ran like a clock work.

To my family for your unconditional love and support. Mom and Dad thank you for always believing in me and shaping me into the person that I am today. Without your encouragement to pursue my goals, I would never have achieved what I have today. To Laleh, without whom I might

not have made it through these last several years without your love and companionship. I don't know what I did to deserve you.

Abstract

Microscale and nanoscale mechanical resonators have been used in advanced technological applications, from high precision time keeping and mass sensing, to processing high frequency signals in mobile communications. In the last few decades, they have been an important part of progress in the field of quantum information and metrology and have been proposed as quantum memories or transducers for measuring or connecting different types of quantum systems.

The field of cavity optomechanics and electromechanics is concerned with coupling the electromagnetic field of a resonant optical cavity or electrical circuit to mechanical motion. These systems provide potential means to control and engineer the state of a mechanical object at the quantum level. This thesis contains the description of mechanical systems in megahertz to a few hundred megahertz frequency range formed by nano-fabricating photonic, phononic, and electrical circuits on a chip. These structures are designed to provide a large radiation pressure coupling between mechanical motion and electromagnetic fields to address and manipulate motional degrees of freedom. Qualitatively novel quantum effects are expected when one takes a step beyond linear coupling and exploits higher order interactions. To that end, we integrate electrical, mechanical and photonic structures in a multimode photonic crystal structure to observe "x^2-coupling", where the optical cavity frequency is coupled to the square of the mechanical displacement. Moreover, we have developed two integrated on-chip platforms based on Si_3N_4 and Si nanomembranes capable of interfacing superconducting qubits and optical photons and realizing reversible microwave-to-optical conversion. We employ radiation pressure to cool these mechanical resonators to their quantum ground state. Finally, we demonstrate a form of electromechanical crystal for coupling microwave photons and hypersonic phonons of frequency $\omega_m/2\pi = 0.425$ GHz by capacitively coupling a phononic crystal acoustic cavity to a superconducting microwave resonator. Moving to higher frequency acoustic cavities not only facilitates the integration of electromechanical circuits and nanophotonic systems

capable of operation in the resolved sideband limit of optomechanics for noise-free quantum signal conversion, but it opens up the possibility of using phonons as information carriers via phononic circuits. Utilizing a two-photon resonance condition for efficient microwave pumping and phononic bandgap shield to eliminate acoustic radiation, we achieve large cooperative electromechanical coupling ($C \approx 30$) and intrinsic decay time of 2.3 ms. Moreover, electrical read-out of the phonon occupancy shows that the acoustic mode thermalizes close to its quantum ground-state of motion (phonon occupancy $n_m = 1.5$) at a fridge temperature of $T_f = 10$ mK. We conclude by considering several designs and fabrication improvements to the hypersonic electromechanical crystals that would enable them to perform quantum conversion between the electrical and acoustic domain.

Contents

List of Figures

Chapter 1

Introduction

1.1 Radiation Pressure

The exertion of the force upon the reflection of light from an object is termed radiation pressure. This is an intriguing concept which was first proposed by Kepler in the 17th century as an explanation for the orientation of comet tails. The tails, which are made from gas and debris separated from the comet nucleus, are observed to always point away from the sun due to the forces from the solar radiation [1]. Later, this phenomenon was quantified via the Maxwells equations [2] of electromagnetism and was later included into Einstein's formulation of special relativity. However, the radiation pressure was considered a weak, perturbative effect the most context. The first unambiguous experimental demonstrations of radiation pressure force were performed by Nichols-Hull and Lebedew [3,4] due to the required analysis for distinguishing the phenomenon from the thermal effect which dominated the previous experiments. This consideration changed with the advent of the laser in the field of optics. With the large and coherent optical powers made available by optical lasers, the radiation pressure found its applications in several aspects, such as trapping and controlling of dielectric particles [5], cooling atomic motion [6], and precision measurement of gravitational field in LIGO.

Later, in what would prove to be a groundbreaking experiment in the field of optomechanics, Braginsky et al. demonstrated the role of radiation pressure and its ability to provide cooling of a mechanical object coupled to an optical resonator [7,8]. In later experiments, these phenomena were also observed for microwave coupled mechanical resonators [9]. Following that, Bragisnky, Caves, and colleagues developed a framework to address the limits imposed by quantum fluctuations in ra-

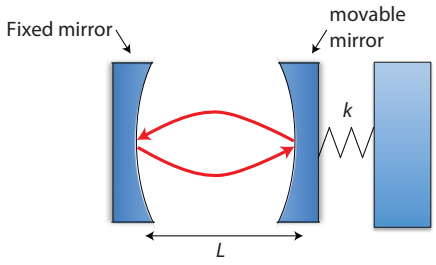

Figure 1.1: This example optomechanical system consists of a Fabry-Perot optical cavity formed from two high-reflectivity mirrors. One mirror is kept fixed, while the other is free to move with mechanical properties modeled by an effective spring force. Displacements of the movable mirror change the optical cavity length L, with a corresponding shift to the optical resonance frequency.

diation pressure on how accurately the position of a mechanical resonator can be measured [10–12]. The interest in where a mechanical oscillator interacts with the electromagnetic field of an optical or microwave cavity escalated with the development of micro- and nano-fabrication processes which allowed us to exploit the nondissipative radiation pressure force for applications in fundamental studies of quantum mechanics, quantum information processing, and precision sensing.

1.2 Optomechanical and Electromechanical Coupling

The basic optomechanical system consists of a mechanical oscillator coupled to an optical field. As an example, consider an optical field bouncing off of a mirror attached to a mechanical oscillator. The phase of the reflected wave is very sensitive to the mechanical displacement; thus, a sensitive readout of the reflected phase allows sensitive inference of the mechanical position. This interaction, and thus the sensitivity of readout, can be enhanced by coupling the mechanical motion to a high-Q electromagnetic resonance, and thus increasing the strength of the interacting field. This situation is shown in Fig. 1.1, where a movable mirror is placed at distance L from a fixed mirror. The motion of the movable mirror modulates the optical path length L of the Fabry-Perot cavity and therefore changes the fundamental resonance frequency of the optical cavity defined by $f_o = c/2L$, where c is the speed of light. Thus for intracavity light with a particular wavelength, the motion of the mirror imparts a shift in both the optical intensity and phase. Furthermore, since reflection of light from the mirror surface exerts a force due to radiation pressure, the optical field, in turn, modulates

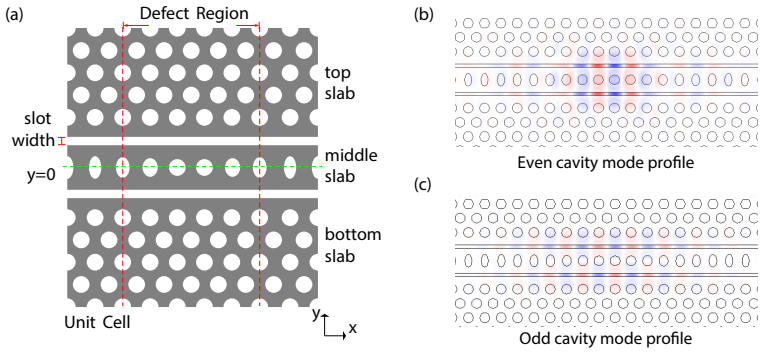

Figure 1.2: **a,** Schematic of a photonic crystal implementation of a multimode optomechanical system. The structure consists of a pair of top and bottom photonic crystal slabs which are separated from a central photonic crystal slab by nanoscale air slots. A pair of optical waveguide modes localizes around each nanoscale slot, propagating along the axial direction (x) of the structure. By varying the photonic crystal unit cell along the length of the structure, one can form optical cavity modes which are localized to a central "defect" region of the structure. **b,** Plot of the FEM-simulated amplitude of the y-polarization of the electric field of the even cavity mode. **c,** Plot of the FEM-simulated y-polarized electric field of the odd cavity mode.

the mirror position. Many optomechanical experiments rely on the canonical optical setup of a Fabry-Perot resonator as shown in Fig. 1.1 with a movable mirror [13–15]. However, these are not the only ways to realize the coupling of the mechanical motion to the resonant frequency of an electromagnetic resonant structure. An example that employs novel coupling mechanisms can be seen in Refs. [16–23] where the mechanical motion changes the capacitance of an LC circuit (Electromechanics) and therefore the resonance frequency, imparting a phase shift on the outgoing electric fields. Another example employs the patterning of a dielectric material such as Si to confine and co-localize a mechanical resonance and optical fields (Optomechanical crystals) can be seen in Refs. [13, 24–26]. While each implementation features unique advantages and disadvantages, this thesis focuses first on optomechanical devices for their high degree of tailorability and ability to support large mechanical frequencies, and electromechanical devices second due to their access to low loss superconducting circuits and non-linear elements such as Josephson-junctions in circuit QED toolbox for quantum information processing.

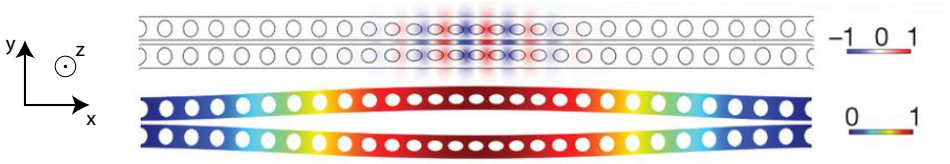

Figure 1.3: Top: FEM simulation showing the in-plane electrical field of the fundamental optical cavity mode. Bottom: FEM simulation of the displacement of the fundamental in-plane differential mode of the structure. The mechanical motion, modifying the gap between the beams, shifts the optical cavity frequency, leading to optomechanical coupling.

1.2.1 Optomechanical Devices

In analogy with electron bands for the electron waves propagating in a lattice, periodic modulation of the index of refraction of a dielectric material, such as Si, leads to the formation of optical bands and band gaps. In these structures, light cannot propagate in the band gaps. Introducing an artificial defect in these periodic structure localizes the electromagnetic field in the defect region which cannot propagate into the continuum inside the structure. These structures are called photonic crystal cavities. If the photonic crystal structure is mechanically compliant, the mechanical motion results in modulations of the optical cavity boundaries and stresses in the material, both of which contribute to modulation in the effective dielectric constant of the optical mode and shifting the frequency of the optical cavity. This leads to a coupling between the phase and intensity of the optical fields and the mechanical motion.

In this work, we fabricate a quasi two-dimensional (2D) photonic crystal structure to create an optical cavity supporting a pair of high-Q optical resonances in the 1500 nm wavelength band (see Fig. 1.2). A two triangular array of circular holes is etched to the top and bottom slabs that are separated by two nanoscale cuts from the central nanobeam which consists of elliptical holes. The index variation in the structure from the etched holes and the nano-scale cuts, confines, and localizes the optical modes in the air slots in the middle of the defect region. The index variation can be seen in Fig. 1.2 (a) as $n_{\mathrm{Si}} = 3.48$ for the gray region, while white regions represent air or vacuum. All three slabs of the structure are undercut and mechanically compliant. The mechanical resonance of the silicon slabs modulates the boundaries of the optical modes and couples the mechanical motion to the optical resonances.

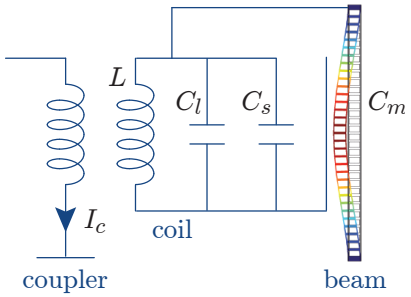

Figure 1.4: Electrical circuit diagram, where the circuit is inductively coupled to the feed line, L is the inductance of the circuit, C_l, C_s are capacitances of the circuit and C_m is the motional capacitance. The exaggerated simulated displacement of a mechanical mode of dielectric beam is shown.

Another type of optomechanical device used in this work (see Chapter 6) is the double-nanobeam or zipper optical cavity (see Fig.1.3), which is made of silicon and consists of two nanobeams, each supporting an optical mode placed side-by-side in y direction. For sufficiently small air-gap between the two nanobeams, the single-beam modes hybridize into coupled modes shared between both nanobeams. In particular, one of the hybridized modes would have large optical intensity in the airgap leading into large optomechanical coupling between the hybridized mode and the differential mechanical mode of the nanobeams.

1.2.2 Electromechanical Devices

As introduced at the beginning of this chapter, optical fields are not the only way to realize coupling of the mechanical motion to resonant frequency of an electromagnetic structure. In comparison to the canonical Fabry-Perot cavity, where the mechanical motion changes the effective length of the optical cavity and shifts the optical resonance frequency, in the electromechanical system, the mechanical motion can be used to change the capacitor gap of an LC resonant circuit and once again shifts the resonance frequency of the circuit. The electromechanical system studied in this work is formed by a dielectric mechanical oscillator capacitively coupled to a superconducting microwave resonant circuit in such a way that the mechanical motion modulates the capacitance gap (see Fig.1.4). There are two unique advantages to these electromechanical systems. First, the substrate is a dielectric material. Our interest in using thin film dielectric material stems from the fact that these materials can be patterned to simultaneously co-localize an optical mode and high frequency mechanical mode

for an on-chip integration with superconducting circuits. Second, the resonant microwave circuit is mechanically supported by a thin-film membrane, reducing the overall parasitic capacitance of the microwave circuit. Moreover, out of many ways to realize a resonant circuit in the microwave regime such as quarter or half wave coplanar waveguides, we utilize lumped element components which can either capacitively or inductively couple to other microwave elements. This work and the bulk of my thesis focuses on lumped element high impedance spiral microwave resonators due to their low loss, compact geometry, and minimal capacitance.

1.3 Quantum applications of Electromechanical and Nanophotonic devices

One of the key goals in quantum information processing is to develop an efficient link between disparate quantum processing units. In this regard, optical signals propagating in optical fibers, particularly in the telecom band, are proposed as a communication channel to link different quantum processing units. This is especially interesting in the context of providing an optical interface for the superconducting quantum circuits given the tremendous success of circuit QED systems. Mechanical systems have the potential as an intermediary between these otherwise incompatible quantum systems. Electromechanics and optomechanics can provide efficient means of conversion between different electromagnetic wavelength, utilizing a common mechanical oscillator to connect two optical and microwave cavities. The mechanism has already been proposed in Ref. [27], and optical to optical wavelength conversion [28] and microwave to microwave frequency conversion [29] as well as reversible optical to microwave conversion at the classical level [30] have been demonstrated. However, it still remains an open challenge to demonstrate optical to microwave frequency conversion at the single photon level. One necessary requirement for quantum limited wavelength conversion is to achieve a large cooperative regime where the rate of interaction between the electromagnetic cavities and the mechanical oscillator is more than the losses. Another requirement is to prepare the mechanical resonator in the quantum regime (*i.e.*, ground state). Moreover, the mechanical resonator needs to operate in the resolved sideband limit of the two cavities [13].

Another example of application of the mechanical resonator in the quantum regime is their potential for storage of quantum states due to their long coherence times. Moreover, mechanical ele-

ments are more compact compared to their electromagnetic counterparts owing to the factor of 10^5 difference in the speed of light and speed of sound in solid state materials.

1.4 Thesis Outline and Structure

My work in the field of optomechanics and electromechanics has primarily involved the development of several micro- and nano-scale device technologies based upon the silicon (Si) and silicon-nitride (Si_3N_4) materials platform. Below I provide a brief description of the various device projects I was involved with and an outline of the corresponding chapters in this thesis that deal with each type of device.

In Chapter 2, I begin with a description of a two-dimension (2D) photonic crystal cavity structure that is designed to achieve large position-squared optomechanical coupling, which is particularly interesting in the context of realizing quantum non-demolition measurement (QND) of phonon number [31–33]. Although the use of x^2-coupling to prepare the mechanical object in a nonclassical state remains an elusive goal due to the small coupling rate to the motion of the mechanical resonator, we demonstrate position squared coupling which is five orders of magnitude higher than Fabry-Perot membrane-in the-middle systems [34] and more than two orders of magnitude larger than volume fiber-gap cavities [35]. Moreover, with this scale of x^2 coupling it is feasible to consider a number of other interesting experiments such as quantum measurement of phonon and photon shot noise [36], or utilizing the interference of quantum noise in the bad cavity limit [37].

The bulk of this thesis deals with integrating superconducting microwave circuits with mechanical objects. In this regard, I have developed two electromechanical platforms, one based on Si_3N4 nanomembranes and the other based on silicon-on-insulator, and both capable of integration with optomechanical devices. Both electromechanical platforms utilize planar capacitors with vacuum gaps of a width of tens of nanometers and high impedance superconducting spiral inductor coils of micron pitch critical for realizing efficient coupling to mechanical motion. I will begin by summarizing the theoretical framework used to describe cavity electromechanical systems in Chapter 3. In Chapter 4, I will present our results with silicon nitride nano-membranes for integrating superconducting microwave circuits with planar acoustic and optical devices and demonstrate back-action cooling of a 4.5 MHz mechanical resonance to its quantum ground state.

In Chapters 5 and 6, I describe our work on developing SOI-based electromechanical devices. I begin in Chapter 5 with a description of the fabrication process that we developed for the creation of high-Q microwave superconducting aluminum (Al) resonators on thin-film silicon membranes which is compatible with both superconducting qubits and silicon photonics. Utilizing this novel process, in Chapter 6, we demonstrate parametric radiation pressure coupling of a 10 GHz high-Q microwave resonator with strong vacuum coupling to the motion of a 6 MHz resonance frequency silicon micromechanical resonator. We again accomplish ground state cooling of the mechanical resonator and reach nearly strong coupling between the microwave resonance and the mechanical resonator. As a proof of concept we present the measurements of an integrated superconducting electromechanical circuit and a 'zipper'-cavity photonic crystal, where the mechanical resonator is coupled simultaneously to both the optical and the microwave resonance, where we present and discuss some of the challenges associated with operating such optomechanical and electromechanical devices together at a temperature of $T_f = 10$ mK.

Finally, in Chapter 7, I present the design, fabrication, and characterization of a SOI-based electromechanical device in which a pair of hybridized electrical microwave resonators are used to couple to a high frequency acoustic mode in the hypersonic frequency range (0.425 GHz). Utilizing a two-photon resonance condition for efficient microwave pumping, we measure the intrinsic decay rate, back-action induced decay rate and the occupancy of the thermal bath coupled to the mechanical resonator. We conclude in Chapter 8 by considering several designs and fabrication improvements of the hypersonic electromechanical crystals that would enable them to perform quantum conversion between the electrical and acoustic domain.

Chapter 2

Position squared coupling in tunable photonic crystal optomechanical cavity

The interaction between light and mechanics in a cavity-optomechanical system is termed dispersive when it couples the frequency of the cavity to the position or amplitude of mechanical motion. To lowest order this coupling is linear in mechanical displacement; however, the overall radiation pressure interaction is inherently nonlinear due to the dependence on optical intensity. To date, this nonlinear interaction has been too weak to observe at the quantum level in all but the ultra-light cold atomic gases [38], and typically a large optical drive is used to parametrically enhance the optomechanical interaction. Higher order dispersive optomechanical coupling may also be prominent. In particular, "x^2-coupling" where the cavity frequency is coupled to the square of the mechanical displacement has been proposed as a means for realizing quantum non-demolition (QND) measurements of phonon number [32,33,39], measurement of phonon shot noise [36], and the cooling and squeezing of mechanical motion [40–42]. In addition to dispersive coupling, an effective x^2-coupling via optical homodyne measurement has also been proposed, with the capability of generating and detecting non-Gaussian motional states [43].

Despite significant technical advances made in recent years [34,35,44,45], the use of x^2-coupling for measuring or preparing non-classical quantum states of a mesoscopic mechanical resonator remains an elusive goal. This is a direct result of the small coupling rate to motion at the quantum level, which for x^2-coupling scales as the square of the zero-point motion amplitude of the mechanical resonator, $x_{\text{zpf}}^2 = \hbar/2m_{\text{eff}}\omega_m$, where m_{eff} is the motional mass of the resonator and ω_m is the resonant frequency. As described in Ref. [33], one method to greatly enhance the x^2-coupling in a multi-mode cavity-optomechanical system is to fine-tune the mode splitting $2J$ to that of the

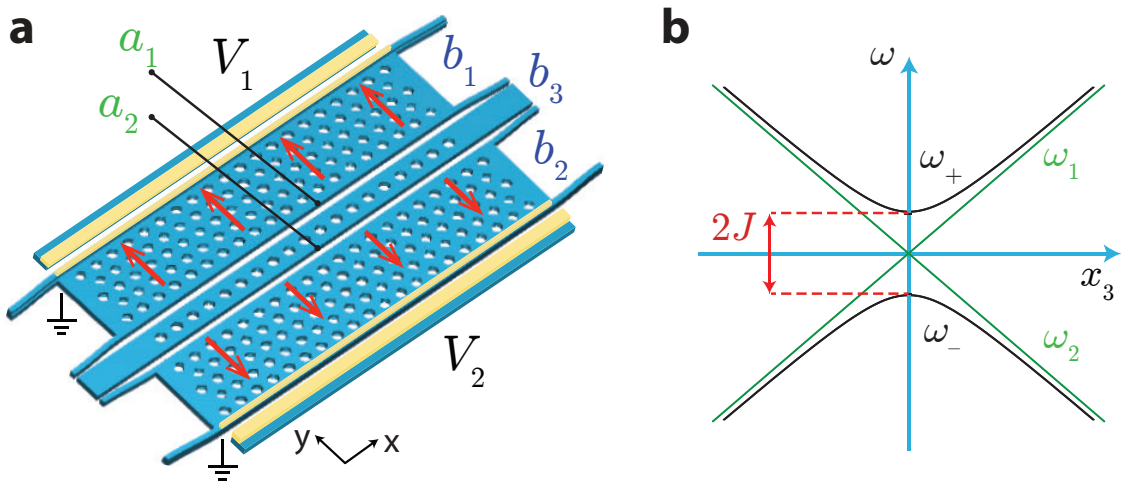

Figure 2.1: **a,** Double-slotted photonic crystal cavity with optical cavity resonances (a_1, a_2) centered around the two slots, and three fundamental in-plane mechanical resonances corresponding to motion of the outer slabs (b_1, b_2) and the central nanobeam (b_3). Tuning the equilibrium position of the outer slabs b_1 and b_2, and consequently the slot size on either side of the central nanobeam, is achieved by pulling on the slabs (red arrows) through an electrostatic force proportional to the square of the voltage applied to capacitors on the outer edge of each slab. **b,** Dispersion of the optical modes as a function of x_3, the in-plane displacement of the central nanobeam from its symmetric equilibrium position. Due to tunnel coupling at a rate J the slot modes a_1 and a_2 hybridize into the even and odd supermodes a_+ and a_-, which have a parabolic dispersion near the central anti-crossing point ($\omega_1 = \omega_2$).

mechanical resonance frequency. In this chapter, we utilize a quasi two-dimensional (2D) photonic crystal structure to create an optical cavity supporting a pair of high-Q optical resonances in the 1500 nm wavelength band exhibiting large linear optomechanical coupling. The double-slotted structure is split into two outer slabs and a central nanobeam, all three of which are free to move, and electrostatic actuators are integrated into the outer slabs to allow for both the trimming of the optical modes into resonance and tuning of the tunnel coupling rate J(Figure2.1a). Due to the form of the underlying photonic bandstructure the spectral ordering of the cavity supermodes in this structure may be reversed, enabling arbitrarily small values of J to be realized.

2.1 Theoretical Background

Before we discuss the specific double-slotted photonic crystal cavity-optomechanical system studied in this work, we consider a more generic multi-moded system consisting of two optical modes which are dispersively coupled to the same mechanical mode, and in which the dispersion of each mode is

linear with the amplitude coordinate x of the mechanical mode. If we further assume a purely optical coupling between the two optical modes, the Hamiltonian for such a three-mode optomechanical system in the absence of drive and dissipation is given by $\hat{H} = \hat{H}_0 + \hat{H}_{\text{OM}} + \hat{H}_J$:

$$\hat{H}_0 = \hbar\omega_1 \hat{a}_1^\dagger \hat{a}_1 + \hbar\omega_2 \hat{a}_2^\dagger \hat{a}_2 + \hbar\omega_m \hat{b}^\dagger \hat{b}, \tag{2.1}$$

$$\hat{H}_{\text{OM}} = \hbar(g_1 \hat{a}_1^\dagger \hat{a}_1 + g_2 \hat{a}_2^\dagger \hat{a}_2)\hat{x} \tag{2.2}$$

$$\hat{H}_J = \hbar J(\hat{a}_1^\dagger \hat{a}_2 + \hat{a}_2^\dagger \hat{a}_1). \tag{2.3}$$

Here, $\hat{a}_i$ and ω_i are the annihilation operator and the bare resonance frequency of the ith optical resonance, $\hat{x} = (\hat{b}^\dagger + \hat{b})x_{\text{zpf}}$ is the quantized amplitude of motion, x_{zpf} the zero point amplitude of the mechanical resonance, ω_m is the bare mechanical resonance frequency, and g_i is the linear optomechanical coupling constant of the ith optical mode to the mechanical resonance. Without loss of generality, we take the bare optical resonance frequencies to be equal ($\omega_1 = \omega_2 \equiv \omega_0$), allowing us to rewrite the Hamiltonian in the normal mode basis $\hat{a}_\pm = (\hat{a}_1 \pm \hat{a}_2)/\sqrt{2}$ as,

$$\begin{aligned}\hat{H} = \hbar\omega_+(0)\hat{a}_+^\dagger \hat{a}_+ + \hbar\omega_-(0)\hat{a}_-^\dagger \hat{a}_- + \hbar\omega_m \hat{b}^\dagger \hat{b} \\ + \hbar\left(\frac{g_1+g_2}{2}\right)\left(\hat{a}_+^\dagger \hat{a}_+ + \hat{a}_-^\dagger \hat{a}_-\right)\hat{x} + \hbar\left(\frac{g_1-g_2}{2}\right)\left(\hat{a}_+^\dagger \hat{a}_- + \hat{a}_-^\dagger \hat{a}_+\right)\hat{x},\end{aligned} \tag{2.4}$$

where $\omega_\pm(0) = \omega_0 \pm J$.

For $|J| \gg \omega_m$ such that $\hat{x}$ can be treated as a quasi-static variable [32, 33], the Hamiltonian can be diagonalized, resulting in eigenfrequencies $\omega_\pm(\hat{x})$,

$$\omega_\pm(\hat{x}) \approx \omega_0 + \frac{(g_1+g_2)}{2}\hat{x} \pm J\left(1 + \frac{(g_1-g_2)^2}{8J^2}\hat{x}^2\right). \tag{2.5}$$

As shown below, in the case of the fundamental in-plane motion of the outer slabs of the double-slotted photonic crystal cavity we have only one of g_1 or g_2 non-zero, whereas in the case of the fundamental in-plane motion of the central nanobeam we have $g_1 \approx -g_2$.

For a system in which the mechanical mode couples to the a_1 and a_2 optical modes with linear

dispersive coupling of equal magnitude but opposite sign ($g_1 = -g_2 = g$), the dispersion in the quasi-static normal mode basis is purely quadratic with effective x^2-coupling coefficient,

$$g' = g^2/2J, \tag{2.6}$$

and quasi-static Hamiltonian,

$$\hat{H} \approx \hbar \left(\omega_+(0) + g'\hat{x}^2\right) \hat{n}_+ + \hbar \left(\omega_-(0) - g'\hat{x}^2\right) \hat{n}_- + \hbar\omega_m \hat{n}_b, \tag{2.7}$$

where $\hat{n}_\pm$ are the number operators for the $a_\pm$ supermodes and $\hat{n}_b$ is the number operator for the mechanical mode. Rearranging this equation slightly highlights the interpretation of the x^2 optomechanical coupling as inducing a static optical spring,

$$\hat{H} \approx \hbar\omega_+(0)\hat{n}_+ + \hbar\omega_-(0)\hat{n}_- + \hbar \left[\omega_m \hat{n}_b + g' \left(\hat{n}_+ - \hat{n}_-\right) \hat{x}^2\right], \tag{2.8}$$

where the static optical spring constant $\bar{k}_s = 2\hbar g' \left(n_+ - n_-\right)$ depends upon the average intra-cavity photon number in the even and odd optical supermodes, $n_\pm \equiv \langle \hat{n}_\pm \rangle$.

For a sideband resolved system ($\omega_m \gg \kappa$), the quasi-static Hamiltonian can be further approximated using a rotating-wave approximation as

$$\hat{H} \approx \hbar[\omega_+(0) + 2\tilde{g}'(\hat{n}_b + 1/2)]\hat{n}_+ + \hbar[\omega_-(0) - 2\tilde{g}'(\hat{n}_b + 1/2)]\hat{n}_- + \hbar\omega_m \hat{n}_b, \tag{2.9}$$

where $\tilde{g}' \equiv g' x_{\text{zpf}}^2 = \tilde{g}^2/2J$ and $\tilde{g} \equiv g x_{\text{zpf}}$ are the x^2 and linear vacuum coupling rates, respectively. It is tempting to assume from Eq. (2.9) that by monitoring the optical transmission through the even or odd supermode resonances, that one can then perform a continuous quantum non-demolition (QND) measurement of the phonon number in the mechanical resonator [39, 46–48]. As noted in Refs. [32, 33], however, the quasi-static picture described by the dispersion of Eq. (2.5) fails to capture residual effects resulting from the non-resonant scattering between the a_+ and a_- supermodes which depends linearly on $\hat{x}$ (last term of Eq. (2.4)). Only in the vacuum strong coupling limit ($\tilde{g}/\kappa \gtrsim 1$) can one realize a QND measurement of phonon number [32, 33].

The regime of $|2J| \sim \omega_m$ is also very interesting, and explored in depth in Refs. [33, 49].

Transforming to a reference frame which removes in Eq. (2.4) the radiation pressure interaction between the even and odd supermodes to first order in g yields an effective Hamiltonian given by [33, 50],

$$\begin{aligned}\hat{H}_{\text{eff}} \approx \hbar\omega_+(0)\hat{n}_+ + \hbar\omega_-(0)\hat{n}_- + \hbar\omega_m\hat{n}_b \\ + \hbar\frac{\tilde{g}^2}{2}\left[\frac{1}{2J-\omega_m}+\frac{1}{2J+\omega_m}\right]\left(\hat{a}_+^\dagger\hat{a}_+ - \hat{a}_-^\dagger\hat{a}_-\right)\left(\hat{b}+\hat{b}^\dagger\right)^2 \\ + \hbar\frac{\tilde{g}^2}{2}\left[\frac{1}{2J-\omega_m}-\frac{1}{2J+\omega_m}\right]\left(\hat{a}_+^\dagger\hat{a}_- + \hat{a}_-^\dagger\hat{a}_+\right)^2, \quad (2.10)\end{aligned}$$

where we assume $|\tilde{g}/\delta| \ll 1$ for $\delta \equiv |2J| - \omega_m$, and terms of order $\tilde{g}^3/(2J \pm \omega_m)^2$ and higher have been neglected. In the limit $|J| \gg \omega_m$ we recover the quasi-static result of Eq. (2.7), whereas in the near-resonant limit of $|\delta| \ll |J|, \omega_m$ we arrive at

$$\begin{aligned}\hat{H}_{\text{eff}} \approx \hbar\omega_+(0)\hat{n}_+ + \hbar\omega_-(0)\hat{n}_- + \hbar\omega_m\hat{n}_b + \hbar\frac{\tilde{g}^2}{2\delta}\big[2sgn(J)\left(\hat{n}_+ - \hat{n}_-\right)\left(\hat{n}_b+1\right) \\ + 2\hat{n}_+\hat{n}_- + \hat{n}_+ + \hat{n}_-\big]. \quad (2.11)\end{aligned}$$

Here we have neglected highly oscillatory terms such as $(\hat{a}_+^\dagger\hat{a}_-)^2$ and $\hat{b}^2$, a good approximation in the sideband resolved regime ($\kappa \ll \omega_m, |J|$). From Eq. (2.11) we find that the frequency shift per phonon of the optical resonances is much larger than in the quasi-static case ($\tilde{g}^2/2|\delta| \gg \tilde{g}^2/2|J|$). Although a QND measurement of phonon number still requires the vacuum strong coupling limit, this enhanced read-out sensitivity is attainable even for $\tilde{g}/\kappa \ll 1$. Equation (2.11) also indicates that, much like the QND measurement of phonon number, in the near-resonant limit a measurement of the intra-cavity photon number stored in one optical supermode can be performed by monitoring the transmission of light through the other supermode [33, 50].

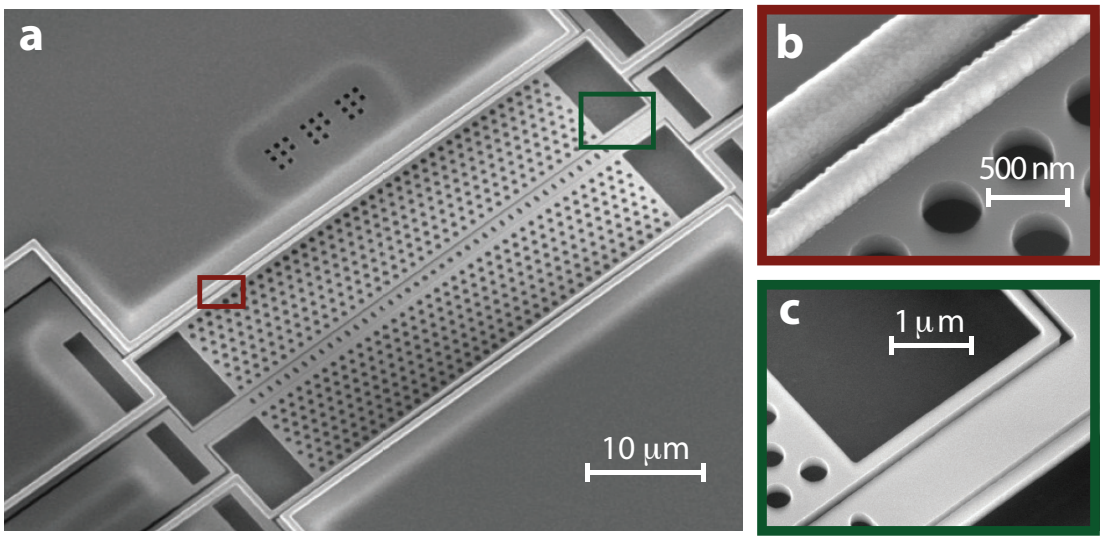

Figure 2.2: **a,** SEM image of a fabricated double-slotted photonic crystal device in the SOI material system. **b,** Zoom-in SEM image showing the capacitor gap ($\sim$ 100 nm) for the capacitor of one of the outer slabs. **c,** Zoom-in SEM image showing some of the suspending tethers of the outer slabs which are of length 2.5 μm and width 155 nm. The central beam, which is much wider, is also shown in this image.

2.2 Double-Slotted Photonic Crystal Optomechanical Cavity

A sketch of the double-slotted photonic crystal cavity structure is shown in Fig. 2.1a. As detailed below and elsewhere [51], the optical cavity structure can be thought of as formed from two coupled photonic crystal waveguides, one around each of the nanoscale slots, and each with propagation direction along the z-axis. A small adjustment ($\sim$ 5%) in the lattice constant is used to produce a local shift in the waveguide band-edge frequency, resulting in trapping of optical resonance to this "defect" region. Optical tunneling couples across the cental photonic crystal beam, which in this case contains only a single row of holes, couples the cavity mode of slot 1 (a_1) to the cavity mode of slot 2 (a_2).

The two outer photonic crystal slabs and the central nanobeam are all mechanically compliant, behaving as independent mechanical resonators. The mechanical resonances of interest in this work are the fundamental in-plane flexural modes of the top slab, the bottom slab, and the central nanobeam, denoted by b_1, b_2, and b_3, respectively. For a perfectly symmetric structure about the z-axis of the central nanobeam, the linear dispersive coupling coefficients of the b_3 mode of the central

nanobeam to the two slot modes a_1 and a_2 are equal in magnitude but opposite in sign, resulting in a vanishing linear coupling at the resonant point where $\omega_1 = \omega_2$ (c.f., Eq. (2.5)). Figure 2.1b shows a plot the dispersion of the optical resonances as a function of the nanobeam's in-plane displacement (x_3), illustrating how the linear dispersion of the slot modes (a_1, a_2) transforms into quadratic dispersion for the upper and lower supermode branches (a_u, a_l) in the presence of tunnel coupling J. The mechanical modes of the outer slabs (b_1, b_2) provide degrees of freedom for post-fabrication tuning of the slotted waveguide optical modes, i.e., to symmetrize the structure such that $\omega_1 = \omega_2$. This is achieved in practice by integrating metallic electrodes which form capacitors at the outer edge of the two slabs of the structure as schematically shown in Fig. 2.1a.

The double-slotted photonic crystal cavity of this work is realized in the silicon-on-insulator (SOI) material system, with a top silicon device layer thickness of 220 nm and an underlying buried oxide (BOX) layer of 3 μm. Fabrication begins with the patterning of the metal electrodes of the capacitors, and involves electron beam (ebeam) lithography followed by evaporation and lift-off of a bi-layer consisting of a 5 nm sticking layer of chromium and a 150 nm layer of gold. After lift-off we deposit uniformly a ~ 4 nm protective layer of silicon dioxide. A second electron beam lithography step is performed, aligned to the first, to form the pattern of the photonic crystal and the nanoscale (~ 90 nm width) slots which separate the central nanobeam from the outer slabs. At this step, we also pattern the support tethers of the outer slabs and the cut lines which define and isolate the outer capacitors. A fluorine based (C_4F_8 and SF_6) inductively coupled reactive-ion etch (ICP-RIE) is used to transfer the ebeam lithography pattern through the silicon device layer. The remaining ebeam resist is stripped using trichloroethylene, and then the sample is cleaned in a heated Piranha (H_2SO_4:H_2O_2) solution. The devices are then released using a hydrofluoric (HF)acid etch to remove the sacrificial BOX layer (this also removes the deposited protective silicon dioxide layer), followed by a water rinse and critical point drying.

A scanning electron microscope (SEM) image showing the overall fabricated device structure is shown in Fig. 2.2a. Zoom-ins of the capacitor region of one of the outer slabs and the tether region at the end of the nanobeam are shown in Figs. 2.2b and c, respectively. Note that the geometry of the capacitors and the stiffness of the support tethers determine how tunable the structure is under application of voltages to the capacitor electrodes. The outermost electrode of each slab is connected

to an independent low-noise DC voltage source, while the innermost electrodes are connected to a common ground, thereby allowing one to independently pull on each outer slab with voltages V_1 and V_2. In this configuration, we are limited to increasing the slots defining the optical modes around the central nanobeam.

2.2.1 Photonic bandstructure

To further understand the optical properties of the double-slotted photonic crystal cavity, we display in Fig. 2.3a the photonic bandstructure of the periodic waveguide structure. The parameters of the waveguide are given in the caption of Fig. 2.3a. Here we only show photonic bands that are composed of waveguide modes with even vector symmetry around the "vertical" mirror plane (σ_z), where the vertical mirror plane is defined by the z-axis normal and lies in the middle of the thin-film silicon slab. The fundamental (lowest lying) optical waveguide bands are of predominantly transverse (in-plane) electric field polarization, and are thus called TE-like. In the case of a perfectly symmetric structure, we can further classify the waveguide bands by their odd or even symmetry about the "horizontal" mirror plane (σ_y) defined by the y-axis normal and cutting through the middle of the central nanobeam. The two waveguide bands of interest that lie within the quasi-2D photonic bandgap of the outer photonic crystal slabs, shown as bold red and black curves, are labeled "even" and "odd" depending on the spatial symmetry with respect to σ_y of their mode shape for the dominant electric field polarization in the y-direction, E_y (note that this labeling is to their actual vector symmetry). The E_y spatial mode profiles at the X-point for the odd and even waveguide supermodes are shown in Figs. 2.3b and c, respectively.

An optical cavity is defined by decreasing the lattice constant 4.5% below the nominal value of $a_0 = 480$ nm for the middle five periods of the waveguide (see Fig. 2.3d). This has the effect of locally pushing the bands toward higher frequencies [55, 56], which creates an effective potential that localizes the optical waveguide modes along the x-axis of the waveguide. The resulting odd and even TE-like cavity supermodes are shown in Figs. 2.3d and e, respectively. These optical modes correspond to the normal modes a_+ and a_- in Section 2.1, which are symmetric and anti-symmetric superpositions, respectively, of the cavity modes localized around each slot (a_1 and a_2). Due to the non-monotonic decrease in the even waveguide supermode as one moves away from

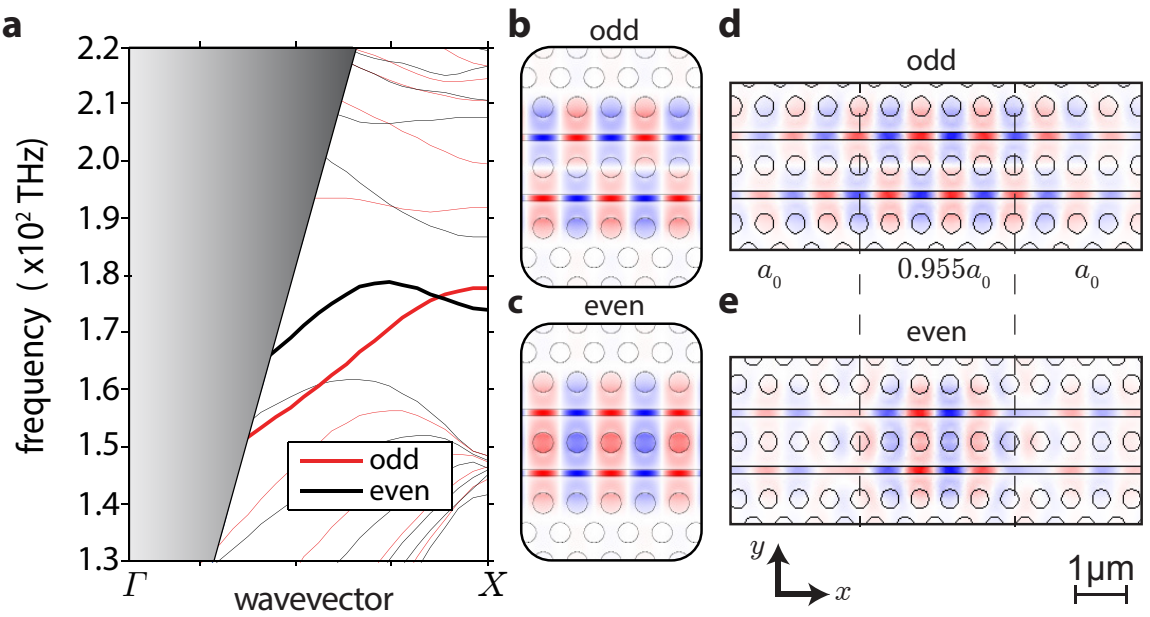

Figure 2.3: **a,** Bandstructure diagram of the periodic (along x) double-slotted photonic crystal waveguide structure. Here we only show photonic bands that are composed of modes with even vector symmetry around the "vertical" (σ_z) mirror plane. The two waveguide bands of interest lie within the quasi-2D photonic bandgap of the outer photonic crystal slabs and are shown as bold red and black curves. These waveguide bands are labeled "even" (bold black curve) and "odd" (bold red curve) due to the spatial symmetry of their mode shape for the dominant electric field polarization in the y-direction, E_y. The simulated structure is defined by the lattice constant between nearest neighbor holes in the hexagonal lattice ($a_0 = 480$ nm), the thickness of the silicon slab ($d = 220$ nm), the width of the two slots ($s = 100$ nm), and the refractive index of the silicon layer ($n_{\mathrm{Si}} = 3.42$). The hole radius in the outer slabs and the central nanobeam is $r = 144$ nm. The grey shaded region represents a continuum of radiation modes which lie above the light cone for the air cladding which surrounds the undercut silicon slab structure. The small blue circle indicates the crossing point of the even and odd supermode waveguide bands. **b,** Normalized E_y field profile at the X-point of the odd waveguide supermode, shown for several unit cells along the x guiding axis. **c,** E_y field profile of the even waveguide supermode. Waveguide simulations of **a-c** were performed using the plane-wave mode solver MPB [52, 53]. Normalized E_y field profile of the corresponding localized cavity supermodes of **d** odd and **e** even spatial symmetry about the horizontal mirror plane. The lattice constant a_0 is decreased by 4.5% for the central five lattice constants between the dashed lines to localize the waveguide modes. Simulations of the full cavity modes were performed using the COMSOL finite-element method mode solver package [54].

the X-bandedge (c.f., Fig. 2.3a), we find that the simulated optical Q-factor of the even a_+ cavity supermode is significantly lower than that of the odd a_- cavity supermode. This will be a key distinguishing feature found in the measured devices as well.

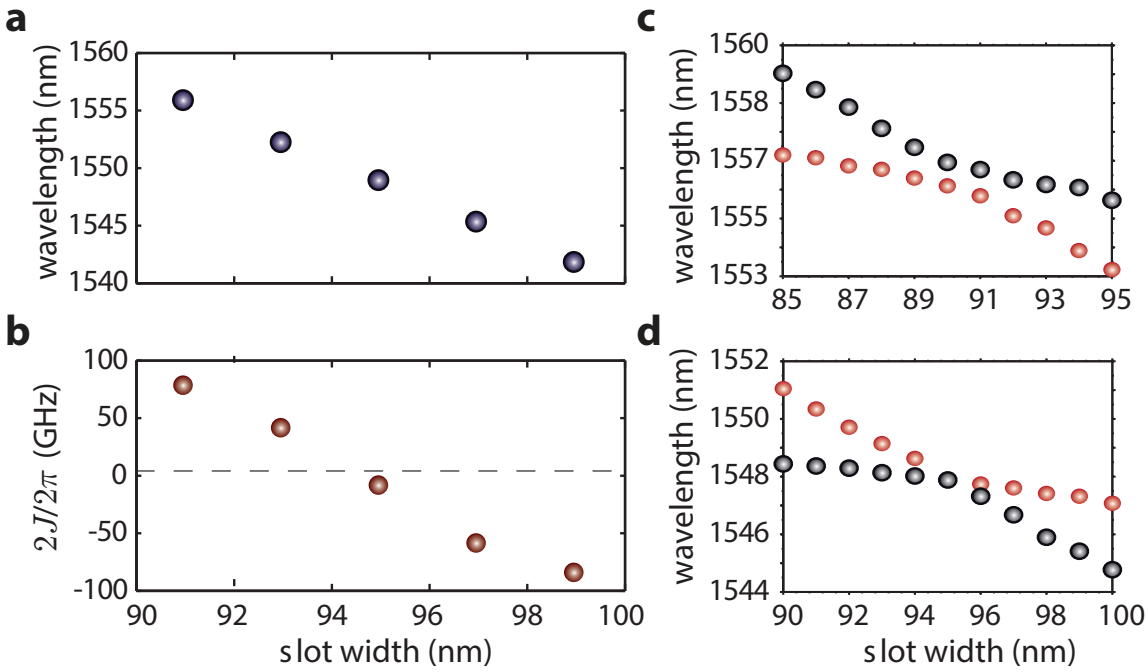

Figure 2.4: Symmetric tuning of the slot widths of the double-slotted photonic crystal cavity showing **a** the mean wavelength shift and **b** the splitting $2J = \omega_+ - \omega_-$ of the even and odd cavity supermodes versus slot width $s = s_1 = s_2$. **c-d** Avoided crossing of the cavity supermodes obtained by tuning s_1 while keeping s_2 fixed at **c** $s_2 = 90$ nm and **d** $s_2 = 95$ nm. For all simulations in **a-d** the parameters of the cavity structure are the same as in Fig. 2.3 save for the slot widths. The simulations were performed using the COMSOL FEM mode solver [54].

2.2.2 Optical tuning simulations

The slot width in the simulated waveguide and cavity structures of Fig. 2.3 is set at $s = 100$ nm. For this slot width we find a lower frequency for the even (a_+) supermode than the odd (a_-) supermode at the X-point photonic bandedge of the periodic waveguide and in the case of the localized cavity modes. Figure 2.4 presents finite-element method (FEM) simulations of the optical cavity for slot sizes swept from 90 nm to 100 nm in steps of 1 nm, all other parameters the same as in Fig. 2.3. For the slot widths tuned symmetrically ($s_1 = s_2 = s$), the mean wavelength of the even and odd cavity supermodes and their frequency splitting $2J = \omega_+ - \omega_-$ are plotted in Fig. 2.4a and Fig. 2.4b, respectively. As expected the mean wavelength drops for increasing slot width. The frequency splitting, however, also monotonically decreases with slot width, going from a positive value for $s = 90$ nm to a negative for $s = 100$ nm slots and crossing zero for a slot width of $s = 95$ nm. In Figs. 2.4c and d the symmetry is broken by keeping s_2 fixed and scanning s_1; the cavity supermodes

are driven through an anti-crossing with a splitting determined by the fixed slot width s_2.

The spectral inversion of the even a_+ and odd a_- cavity supermodes predicted in Fig. 2.4b originates in the unequal overlap of each mode with the air slots separating the two outer slabs from the central nanobeam. The odd supermode tends to be pushed further from the middle of the central nanobeam, having slightly larger overlap with the air slots. An increase in the air region for increased slot size leads to a blue shift of both cavity supermodes. The odd mode having a larger electric field energy density in the air slots than the even mode is more affected by a change in the slot widths. Therefore, upon equal increase of the slot widths, the odd mode experiences larger frequency shifts than the even mode, which results in a tuning of the frequency splitting. For particular geometrical parameters of the central nanobeam [51], a change in the slot widths is sufficient to invert the spectral ordering of the supermodes. This means that arbitrarily small splittings can potentially be realized.

2.3 Mechanical Resonances

Having considered the optical cavity modes of the double-slotted planar photonic crystal, we now analyze the mechanical modes of the structure. In order to support mechanical resonances the photonic crystal slabs are suspended. The optical modes can interact with both flexural and localized acoustic modes of the central nanobeam. In Sec. 2.3.1, we present the flexural modes of the structure. We show that higher orders flexural modes are found to exist up to 1 GHz with significant optomechanical coupling, making them suitable for operation in the resolved sideband regime, where the optical linewidth κ is much smaller than the mechanical frequency ω_m [57]. In Sec. 2.3.2, we show that the defect developed to form the optical cavity also gives rise to a localized acoustic resonance of a few GHz frequency.

2.3.1 Flexural mechanical resonances

The outer slabs and nanobeam behave as three independent mechanical resonators supporting various in-plane and out-of-plane flexural mechanical resonances. Here, we focus on the in-plane flexural modes that are asymmetric with respect to the $y = 0$ plane mirror operator ($\sigma_y = -1$), and symmetric with respect to the $x = 0$ plane mirror operator ($\sigma_x = +1$), about the center of the structure. These flexural modes are represented in Fig. 2.5 with exaggerated deformation profiles. Since our main

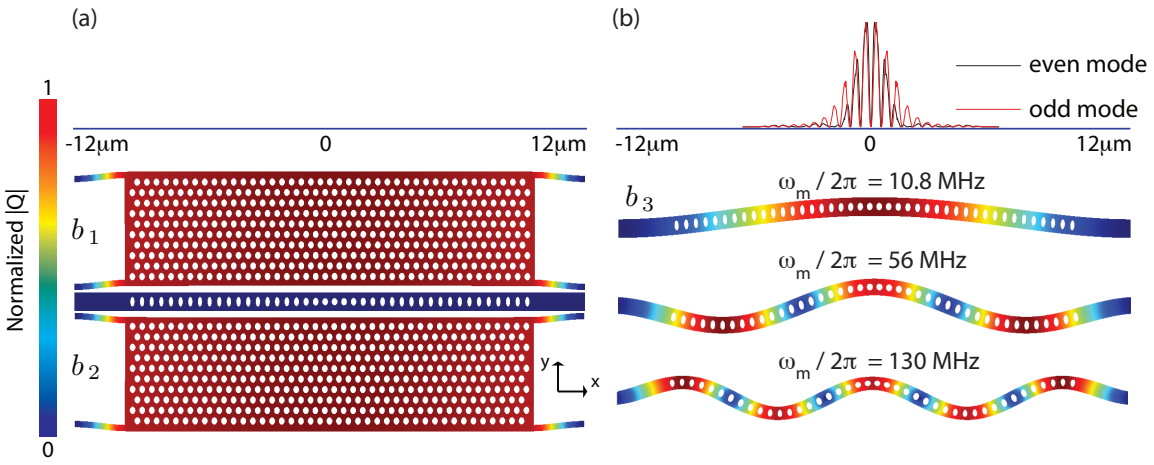

Figure 2.5: Normalized displacement profile of **a** the in-plane slab modes and **b** the nanobeam first and higher order in-plane flexural modes. The inset on top of **b** shows the profiles of $|E_y|^2$ along the waveguides for both the odd and even symmetry optical supermodes. The deformations are exaggerated for clarity. The photonic crystal parameters are the same as in Fig. 2.3. The central nanobeam is 731 nm wide and 24 μm long. The outer slabs are suspended by tethers of length $l_t = 2.5$ μm and width $w_t = 150$ nm.

focus will be on the fundamental resonances, we denote the fundamental in-plane flexural modes of the two outer slabs and nanobeam as b_1, b_2 and b_3 respectively. Their respective frequencies are denoted ω_{b_1}, ω_{b_2} and ω_{b_3}.

In our design, the outer slabs are suspended by tethers of length l_t =2.5 μm and width w_t =150 nm, yielding fundamental in-plane flexural resonance of $\omega_m/2\pi \simeq 6$ MHz. As shown in Fig. 2.5 (a), these modes correspond to a uniform displacement of the whole slabs. The displacement of one outer slab causes a uniform change of the width of the adjacent slot, and hence a change of the optical supermode frequencies. The in-plane slab modes provide degrees of freedom for the electromechanical tuning of the slot widths.

In Fig. 2.5 (b), we plot the displacement profiles of the first three lowest frequency (10.8 MHz, 56 MHz and 130 MHz) nanobeam in-plane flexural modes of symmetry $\{\sigma_x = +1, \sigma_y = -1\}$. The y-polarized electric field profiles $|E_y|^2$ are plotted in the inset for both the odd and even optical supermodes $a_\pm$. The finite extent of the optical modes along the x-axis of the photonic crystal structure limits the region of the nanobeam that will contribute to the optomechanical interaction. As a result, the nanobeam displacement amplitude x_3 can be approximated by a net effective displacement of the whole nanobeam $\bar{x}_3 \approx x_3$, causing one slot width to change by an amount $+\bar{x}_3$ and the other to

change by $-\bar{x}_3$. Because of this asymmetric displacement, the optomechanical couplings of these flexural mode to the individual slot modes a_1 and a_2 are expected to be equal and of opposite sign. This favors the quadratic and linear cross-mode interaction terms introduced in Eq. (2.9).

Higher order flexural modes of the nanobeam have been identified with frequencies up to 1 GHz and are summarized in Tab. 2.1. Assuming a moderate optical quality factor of $Q = 5 \times 10^5$, the resolved-sideband regime condition ($\kappa < \omega_m$) could be met with a flexural mode of frequency $\omega_m/2\pi = 400$ MHz.

2.3.2 Localized phononic crystal resonance

In Sec. 2.2.1 we described how to localize optical waveguide modes of the double-slotted photonic crystal waveguide propagating by engineering a perturbation to the waveguide unit cell in the propagation direction. In particular, we analyzed the photonic bandstructure of the waveguide unit cell and designed a defect based on a combination of change in the lattice constant and change in the central nanobeam hole aspect ratio. Here we study the phononic bandstructure of the nanobeam unit cell and show that our choice of photonic crystal defect parameters makes the nanobeam compatible with the localization of an GHz-frequency acoustic resonance.

Figure 2.6(a) and 2.6(b) show the FEM-simulated acoustic bandstructure of the nanobeam unit cell and the frequency shift of the *breathing* mode band at the Γ-point as the nanobeam transitions from the mirror unit cell geometry to the defect unit cell geometry. The breathing mode band is shown as a solid red curve. The nanobeam unit cell and the corresponding normalized displacement field profile $\mathbf{Q}(\mathbf{r})$ of the breathing mode are depicted in Figs. ‘2.6(e-g). The localized breathing mode is drawn from the Γ-point of the bandstructure in order to have a significant optomechanical coupling to the optical mode [58].

Figure 2.6(c) and 2.6(d) detail separately the shifts of Γ-point frequency of the breathing mode

Table 2.1: In-plane flexural modes of the nanobeam. We consider the modes with symmetric displacement with respect to σ_x. The geometric parameters of the nanobeam are the same as in Fig. 2.3.

$\omega_m/2\pi$ [MHz]	10.8	56	130	227	340	467	605	746	884	1025
x_{zpf} [fm]	15.8	6.6	4.2	3.1	2.5	2.2	1.9	1.7	1.6	1.5
m_{eff} [pg]	3.1	3.4	3.6	3.9	3.9	3.8	3.8	3.8	3.8	3.6

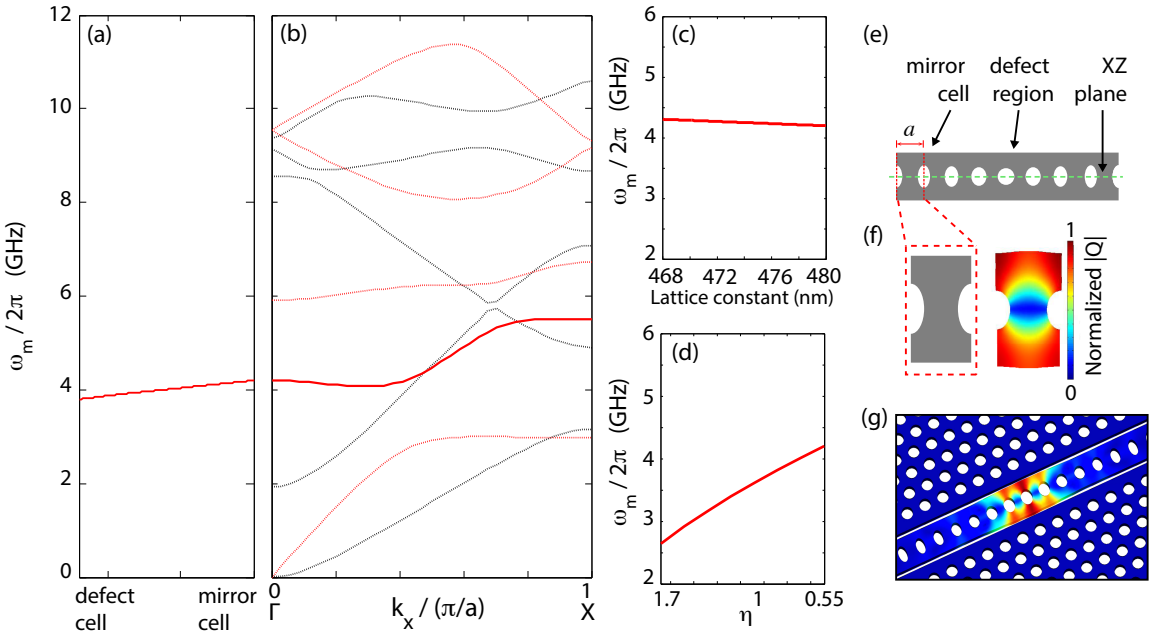

Figure 2.6: **a,b** Simulated phononic bandstructure of the nanobeam and defect mode drawn from the Γ-point. The breathing mode band is specified by the solid red line. The even (red lines) and odd (black lines) symmetry acoustic modes are defined with respect to σ_y mirror operator. **a,** Shift of the Γ-point frequency of the breathing mode band for a defect formed by both variations in lattice constant and ellipticity of holes. The defect parameters are the same as in Fig. 2.3. **c,** and **d,** show the shift of the breathing mode frequency at the Γ point due to variations of the lattice constant and of the holes aspect ratio, respectively. **e)** Mechanical beam and **f** normalized displacement field $\mathbf{Q}(\mathbf{r})$ of the localized breathing mode. The color scale indicates the magnitude of $\mathbf{Q}(\mathbf{r})$. **g,** Exaggerated deformation of the structure due to the breathing mode. All acoustic mode simulations were performed using COMSOL [54].

caused by the perturbation in the lattice constant and hole ellipticity of the nanobeam. Increasing the aspect ratio η will push the breathing mode frequency down into the band gap of the unperturbed mirror cells, while decreasing the lattice constant slightly increases the frequency of the Γ-point mode. As summarized in Fig. 2.6(a), the same defect used to localize the photonic crystal resonances satisfies the conditions to localize a phononic crystal resonance. Note that, in contrast to the mechanical flexural modes, the displacement of the localized breathing mode is symmetric with respect to σ_y so the optomechanical coupling to this mode is expected to be the same for both a_1 and a_2. Therefore, the breathing mode is expected to have negligible linear cross-mode and quadratic coupling strengths. Nevertheless, the breathing mode presents the advantage of being well in the resolved sideband regime and could potentially be used as an auxiliary mechanical mode in multimode

optomechanically induced transparency schemes, as proposed in Refs. [59, 60].

2.4 Optomechanical Coupling Relations

With knowledge of the optical and mechanical properties of the double slotted waveguide cavity, we can now turn to the calculation of the different optomechanical coupling factors. We utilize a perturbation theory of Maxwell's equations [61] suitable for dealing with both spatial shifts in the dielectric boundaries of the cavity structure as well as stress-induced modifications of the local dielectric constant of the deformed structure. Applying first-order perturbation theory to the numerically computed unperturbed optical field profiles and mechanical field profiles allows us to evaluate both the linear self-mode coupling $g_{\pm}$ and the linear cross-mode coupling g_{+-} for the nanobeam flexural modes [62]. Considering the perturbation theory to second-order yields the strength of the quadratic coupling in our structure. Finally, we consider the modification of the coupling strengths due to deviations of the structure from the symmetric equilibrium position of the central nanobeam and outer slabs.

2.4.1 Linear self-mode optomechanical coupling

Maxwell's equations in a source-free, linear dielectric medium yields the following eigenvalue equation for the electric field:

$$\nabla \times \nabla \times |E\rangle = \left(\frac{\omega^2}{c}\right) \epsilon \, |E\rangle \,, \tag{2.12}$$

where we have used the Dirac notation $|E\rangle$ for the electric field $E(r)$ eigenstate with harmonic time dependence $e^{-i\omega t}$. Here, c is the speed of light in vacuum, and $\epsilon(r)$ is a dielectric constant which is a function of the spatial coordinate r (and most generally a tensor). We are interested in the change in the modal frequency due to an infinitesimal perturbation $\delta\alpha$ to the dielectric structure. The first-order correction term to the mode frequency is expressed as

$$\delta\omega^{(1)} = -\frac{\omega^{(0)}}{2} \frac{\langle E^{(0)}| \, \delta\alpha \, |E^{(0)}\rangle}{\langle E^{(0)}| \, \epsilon^{(0)} \, |E^{(0)}\rangle}, \tag{2.13}$$

where $\epsilon^{(0)}(r)$ is the unperturbed dielectric constant of the structure, $|E^{(0)}\rangle$ and $\omega^{(0)}$ are electric field

and frequency of the harmonic optical mode of interest, $\langle E^{(0)}|\,\epsilon^{(0)}\,|E^{(0)}\rangle \equiv \int_V \mathrm{d}^3 r \left(E^{(0)} \cdot \left(\epsilon^{(0)} E^{(0)}\right)^*\right)$, and $\delta\alpha$ depends upon the type of perturbation to the dielectric structure.

The change in dielectric constant due to mechanical displacement arises from two main contributions. The first contribution is due to shifting of the interface boundary between two dielectric media. In this case the dielectric function is a high-contrast step function which translates displacements normal to the boundary into local modifications of the dielectric seen by the electric field. As proposed by Johnson, et al., in [61], the appropriate perturbation theory in this so-called *moving boundary* (MB) problem is given by

$$\delta\omega^{(1)}_{\mathrm{MB}} = -\frac{\omega^{(0)}}{2}\frac{\int_A \mathrm{d}^2 r(\mathbf{q}\cdot\mathbf{n})\,[\Delta\epsilon|E^{(0)}_{\parallel}|^2 - \Delta\epsilon^{-1}|D^{(0)}_{\perp}|^2]}{\langle E^{(0)}|\,\epsilon^{(0)}\,|E^{(0)}\rangle}, \tag{2.14}$$

where $\epsilon_{1(2)}$ is the dielectric constant of medium 1 (2) at any point in the boundary surface A between two media of differing dielectric constant, $\Delta\epsilon = \epsilon_1 - \epsilon_2$, $\Delta\epsilon^{-1} = \epsilon_1^{-1} - \epsilon_2^{-1}$, $|E^{(0)}_{\parallel}|$ ($|D^{(0)}_{\perp}|$) is the magnitude of the unperturbed electric (displacement) field polarized in the plane (out of the plane) of the boundary surface A between medium 1 and medium 2, and $\mathbf{n}(r)$ is the outward unit vector normal pointing from medium 1 into medium 2 on boundary A. Here, $\mathbf{q}(\mathbf{r})$ is the normalized displacement field of the mechanical mode of interest with maximum displacement equal to unity, $\max|\mathbf{q}(\mathbf{r})| = 1$. We can also define an effective mass of the mechanical mode in terms of q,

$$m_{\mathrm{eff}} = \int_V \mathrm{d}^3 r \rho(r)|\mathbf{q}(\mathbf{r})|^2, \tag{2.15}$$

where ρ is the mass density of the dielectric material defining the optomechanical structure. This effective mass is the appropriate motional mass for evaluating the zero-point fluctuation amplitude, $x_{\mathrm{zpf}} = \sqrt{\hbar/2m_{\mathrm{eff}}\omega_m}$, of the generalized amplitude coordinate corresponding to the point of maximum amplitude of the mechanical mode.

The second contribution to the linear self-mode coupling is due to the *photoelastic effect*, resulting from the change of the dielectric constant due to the local strain induced by the mechanical displacement. The first-order perturbation to the dielectric tensor is given by

$$\delta\boldsymbol{\epsilon} = -\boldsymbol{\epsilon}^{(0)}\frac{\mathbf{pS}}{\epsilon_0}\boldsymbol{\epsilon}^{(0)}, \tag{2.16}$$

where $\boldsymbol{\epsilon}^{(0)}$ is the unperturbed dielectric tensor, ϵ_0 is the permittivity of free space, $\mathbf{p}$ is the fourth rank photoelastic tensor, and $\mathbf{S}$ is the symmetric strain tensor. For an isotropic medium this simplifies to

$$\delta\epsilon_{ij} = -\epsilon_0 n^4 p_{ijkl} S_{kl}, \tag{2.17}$$

in index notation. In matrix form,

$$\delta\boldsymbol{\epsilon} = -\epsilon_0 n^4 \times \begin{bmatrix} p_{11}S_{xx} + p_{12}(S_{yy}+S_{zz}) & p_{44}S_{xy} & p_{44}S_{xz} \\ p_{44}S_{xy} & p_{11}S_{yy} + p_{12}(S_{xx}+S_{zz}) & p_{44}S_{yz} \\ p_{44}S_{xz} & p_{44}S_{yz} & p_{11}S_{zz} + p_{12}(S_{xx}+S_{yy}) \end{bmatrix}. \tag{2.18}$$

The resulting first-order photoelastic (PE) correction to the optical frequency is

$$\begin{aligned} \delta\omega^{(1)}_{\mathrm{PE}} = \frac{\omega^{(0)}\epsilon_0 n^4}{2\left\langle E^{(0)}\right| \boldsymbol{\epsilon}^{(0)} \left|E^{(0)}\right\rangle} \int_V \mathrm{d}^3 r 2 \Big[& \mathbf{Re}((E_x^{(0)})^* E_y^{(0)}) p_{44} S_{xy} \\ & + \mathbf{Re}((E_x^{(0)})^* E_z^{(0)}) p_{44} S_{xz} + \mathbf{Re}((E_y^{(0)})^* E_z^{(0)}) p_{44} S_{yz} \\ & + |E_x^{(0)}|^2 (p_{11}S_{xx} + p_{12}(S_{yy}+S_{zz})) + |E_y^{(0)}|^2 (p_{11}S_{yy} + p_{12}(S_{xx}+S_{zz})) \\ & + |E_z^{(0)}|^2 (p_{11}S_{zz} + p_{12}(S_{yy}+S_{xx})) \Big]. \end{aligned} \tag{2.19}$$

In the structures studied here, which are made by etching patterns into a thin-film of silicon, the only two media are silicon and vacuum. As such, for the PE contribution to the linear self-mode coupling we utilize the photoelastic tensor coefficients for silicon in evaluating the integral in the numerato: $p_{11} = -0.0101$, $p_{12} = 0.009$ and $p_{44} = -0.051$.

We begin by considering the calculation of g_{+,b_1} and g_{-,b_1} for our double-slotted photonic crystal device, i.e., the linear optomechanical couplings of the optical supermodes a_+ and a_- to the fundamental in-plane flexural mode of either outer slab (we choose b_1 in this case). Table 2.2 displays the numerically computed coefficients using the perturbation theory described above in terms

of the unperturbed optical and mechanical fields. g_{+,b_1} and g_{-,b_1} can also be approximated by fitting the anti-crossing curves of Fig. 2.4 using the dispersion relation given in Eq. (2.5). The approximate dispersion relation fit values for the linear couplings are also shown in Tab. 2.2, and compare well to the exact perturbation theory values.

The localized breathing mode of the central nanobeam was found by FEM simulations to be at a mechanical frequency of $\omega_m/2\pi \approx 4$ GHz, with linear coupling rates of $\tilde{g}_+/2\pi$ =249 kHz and $\tilde{g}_-/2\pi$ =163 kHz to the $a_\pm$ supermodes, respectively, where we have used the notation $\tilde{g}_\pm = g_\pm x_{\text{zpf}}$.

Table 2.2: Strength of the linear optomechanical coupling of the optical supermodes to the fundamental in-plane flexural modes of the *outer slabs* for three different slot widths. The second and third columns display the linear coupling strengths calculated numerically using the perturbation theory. The fourth column gives the values of the optomechanical coupling constant obtained by fitting the anti-crossing curves shown in Fig. 2.4. The geometric parameters of the nanobeam are the same as in Fig. 2.5.

	First order perturbation theory		Anti-crossing fit
Slot width [nm]	$g_{+,b_1}/2\pi$ [GHz/nm]	$g_{-,b_1}/2\pi$ [GHz/nm]	$[(g_{1,b_1}+g_{2,b_1})/2]/2\pi$ [GHz/nm]
90	55.05	57.79	51.13
95	51.81	53.62	48.81
100	41.12	47.69	44.45

2.4.2 Linear cross-mode optomechanical coupling

By analogy with Eq. (2.13), the first order perturbation term for the linear cross-mode coupling g_{ij}, where $i \neq j$, can be written as [63]

$$g_{ij,k} = -\frac{\sqrt{\omega_i^{(0)}\omega_j^{(0)}}}{2} \frac{\langle E_i^{(0)}|\, \delta\alpha_k \,|E_j^{(0)}\rangle}{\left(\langle E_i^{(0)}|\, \epsilon^{(0)} \,|E_i^{(0)}\rangle\right)^{1/2} \left(\langle E_j^{(0)}|\, \epsilon^{(0)} \,|E_j^{(0)}\rangle\right)^{1/2}}. \tag{2.20}$$

In the case of the double-slotted photonic crystal of this work, we have for the shifting boundaries contribution to the cross-mode coupling between the supermodes a_+ and a_- at the symmetric ($\{x_{k,eq}\} = 0$) equilibrium position (center of the anti-crossing curve of Fig. 2.4):

$$g_{+-,k} = -\frac{\sqrt{\omega_+^{(0)}\omega_-^{(0)}}}{2} \frac{\int_A \mathrm{d}^2 r (q_k \cdot n)\, [\Delta\epsilon \left(E_{\parallel,+}^{(0)}\right)^* \cdot E_{\parallel,-}^{(0)} - \Delta\epsilon^{-1} \left(D_{\perp,+}^{(0)}\right)^* \cdot D_{\perp,-}^{(0)}]}{\left(\langle E_+^{(0)}|\, \epsilon^{(0)} \,|E_+^{(0)}\rangle\right)^{1/2} \left(\langle E_-^{(0)}|\, \epsilon^{(0)} \,|E_-^{(0)}\rangle\right)^{1/2}}. \tag{2.21}$$

Note that for the flexural mechanical modes of the photonic crystal structure (either slab or central nanobeam modes) we expect this to be the dominant contribution to the optomechanical coupling. Expanding $E_+ = (E_1 + E_2)/\sqrt{2}$ and $E_- = (E_1 - E_2)/\sqrt{2}$ in terms of the slot modes, and neglecting the cross terms such as $E_1^* \cdot E_2$ due to the small spatial overlap between the fields of the modes localized in separated slots, we again obtain $g_{+-,k} = (g_{1,k} - g_{2,k})/2$.

Consider now the flexural modes of the central nanobeam. At the symmetric ($\{x_{k,eq}\} = 0$) equilibrium position, the nanobeam's in-plane flexural modes are such that $g_1 = -g_2$. Therefore, at the center of the anti-crossing curve g_{+-} is maximal and equal to the linear coupling of the nanobeam mode to the $a_{1,2}$ slot modes. Table 2.3 shows the numerically computed linear cross-mode coupling rate $\tilde{g}_{ij} = g_{ij} x_{\text{zpf}}$ for the fundamental and higher order nanobeam in-plane flexural modes along with their respective frequencies simulated for slot sizes $s_1 = s_2 = 95$ nm using Eq. (2.21). Due to the tight localization of optical modes (see Fig. 2.5) we find there is still significant coupling to higher order flexural modes of frequencies all the way up to 1 GHz. For the numerical simulations of the $a_\pm$ optical supermodes of the double-slotted photonic crystal structure we also find that the radiation-limited optical quality factor is theoretically equal to 5×10^6 and 3×10^5 for the odd and even modes respectively. Therefore, as noted earlier, we can expect mechanical modes of frequencies $\omega_m/2\pi > 300$ MHz to be in the resolved-sideband regime.

2.4.3 Quadratic optomechanical coupling

By extending the perturbation theory to the second order, it is also possible to calculate the x^2-coupling strength. We obtain, for a given optical mode a_i,

$$\delta\omega_i^{(2)} = \frac{3}{8}\omega^{(0)} \left| \frac{\langle E_i^{(0)}| \, \delta\alpha \, |E_i^{(0)}\rangle}{\langle E_i^{(0)}| \, \epsilon^{(0)} \, |E_i^{(0)}\rangle} \right|^2 - \frac{1}{2} \sum_{j \neq i} \frac{{\omega_i^{(0)}}^3}{{\omega_j^{(0)}}^2 - {\omega_i^{(0)}}^2} \frac{\left| \langle E_j^{(0)}| \, \delta\alpha \, |E_i^{(0)}\rangle \right|^2}{\langle E_j^{(0)}| \, \epsilon^{(0)} \, |E_j^{(0)}\rangle \, \langle E_i^{(0)}| \, \epsilon^{(0)} \, |E_i^{(0)}\rangle} \, . \tag{2.22}$$

In the case of the supermodes a_+ and a_- of the symmetric double-slotted photonic crystal structure ($\{x_{k,eq}\} = 0$), the first term vanishes and the only contribution to the x^2-coupling comes from the second term. For optical splittings such that $2J \ll \omega_0$,

$$\delta\omega_+^{(2)}(\{0\}) \equiv_+ \approx -\frac{\omega_+^{(0)}}{(\omega_+^{(0)}+\omega_-^{(0)})(\omega_-^{(0)}-\omega_+^{(0)})} \frac{\left(\omega_+^{(0)}\right)^2 \left|\langle E_-^{(0)}|\,\delta\alpha\,|E_+^{(0)}\rangle\right|^2}{\langle E_-^{(0)}|\,\epsilon^{(0)}\,|E_-^{(0)}\rangle\,\langle E_+^{(0)}|\,\epsilon^{(0)}\,|E_+^{(0)}\rangle}\,, \qquad (2.23)$$
$$\approx \frac{g_{+-}^2}{2J}\,.$$

In Eq. (2.23) we only consider the contribution from the fundamental optical cavity supermodes because the frequency splitting between them is relatively small. Note that another approach [45] has shown that using a large number of spatially overlapping optical modes rather than decreasing the splitting of just two optical modes (as in our case) can also lead to significant x^2-coupling strengths. The values of $\tilde{g}' = g'(x_{\text{zpf}})^2$ are summarized in Table 2.3 for the nanobeam in-plane flexural modes up to 884 MHz. Here we assume an optical $a_\pm$ supermode frequency splitting of $2J/2\pi = 1$ GHz, which is close to the minimum splitting based on the estimated optical quality factors which allows the optical supermodes to be selectively excited and interrogated.

Table 2.3: Linear cross-mode optomechanical (vacuum) coupling rates $\tilde{g}_{+-}$ of the optical supermodes to the nanobeam's in-plane fundamental and higher order flexural modes. The x^2-coupling rate $\tilde{g}'_+$ is inferred using Eq. (2.23) for a minimum splitting of $2J/2\pi = 1$ GHz. The geometric parameters of the nanobeam are the same as in Fig. 2.5.

$\omega_m/2\pi$ [MHz]	$\tilde{g}_{+-}/2\pi$ [kHz]	$\tilde{g}'_+/2\pi$ [Hz]
10.8	1020	1000
56	402	160
130	271	73
227	208	43
340	167	28
467	126	15
605	81	7
746	44	2
884	20	0.4
1025	8	0.07

2.4.4 Coupling coefficients as a function of a static displacement of the nanobeam

In the analysis of the optomechanical coupling coefficients described above in Section 2.4.1-2.4.3 we considered a symmetric double-slotted structure with equal slot widths $s_1 = s_2$ (equilibrium position $\{x_{k,eq}\} = 0$), and thus the calculations were done for the optical supermodes $a_\pm$. In practice, we

could find this symmetric condition by tuning one of the slabs to adjust the relative slots sizes until the optical frequency spectrum was at the center of the anti-crossing curve as shown in Fig. 2.4. Far away from the center of the anti-crossing, however, the optical supermodes correspond more closely to the individual slot modes a_1 and a_2, and we expect different optomechanical coupling strengths. Here we describe how the optomechanical coupling coefficients change upon a large, static displacement of the central nanobeam which takes us far from the symmetric condition near the center of the anti-crossing curve.

From the approximate analytical expression of the supermode dispersion (see Eq. 2.5), we derive here approximate expressions for $g_{\pm,b_3}(x_{3,\text{eq}})$, $g_{+-,b_3}(x_{3,\text{eq}})$ and $g'_{\pm,b_3}(x_{3,\text{eq}})$ as a function of the static displacement amplitude $x_{3,\text{eq}}$ of the fundamental nanobeam mode:

$$g_{\pm,b_3}(x_{3,\text{eq}}) \approx \frac{g_{1,b_3}+g_{2,b_3}}{2} \pm \left(\frac{g_{1,b_3}-g_{2,b_3}}{2}\right)\frac{Z}{\sqrt{1+Z^2}}, \tag{2.24}$$

$$g_{+-,b_3}(x_{3,\text{eq}}) \approx \left(\frac{g_{1,b_3}-g_{2,b_3}}{2}\right)\frac{1}{\sqrt{1+Z^2}}, \tag{2.25}$$

$$g'_{\pm,b_3}(x_{3,\text{eq}}) \approx \pm\,\frac{g^2_{+-,b_3}}{2J}\left[\frac{1}{\sqrt{1+Z^2}}\right]^3, \tag{2.26}$$

where $Z = \left(\left(g_{1,b_3}-g_{2,b_3}\right)/2J\right)x_{3,\text{eq}}$. Note $g_{+-,b_3} \equiv g_{+-,b_3}(x_{3,\text{eq}}=0)$ as per our previously established convention.

As discussed in Sec. 2.3.1, $x_{3,\text{eq}}$ can be approximated by a static displacement $\bar{x}_3$ of the whole nanobeam. Using the perturbative calculation of the optomechanical coupling coefficients from the numerically simulated optical and mechanical fields one can then obtain $g_{\pm,b_3}(\bar{x}_3)$, $g_{+-,b_3}(\bar{x}_3)$ and $g'_{\pm,b_3}(\bar{x}_3)$ by simulating a structure with the nanobeam displaced from its equilibrium position by $\bar{x}_3$ (this becomes the new "unperturbed" structure in our perturbative calculations). Here we consider a structure with nominal slot widths of $s = 90$ nm at equilibrium, and the displacement of the nanobeam from its equilibrium position is swept from $\bar{x}_3 = -3$ nm to $\bar{x}_3 = 3$ nm in steps of 0.5 nm. At each position we calculate the coupling coefficients between the optical supermodes and the fundamental in-plane flexural mode of the nanobeam. The results of these simulations and calculations are plotted in Fig. 2.7. A fit to the numerically calculated coefficients using Eqs. (2.24-2.26) shows very good agreement.

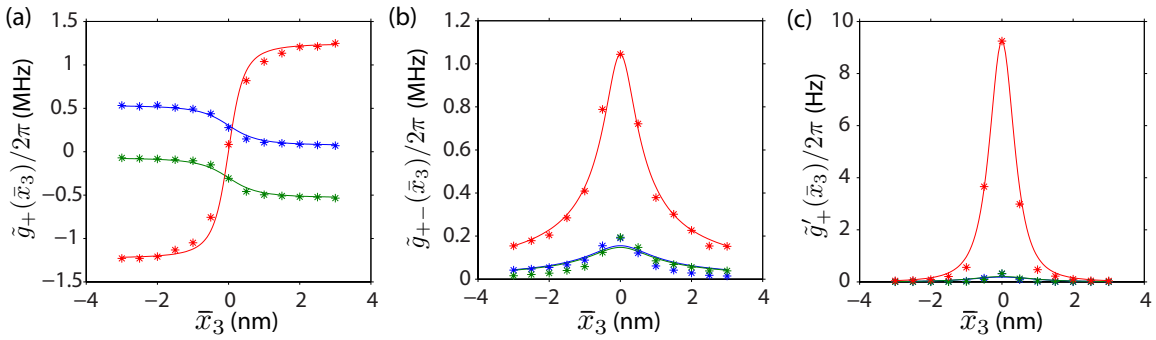

Figure 2.7: **a,** Linear *self-mode* optomechanical coupling, **b** linear *cross-mode* optomechanical coupling, and **c** x^2-coupling of the $\omega_+(\bar{x}_3)$ supermode branch to the fundamental in-plane mechanical resonances of the nanobeam (b_3, red curve) and outer slabs (b_1, blue curve; b_2, green curve). The asterisk ($*$) correspond to numerical FEM simulations of the coupling rates using the perturbation theory with different in-plane static displacement $\bar{x}_3$ of the nanobeam from its symmetric equilibrium position. The geometrical parameters of the simulated double-slotted structure are $(a, r, s_1, s_2) = (480 \text{ nm}, 0.3a, 90 \text{ nm}+\bar{x}_3, 90 \text{ nm}-\bar{x}_3)$. The solid lines are theoretical fits based on Eqs. (2.24-2.26).

These results confirm our previous speculations that far from the symmetric equilibrium position the linear optomechanical coupling is the dominant optomechanical interaction between the optical supermodes and the flexural modes of the central nanobeam, while at symmetric equilibrium position of the beam ($\bar{x}_3 = 0$) the optomechanical interaction is predominantly x^2-coupling. The linear cross-mode coupling between the optical supermodes is also maximal at $\bar{x}_3 = 0$. Experimentally, a static displacement of the whole nanobeam by $\bar{x}_3$ can be mimicked by displacing both outer slabs in the same direction by an amount $\bar{x}_3$. Conversely, a change in the equilibrium slot size can be achieved by displacing both outer slabs in opposite directions. In our recent experimental realization of the double-slotted photonic crystal cavity structure we used this tuning degree of freedom by integrating a set of independent capacitors on the outer slabs. Note that the magnitude of the x^2-coupling in these simulations is limited by the large optical mode splitting ($2J/2\pi = 117$ GHz) of the simulated cavity. With the use of capacitive tuning methods much finer splitting can be realized in practice, however, a larger slot structure was chosen for the simulations to reduce the required mesh size of the structure and to allow for more coarse sweeping of the slot size.

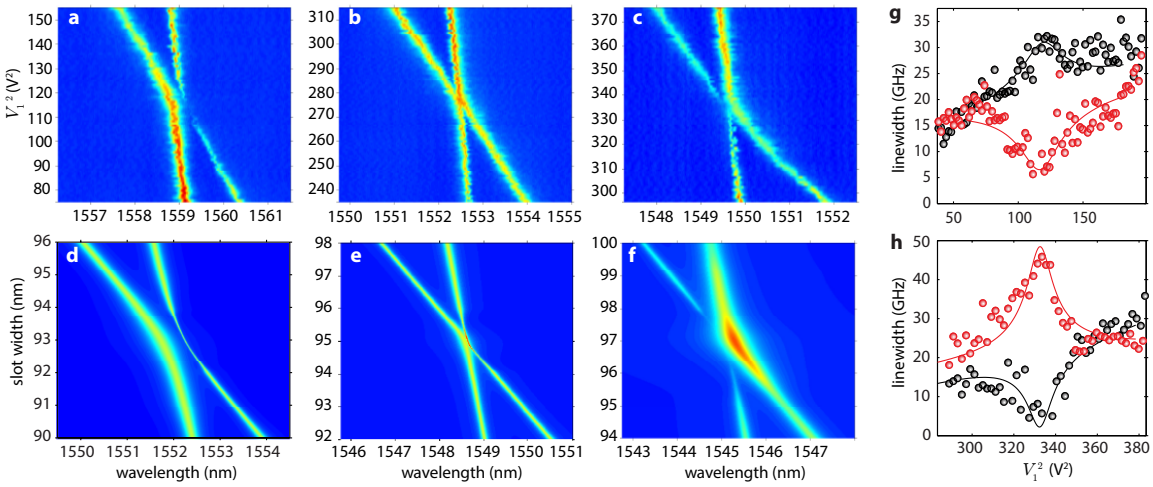

Figure 2.8: **a-c** Optical transmission measurements versus the wavelength of the probe laser showing the cavity mode anti-crossing and tuning of the photon tunneling rate. In these measurements the probe laser wavelength (horizontal axis) is scanned across the optical cavity resonances as the voltage across the first capacitor V_1 is swept from low to high (vertical axis shows V_1^2 in V^2, proportional to slab displacement). The second capacitor is held fixed at $V_2 = 1\mathrm{V}$, **b** $V_2 = 15\mathrm{V}$ and **c** $V_2 = 18\mathrm{V}$. The color scalebar indicates the fractional change in the optical transmission level, ΔT, with blue corresponding to $\Delta T = 0$ and red corresponding to $\Delta T \approx 0.25$. From the three anti-crossing curves we measure a splitting $2J$ equal to **a** 50 GHz, **b** 12 GHz, and **c** -25 GHz. **d-f** Corresponding simulations of the normalized optical transmission spectra for the slot width s_1 varied and the second slot width held fixed at **d** $s_2 = 92$ nm, **e** $s_2 = 95$ nm and **f** $s_2 = 97$ nm. The dispersion and tunneling rate of the slot modes are taken from simulations similar to that found in Fig. 2.4. **g** and **h** show the measured linewidths of the high frequency upper (black) and low frequency lower (red) optical resonance branches as a function of V_1^2, extracted from **a** and **c**, respectively. The narrowing (broadening) is a characteristic of the odd (even) nature of the cavity supermode, indicating the inversion of the even and odd supermodes for the two voltage conditions $V_2 = 1$ V and $V_2 = 18$ V. The lines are guides for the eye.

2.5 Experimental measurements

Optical testing of the fabricated devices is performed in a nitrogen-purged enclosure at room temperature and pressure. A dimpled optical fiber taper is to locally excite and collect light from the photonic crystal cavity, details of which can be found in Ref. [64]. The light from a tunable, narrow-bandwidth laser source in the telecom 1550 nm wavelength band (New Focus, Velocity series) is evanescently coupled from the fiber taper into the device with the fiber taper guiding axis parallel with that of the photonic crystal waveguide axis, and the fiber taper positioned laterally at the center of the nanobeam and vertically a few hundreds of nanometers above the surface of the silicon chip. Relative positioning of the fiber taper to the chip is accomplished using a multi-axis set of encoded

DC-motor stages with 50 nm step resolution. The polarization of the light in the fiber is polarized parallel with the surface chip in order to optimize the coupling to the in-plane polarization of the cavity modes.

With the taper placed suitably close to a photonic crystal cavity (200 nm), the transmission spectrum of the laser probe through the device features resonance dips at the supermode resonance frequencies, as shown in the intensity plots of Figs. 2.8a-c. The resonance frequency of the cavity modes are tuned via displacement of the top and bottom photonic crystal slabs, which can be actuated independently using their respective capacitor voltages V_1 and V_2. The capacitive force is proportional to the applied voltage squared [56], and thus increasing the voltage V_i on a given capacitor widens the waveguide slot s_i and (predominantly) increases the slot mode frequency a_i (note the other optical slot mode also increases slightly). For the devices studied in this work, the slab tuning coefficient with applied voltage (α_{cap}) is estimated from SEM analysis of the resulting structure dimensions and FEM electromechanical simulations to be $\alpha_{\text{cap}} = 25$ pm/V^2.

We fabricated devices with slot widths targeted for a range of 75-85 nm, chosen smaller than the expected zero-splitting slot width of $s = 95$ nm so that the capacitors could be used to tune through the zero-splitting point. While splittings larger than 150 GHz were observed in the nominal 85 nm slot width devices, splittings as small as 10 GHz could be resolved in the smaller 75 nm slot devices. As such, in what follows we focus on the results from a single device with as-fabricated slot size of $s \approx 75$ nm.

2.5.1 Anti-crossing measurements

Figure 2.8 shows intensity plots of the normalized optical transmission through the optical fiber taper when evanescently coupled to the photonic crystal cavity of a device with nominal slot width $s = 75$ nm. Here a series of optical transmission spectrum are measured by sweeping the probe laser frequency and the voltage V_1, with V_2 fixed at three different values. The estimated anti-crossing splitting from the measured dispersion of the cavity supermodes is $2J/2\pi = 50$ GHz, 12 GHz, and -25 GHz for $V_2 = 1$ V, 15 V, and 18 V, respectively. In order to distinguish between the odd and even cavity supermodes at the anti-crossing point, we use the fact that both the coupling rate to the fiber taper κ_e and the intrinsic linewidth κ_i depend upon the symmetry of the cavity mode. First,

the odd mode becomes dark at the anti-crossing because it cannot couple to the symmetric fiber taper mode. Second, in the vicinity of the anti-crossing point the linewidth of the odd mode narrows while the linewidth of the even mode broadens. Far from the anti-crossing region, the branches are asymptotic to individual slot modes and their linewidths and couplings to the fiber taper are similar.

These features are clearly evident in the optical transmission spectra of Figs. 2.8a-c, as well as in the measured linewidth of the optical supermode resonances shown in Figs. 2.8g-h. Figure 2.8a was taken with a small voltage $V_2 = 1$ V, corresponding to a small slot width at the anti-crossing point, and thus consistent with the even mode frequency being higher than the odd mode frequency for small slot widths (c.f., Fig. 2.4b). The exact opposite identification is made in Fig. 2.8c where $V_2 = 18$ V is much larger, corresponding to a larger slot width at the anti-crossing point. Fig. 2.8b with $V_2 = 15$ V is close to the zero-splitting condition. For comparison, a simulation of the expected anti-crossing curves are shown in Figs. 2.8d, e, and f for $s_2 = 92$, 95, and 97 nm, respectively. Here we have taken the even superposition of the slot modes to have a lower Q-factor than the odd superposition of the slot modes, and the coupling of the fiber taper to be much stronger to the even mode than the odd mode, consistent with results from numerical FEM simulations. Good correspondence with the measured transmission curves of Figs. 2.8a-c are found after accounting for an overall 4.5 nm wavelength shift.

An estimate of the x^2-coupling coefficient g'_{b_3} can found from the simulated value of α_{cap} and a fit to the measured tuning curves of Fig. 2.8 away from the anti-crossing point. Consider the anti-crossing curve of Fig. 2.8b with the smallest splitting. Far from the anti-crossing point the tuning of the a_1 and a_2 slot modes are measured to be linear with the square of V_1: $\bar{g}_{a_1,V_1^2}/2\pi = 3.9$ GHz/V^2 and $\bar{g}_{a_2,V_1^2}/2\pi = 0.5$ GHz/V^2. For the simulated value of $\alpha_{\text{cap}} = 0.025$ nm/V^2 the corresponding linear dispersive coefficients versus the first slot width are $\bar{g}_{a_1,\delta s_1}/2\pi = 156$ GHz/nm and $\bar{g}_{a_2,\delta s_1}/2\pi = 20$ GHz/nm. Noting that a displacement amplitude x_3 for the fundamental in-plane mechanical mode of the central nanobeam is approximately equivalent to a reduction in the width of one slot by -x_3 and an increase in the other slot by +x_3, the linear optomechanical coupling coefficient between optical slot mode a_1 and mechanical mode b_3 is estimated to be $g_{a_1,b_3} \approx (\bar{g}_{a_1,\delta s_1} + \bar{g}_{a_1,-\delta s_2}) = (\bar{g}_{a_1,\delta s_1} - \bar{g}_{a_2,\delta s_1}) = 2\pi[136$ GHz/nm$^2]$, where by symmetry $\bar{g}_{a_1,-\delta s_2} = -\bar{g}_{a_2,\delta s_1}$. Along with a measured splitting of $2J/2\pi = 12$ GHz, this yields through

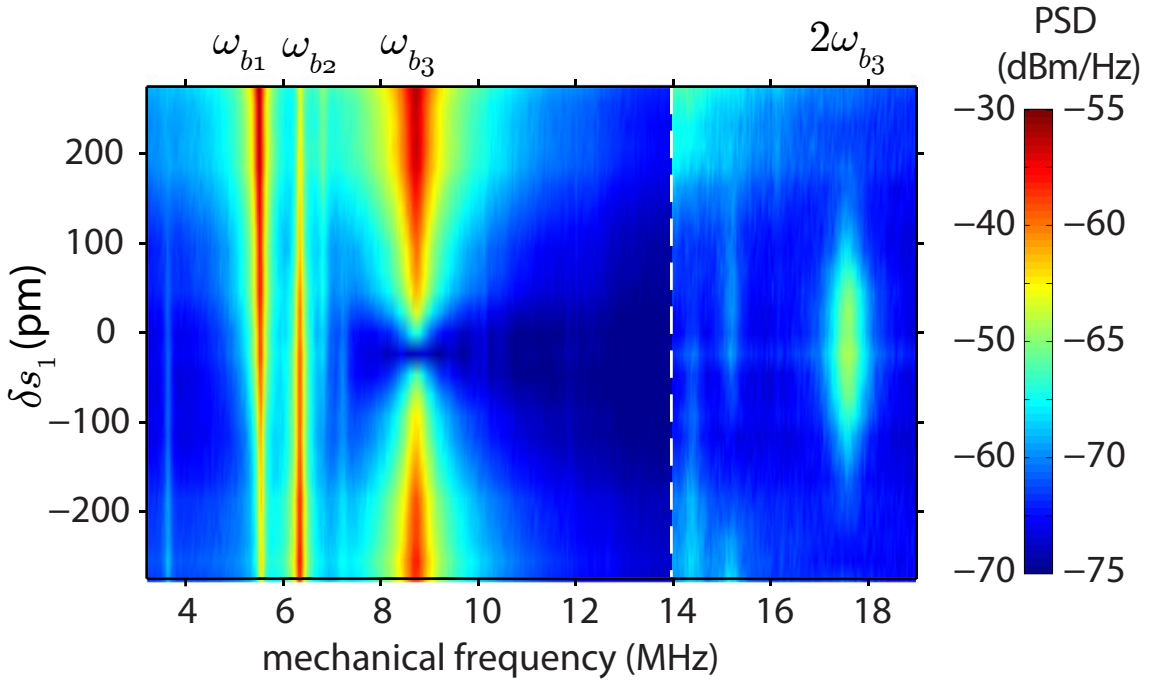

Figure 2.9: RF photocurrent noise spectrum for the optically transmitted light past the double-slotted photonic crystal cavity. Here the applied voltage $V_2 = 1$ V is held fixed and V_1 is swept from just below to just above the anti-crossing point of Fig. 2.8a. In these measurements the probe laser power is 10 μW at the input to the cavity, the probe laser frequency is set on the blue side of the upper frequency supermode resonance, $\Delta_L \approx \kappa/2\sqrt{3}$, and the fiber taper is placed in the near-field of the photonic crystal cavity resulting in an on-resonance dip in transmission of approximately $\Delta T = 15\%$. The vertical axis in this plot is converted to a change in the slot width, δs_1, using the numerically simulated value of $\alpha_{\text{cap}} = 0.025$ nm/V^2. The color indicates the magnitude of the RF noise in dBm/Hz, where the colorscale from 0-14 MHz is shown on the left of the scalebar and the colorscale from 14-20 MHz is shown on the right of the scalebar (a different scale is used to highlight the noise out at $2\omega_{b_3}$).

Eq. (2.6) an estimate for the x^2-coupling coefficient of $g'_{b_3}/2\pi \approx 1.54$ THz/nm^2.

2.5.2 Transduction of mechanical motion

Figure. 2.9a shows the evolution of the optically-transduced mechanical noise power spectral density (NPSD) near the anti-crossing region of Fig. 2.8a. In this plot s_2 is fixed and s_1 is varied over an estimated range of $\delta s_1 = \pm 0.3$ nm around the anti-crossing. Optical motion is imprinted as intensity modulations of the probe laser which is tuned to the blue side of the upper frequency supermode. Here we choose the detuning point corresponding to $\Delta_L \equiv \omega_L - \omega_+ \approx \kappa/2\sqrt{3}$, where ω_L is the

probe laser frequency and κ is the full-width at half-maximum linewidth of the optical resonance. This detuning choice ensures maximal, linear transduction of small fluctuations in the frequency of the cavity supermode, which allows us to relate nonlinear transduction of motion with true nonlinear optomechanical coupling [44, 45]. A probe power of $P_{\text{in}} = 10\ \mu$W is used in order to avoid any nonlinear effects due to optical absorption, and the transmitted light is first amplified through an erbium-doped fiber amplifier before being detected on a high gain photoreceiver (transimpedance gain 4×10^4, NEP$= 2.5$ pW/Hz$^{1/2}$, bandwidth 125 MHz). The resulting radio-frequency (RF) photocurrent noise spectrum is plotted in Fig. 2.9.

In order to identify the measured noise peaks, numerical FEM simulations of the mechanical properties of the double-slotted structure were performed. Taking structural dimensions from SEM images, the simulated mechanical frequency for the fundamental in-plane resonances of the two outer slabs (b_1 and b_2) is found to be $\omega_m/2\pi = 6$MHz. An effective motional mass for the slab modes of $m_{\text{eff}} = 36$ pg was determined by integrating, over the volume of the structure, the mass density of the silicon slab weighted by the normalized, squared displacement amplitude of the slab's motion [65]. The corresponding estimate of the zero-point amplitude of the slab modes is given by $x_{\text{zpf}} \equiv (\hbar/2m_{\text{eff}}\omega_m)^{1/2} = 5.3$ fm. The resonance frequency, effective motional mass, and zero-point amplitude for the fundamental in-plane resonance of the central nanobeam (b_3) are simulated to be $\omega_m/2\pi = 10$MHz, $m = 6$ pg, and $x_{\text{zpf}} = 16$ fm, respectively.

Comparing to Fig. 2.9a, the two lowest frequency noise peaks are thus identified due to the thermal motion of the b_1 and b_2 modes of the outer slabs, with $\omega_{b_1}/2\pi = 5.54$ MHz and $\omega_{b_2}/2\pi = 6.34$ MHz. The identification of the b_1 mode with the lower frequency mechanical resonance is made possible due to the increasing signal transduction of this resonance as s_1 is increased above the anti-crossing point. Since we are probing the upper frequency optical supermode, for $s_1 > s_2$ ($\delta s_1 > 0$) the supermode is approximately a_1 which is localized to slot 1 and sensitive primarily to the motion of b_1. We see an opposite trend for the b_2 resonance, with larger transduction gain for $s_1 < s_2$ ($\delta s_1 < 0$).

The noise peak at $\omega_m/2\pi = 8.73$ MHz behaves altogether differently than the b_1 and b_2 resonances. This noise peak is transduced with roughly equal signal levels for $\delta s_1 > 0$ and $\delta s_1 < 0$, but significantly drops in strength for $\delta s_1 \approx 0$ near the anti-crossing. This is the expected characteristic

of the b_3 mode, where the dispersive linear optomechanical coupling to the b_3 should vanish at the anti-crossing point. Also shown in Fig. 2.9a is the noise at $2\omega_{b_3} \approx 17.5$ MHz, which shows a weakly transduced resonance with signal strength peaked around $\delta s_1 = 0$. The suppression in transduction of the noise peak at ω_{b_3} concurrent with the rise in transduction of the noise peak at $2\omega_{b_3}$ is a direct manifestation of the transition from linear (g_{a_1,b_3} or g_{a_2,b_3}) to position-squared (g'_{b_3}) optomechanical coupling.

2.5.3 Static and dynamic optical spring measurements

Our previous estimate of g'_{b_3} from the anti-crossing curves relied on the approximate correspondence between the static displacement of the outer slabs and the fundamental in-plane vibrational amplitude of the b_3 mode of the central nanobeam. A more accurate determination of the true x^2-coupling coefficient to b_3 can be determined from two different optical spring measurements. Far from the anti-crossing one can determine the linear optomechanical coupling coefficient between the optical slot modes and the b_3 mechanical mode from the dynamic back-action of the intra-cavity light field on the mechanical frequency, which in conjunction with the measured anti-crossing splitting yields g'_{b_3} via Eq. (2.6). A direct measurement of $\tilde{g}'_{b_3}$ can also be obtained from the static optical spring effect near the anti-crossing point as indicated in Eq. (2.8).

Figure 2.10a shows the dependence of the mechanical resonance frequency of the b_3 mode of the central nanobeam versus the laser detuning Δ_L when the device is tuned far from the anti-crossing point in Fig. 2.8a ($V_1 \approx 12$ V and $V_2 = 1$ V). In these measurements the probe laser power is fixed at $P_{\text{in}} = 10$ μW and the laser frequency is scanned across the upper optical supermode resonance, which away from the anti-crossing point in this case is the slot-mode a_1. In the sideband unresolved regime ($\omega_m \ll \kappa$), the dynamic optical spring effect has a dispersive lineshape centered around the optical resonance frequency, with optical softening of the mechanical resonance occurring for red detuning ($\Delta_L < 0$) and optical stiffening occurring for blue detuning ($\Delta_L > 0$).

A fit to the measured frequency shift versus Δ_L is performed using the linear optomechanical coupling rate $\tilde{g}_{a_1,b_3}$ as a fit parameter. The resulting optomechanical coupling rate which best fits the data is shown in Figure 2.10a as a red curve, and corresponds to $\tilde{g}_{a_1,b_3}/2\pi = 1.72$ MHz. Using $x_{\text{zpf}} = 16$ fm for the b_3 mechanical mode, this corresponds to $g_{a_1,b_3}/2\pi = 107$ GHz/nm. Note that

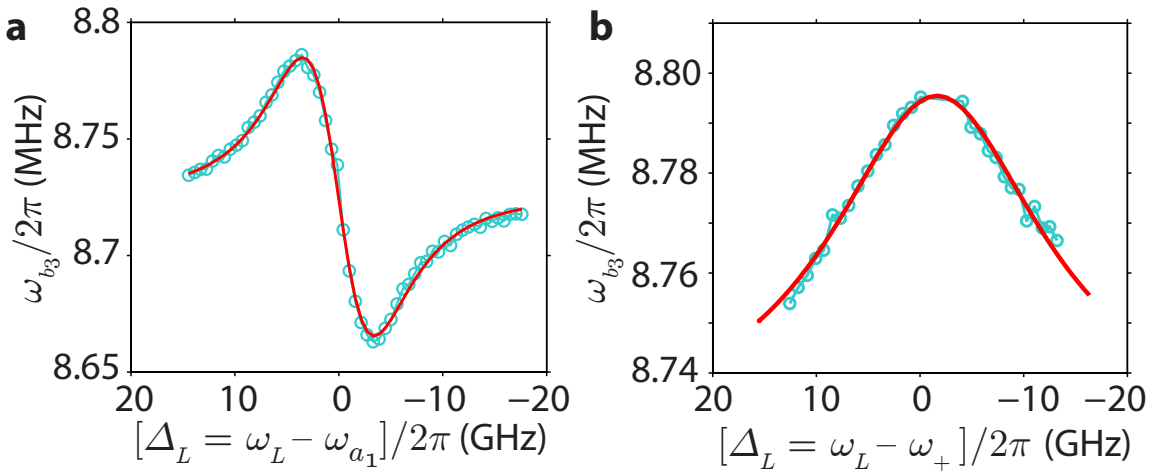

Figure 2.10: **a,** Dynamic optical spring effect measured by exciting the upper frequency supermode resonance far from the anti-crossing point ($\sim a_1$ mode) [$P_{\text{in}} = 10$ μW, $\kappa = 12.5$ GHz, $\Delta T \approx 10\%$]. **b,** Static optical spring shift of the b_3 resonance frequency versus laser detuning Δ_L from the upper ($\sim a_+$) supermode resonance near the anti-crossing point (V_1 is adjusted such that the device is approximately 1 V^2 from the anti-crossing point in Fig. 2.8a) [$P_{\text{in}} = 50$ μW, $\kappa = 26$ GHz, $\Delta T \approx 25\%$]. In both **a** and **b** V_2 is fixed at 1 V (see Fig. 2.8a) and the measured data (circles) correspond to a Lorentzian fit to the resonance freqency of the optically transduced thermal noise peak at ω_{b_3}. In **a** the red curve is a fit to the data using a dynamical optical spring model [65] with linear optomechanical coupling coefficient $\tilde{g}_{a_1,b_3}/2\pi = 1.72$ MHz. In **b** the red curve is a fit to the data using a static spring model (c.f., Eq. (2.8) with x^2-coupling coefficient $\tilde{g}'_{b_3}/2\pi = 46$ Hz. In both the spring models of **a** and **b** the intra-cavity photon number versus detuning $n(\Delta_L)$ is calibrated from the known input laser power, cavity linewidth, and on-resonance transmission contrast.

this is slightly smaller than the value measured indirectly from the dispersion in the anti-crossing curve of Fig. 2.8; however, that value relied on the simulated value for α_{cap}, which is quite sensitive to the actual fabricated dimensions and stiffness of the structure. For the smallest splitting measured in this work ($2J/2\pi = 12$ GHz), we get an estimated value for the x^2-coupling to the b_3 mode from the dynamic optical spring measurements of $\tilde{g}'_{b_3}/2\pi = 245$ Hz ($g'_{b_3}/2\pi = 0.96$ THz/nm^2).

An entirely different dynamics occurs at the anti-crossing point where x^2 optomechanical coupling dominates. Optical pumping of the supermode resonances near the anti-crossing point gives rise to a static optical spring shift which depends on the average, instantaneous value of the intra-cavity photon number. Due to the opposite sign of the quadratic dispersion of the upper and lower optical supermode branches, optical pumping of the upper branch resonance leads to a stiffening of the mechanical structure whereas optical pumping of the lower branch leads to a softening of the structure [44, 66]. The measured frequency shift of the b_3 mechanical resonance for optical pumping

of the upper branch cavity supermode (the even a_+ mode in this case) is shown in Fig. 2.10b for a voltage setting on the capacitor electrodes of $V_1 = 10.6$ V and $V_2 = 1$ V. This position is slightly below the exact center of the anti-crossing point of Fig. 2.8a so as to allow weak linear transduction of the b_3 resonance. A rather large supermode splitting of $2J/2\pi = 50$ GHz was also chosen to ensure that only the even a_+ supermode is excited, and that the contribution to the optical trapping (anti-trapping) by the lower branch a_- resonance is negligible.

As per Eq. (2.8), the mechanical frequency shift is approximately given by $\Delta\omega_m(\Delta_L) \approx 2\tilde{g}'_{b_3} n_+(\Delta_L)$, where $n_+(\Delta_L)$ is the average intra-cavity photon number in the a_+ supermode. Fitting this model to the data measured in Fig. 2.10b yields a value of $\tilde{g}'_{b_3} = 46$ Hz. This is slightly lower than the 60 Hz value expected for a splitting of $2J/2\pi = 50$ GHz and the linear coupling rate of $\tilde{g}_{a_1,b_3}/2\pi = 1.72$ MHz determined from the dynamical optical spring effect, but consistent with our slight detuning of the structure from the exact center of the anti-crossing.

Chapter 3

Theory of Sideband-resolved Electromechanical System

This chapter will develop the basic theoretical framework to understand the electromechanical interaction specifically in the sideband resolved regime. A thorough development of the theory leading up to what is required to understand the physics behind the measurements is presented.

3.1 Reflective coupling to a microwave resonator

We consider a resonator mode $\hat{a}$ at frequency ω_r, which is coupled to a single waveguide with coupling strength κ_e, and to the environment with the coupling strength κ_i (see Fig. 3.1). We follow general input-output theory [67] to write the time derivative of the annihilation operator

$$\dot{\hat{a}}(t) = -\left(i\omega_r + \frac{\kappa}{2}\right)\hat{a}(t) - \sqrt{\kappa_e}\hat{a}_{\text{in}}(t) - \sqrt{\kappa_i}\hat{a}_{b,r}(t) - \sqrt{\kappa_e}\hat{a}_{b,\text{wg}}(t), \tag{3.1}$$

where $\kappa = \kappa_e + \kappa_i$ is the total resonator linewidth, $\hat{a}_{\text{in}}(t)$ represents the annihilation operator of the coherent input mode, $\hat{a}_{b,\text{wg}}(t)$ the waveguide mode operator, and $\hat{a}_{b,r}(t)$ is the respective field operator of the resonator environment. We take the Fourier transform to remove the time derivative, and simplify to get the frequency dependence

$$\hat{a}(\omega) = \frac{-\sqrt{\kappa_e}\hat{a}_{\text{in}}(\omega) - \sqrt{\kappa_i}\hat{a}_{b,r}(\omega) - \sqrt{\kappa_e}\hat{a}_{b,\text{wg}}(t)}{\kappa/2 + i(\omega_r - \omega)}. \tag{3.2}$$

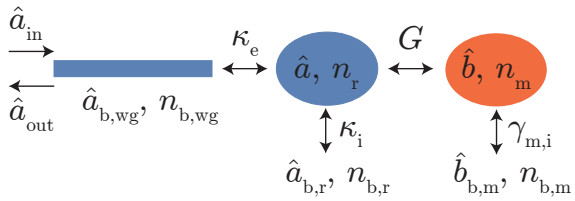

Figure 3.1: **System modes, coupling rates and noise baths.** In the reflective geometry the microwave cavity mode $\hat{a}$ is coupled to the coherent waveguide modes $\hat{a}_{\rm in}$ and $\hat{a}_{\rm out}$ with the external coupling strength κ_e. It is also coupled to a bath of noise photons, ideally at the refrigerator temperature $n_{b,r}$, with the intrinsic coupling strength κ_i. In addition, the waveguide bath mode $\hat{a}_{b,\rm wg}$ can be populated with thermal noise photons $n_{b,\rm wg}$, which also couples with κ_e. The mechanical resonator mode $\hat{b}$ is coupled to the microwave resonator with the parametrically enhanced electromechanical coupling strength G. In addition, it is coupled to a bath of noise phonons, ideally at the refrigerator temperature $n_{b,m}$, with the intrinsic coupling rate $\gamma_{m,i}$.

The resonator output field is defined as

$$\begin{aligned}\hat{a}_{\rm out}(\omega) &= \hat{a}_{\rm in}(\omega) + \sqrt{\kappa_e}\hat{a}(\omega) \\ &= \hat{a}_{\rm in}(\omega) + \frac{-\kappa_e\hat{a}_{\rm in}(\omega) - \sqrt{\kappa_e\kappa_i}\hat{a}_{b,r}(\omega) - \kappa_e\hat{a}_{b,\rm wg}(t)}{\kappa/2 + i(\omega_r - \omega)},\end{aligned} \tag{3.3}$$

which we can use to calculate the complex scattering parameter as measured by a network analyzer

$$S_{11}(\omega) = \frac{\langle\hat{a}_{\rm out}(\omega)\rangle}{\langle\hat{a}_{\rm in}(\omega)\rangle} = 1 - \frac{\kappa_e}{\kappa/2 + i(\omega_r - \omega)}, \tag{3.4}$$

where the incoherent bath mode terms drop out. We use this function to simultaneously fit the real and imaginary part of the measured cavity response and extract the intrinsic and extrinsic cavity coupling rates.

3.1.1 Derivation of intra-cavity photon number

It is useful to define the intra-cavity photon number n_d due to a classical coherent drive tone at frequency ω_d. This classical coherent drive is used to parametrically enhance the interaction between the cavity and the mechanical oscillator as it will be explained later. We replace the field operators in Eq. 3.2 with the classical amplitudes $\hat{a}(\omega) \to \alpha(\omega)$ and discard the resonator and waveguide bath modes to get

$$n_d = |\alpha_{\rm d}|^2 = |\alpha_{\rm in}|^2 \frac{4\kappa_e}{\kappa^2 + 4\Delta_{r,d}^2}. \tag{3.5}$$

Here we have introduced the resonator drive detuning $\Delta_{r,d} = \omega_r - \omega_d$ and the input photon flux $|\alpha_{\text{in}}|^2 = P_{\text{in}}/(\hbar\omega_d)$. The power at the cavity input can be expressed as $P_{\text{in}} = 10^{-3}10^{(\mathcal{A}+P_{\text{d}})/10}$ with P_{d} being the drive power in dBm and $\mathcal{A}$ the total attenuation of the input signal in dB due to the losses from the source to the sample.

3.1.2 Asymmetric lineshape

The measured spectra of the cavity does not always have the shape of a symmetric lorentzian and shows fano-features. Fano line shapes generally originate from interference between a resonant mode and a background mode [68]. Experimental imperfections, such as leakage or reflections in the feedline circuit, can lead to such asymmetric cavity line shapes. We can model this effect by introducing a complex valued external resonator to waveguide coupling parameter $\bar{\kappa}_{\text{e}} = |\kappa_e|e^{-iq}$, where q is a version of the Fano parameter. While small q values do not change the magnitude of the inferred external coupling (or the drive photon number), they correctly model small asymmetries in the Lorentzian cavity response [69]. For simplicity we define the generalized coupling $\bar{\kappa}_{\text{e}} = \kappa_e - iq$ and substitute into Eq. 3.4, to get the generalized resonator line shape

$$S_{11}(\omega) = 1 - \frac{\kappa_e - iq}{\kappa/2 - i(\omega_r - \omega)}. \tag{3.6}$$

3.2 Derivation of cavity electromechanical response functions

In this section we follow previous work [21, 70–72] to calculate the coherent response and the full noise spectrum of the system. In contrast to earlier treatments we also include thermal noise in the feedline circuit, which gives rise to an increased mechanical occupation and an asymmetric cavity noise line shape.

The Hamiltonian of the coupled microwave cavity-mechanical system (see Fig. 3.1) can be written as

$$\hat{H} = \hbar\omega_r\hat{a}^\dagger\hat{a} + \hbar\omega_m\hat{b}^\dagger\hat{b} + \hbar g_0\hat{a}^\dagger\hat{a}(\hat{b}^\dagger + \hat{b}), \tag{3.7}$$

where $\hat{b}$ ($\hat{b}^\dagger$) is the annihilation (creation) operator of the mechanical mode at frequency ω_m, and g_0 is the electromechanical coupling strength, *i.e.*, the resonator frequency shift due to a mechanical

displacement corresponding to half a phonon on average. We excite the microwave resonator mode using a strong drive tone at frequency $\omega_{\rm d}$, detuned from the resonator frequency by $\Delta_{r,d} = \omega_r - \omega_d$. The linearized Hamiltonian in the rotating frame is then given as

$$\hat{H}' = -\hbar\Delta_{r,d}\hat{a}^\dagger\hat{a} + \hbar\omega_m\hat{b}^\dagger\hat{b} + \hbar G(\hat{a}^\dagger + \hat{a})(\hat{b}^\dagger + \hat{b}), \tag{3.8}$$

where $G = \sqrt{n_{\rm d}}g_0$ is the parametrically enhanced optomechanical coupling strength. The linearized Langevin equations are given as

$$\dot{\hat{a}}(t) = -\left(i\Delta_{r,d} + \frac{\kappa}{2}\right)\hat{a}(t) - iG(\hat{b}(t) + \hat{b}^\dagger(t)) - \sqrt{\kappa_e}\hat{a}_{\rm in}(t) - \sqrt{\kappa_i}\hat{a}_{b,r}(t) - \sqrt{\kappa_e}\hat{a}_{b,{\rm wg}}(t) \tag{3.9}$$

$$\dot{\hat{b}}(t) = -\left(i\omega_m + \frac{\gamma_{m,i}}{2}\right) - iG(\hat{a}^\dagger(t) + \hat{a}(t)) - \sqrt{\gamma_{m,i}}\hat{b}_{b,m}(t). \tag{3.10}$$

Taking the Fourier transform and simplifying we obtain

$$\chi_{\rm r}^{-1}(\omega)\hat{a}(\omega) = -iG(\hat{b}(\omega) + \hat{b}^\dagger(\omega)) - \sqrt{\kappa_e}\hat{a}_{\rm in}(\omega) - \sqrt{\kappa_{\rm i}}\hat{a}_{b,r}(\omega) \tag{3.11}$$

$$\widetilde{\chi}_{\rm r}^{-1}(\omega)\hat{a}^\dagger(\omega) = iG(\hat{b}(\omega) + \hat{b}^\dagger(\omega)) - \sqrt{\kappa_e}\hat{a}^\dagger_{\rm in}(\omega) - \sqrt{\kappa_{\rm i}}\hat{a}^\dagger_{b,r}(\omega) \tag{3.12}$$

$$\chi_{\rm m}^{-1}(\omega)\hat{b}(\omega) = -iG(\hat{a}(\omega) + \hat{a}^\dagger(\omega)) - \sqrt{\gamma_{m,i}}\hat{b}_{b,m}(\omega) \tag{3.13}$$

$$\widetilde{\chi}_{\rm m}^{-1}(\omega)\hat{b}^\dagger(\omega) = iG(\hat{a}(\omega) + \hat{a}^\dagger(\omega)) - \sqrt{\gamma_{m,i}}\hat{b}^\dagger_{b,m}(\omega), \tag{3.14}$$

where we have introduced the uncoupled susceptibilities of the cavity and the mechanical mode

$$\chi_{\rm r}^{-1}(\omega) = \kappa/2 + i(\Delta_{r,d} - \omega) \tag{3.15}$$

$$\widetilde{\chi}_{\rm r}^{-1}(\omega) = \kappa/2 - i(\Delta_{r,d} + \omega) \tag{3.16}$$

$$\chi_{\rm m}^{-1}(\omega) = \gamma_{m,i}/2 + i(\omega_m - \omega) \tag{3.17}$$

$$\widetilde{\chi}_{\rm m}^{-1}(\omega) = \gamma_{m,i}/2 - i(\omega_m + \omega). \tag{3.18}$$

In the sideband resolved limit $\omega_m \gg \kappa, G$, and for positive detuning of the drive tone $\Delta_{r,d} \approx \omega_m$

(red side pumping), the linearized Langevin equations can be written approximately as

$$\hat{a}(\omega) = \frac{iG\chi_{\mathrm{m}}\chi_{\mathrm{r}}\sqrt{\gamma_{m,i}}\hat{b}_{b,m}(\omega) - \chi_{\mathrm{r}}(\sqrt{\kappa_e}\hat{a}_{\mathrm{in}}(\omega) + \sqrt{\kappa_i}\hat{a}_{b,r}(\omega) + \sqrt{\kappa_e}\hat{a}_{b,\mathrm{wg}}(\omega))}{1 + G^2\chi_{\mathrm{m}}\chi_{\mathrm{r}}} \tag{3.19}$$

$$\hat{b}(\omega) = \frac{-\chi_{\mathrm{m}}\sqrt{\gamma_{m,i}}\hat{b}_{b,m}(\omega) - iG\chi_{\mathrm{m}}\chi_{\mathrm{r}}(\sqrt{\kappa_e}\hat{a}_{\mathrm{in}}(\omega) + \sqrt{\kappa_i}\hat{a}_{b,r}(\omega) + \sqrt{\kappa_e}\hat{a}_{b,\mathrm{wg}}(\omega))}{1 + G^2\chi_{\mathrm{m}}\chi_{\mathrm{r}}}. \tag{3.20}$$

Now we can calculate the cavity output mode:

$$\begin{aligned}\hat{a}_{\mathrm{out}}(\omega) &= \hat{a}_{\mathrm{in}}(\omega) + \sqrt{\kappa_e}\hat{a}(\omega) \\ &= \hat{a}_{\mathrm{in}}(\omega) - (\hat{a}_{\mathrm{in}}(\omega) + \hat{a}_{b,\mathrm{wg}}(\omega))\frac{\kappa_e\chi_{\mathrm{r}}}{1 + G^2\chi_{\mathrm{m}}\chi_{\mathrm{r}}} - \hat{a}_{b,r}(\omega)\frac{\sqrt{\kappa_e\kappa_i}\chi_{\mathrm{r}}}{1 + G^2\chi_{\mathrm{m}}\chi_{\mathrm{r}}} \\ &+ \hat{b}_{b,m}(\omega)\frac{iG\sqrt{\kappa_e\gamma_{m,i}}\chi_{\mathrm{m}}\chi_{\mathrm{r}}}{1 + G^2\chi_{\mathrm{m}}\chi_{\mathrm{r}}}.\end{aligned} \tag{3.21}$$

3.3 Electromagnetically Induced Transparency

We first calculate the coherent part of the system response using Eq. 3.21 and drop incoherent noise terms to get

$$S_{11}(\omega) = \frac{\langle\hat{a}_{\mathrm{out}}(\omega)\rangle}{\langle\hat{a}_{\mathrm{in}}(\omega)\rangle} = 1 - \frac{\kappa_e\chi_{\mathrm{r}}}{1 + G^2\chi_{\mathrm{m}}\chi_{\mathrm{r}}}. \tag{3.22}$$

Substituting the bare response of the cavity and the mechanical oscillator we get the coherent EIT response function valid for small probe drive strengths

$$S_{11}(\omega) = 1 - \frac{\kappa_e}{\kappa/2 + i(\Delta_{r,d} - \omega) + \frac{G^2}{\gamma_{m,i}/2 + i(\omega_m - \omega)}}. \tag{3.23}$$

In order to take into account potential interference with a continuum of parasitic modes, we can follow the procedure outlined above. Substituting $\kappa_e \to \kappa_e - iq$ we get

$$S_{11,\mathrm{as}}(\omega) = 1 - \frac{\kappa_e - iq}{\kappa/2 + i(\Delta_{r,d} - \omega) + \frac{G^2}{\gamma_{m,i}/2 + i(\omega_m - \omega)}}, \tag{3.24}$$

which can be used to fit asymmetric EIT spectra.

3.4 Quantum derivation of observed noise spectra

Using the Fourier transforms defined above, we can write the spectral density of an operator $\hat{A}$ as

$$S_{AA}(t) = \int_{-\infty}^{+\infty} d\tau e^{i\omega\tau} \left\langle \hat{A}^\dagger(t+\tau)\hat{A}(t) \right\rangle \tag{3.25}$$

$$S_{AA}(\omega) = \int_{-\infty}^{+\infty} d\omega' \left\langle \hat{A}^\dagger(\omega)\hat{A}(\omega') \right\rangle . \tag{3.26}$$

The auto-correlation function of the detected normalized field amplitude (or the photo current) of the output mode $\hat{I}(t) = \hat{a}_{\text{out}}(t) + \hat{a}^\dagger_{\text{out}}(t)$ is then given as

$$S_{II} = \int_{-\infty}^{+\infty} d\omega' \left\langle \left(\hat{a}_{\text{out}}(\omega) + \hat{a}^\dagger_{\text{out}}(\omega) \right) \left(\hat{a}_{\text{out}}(\omega') + \hat{a}^\dagger_{\text{out}}(\omega') \right) \right\rangle . \tag{3.27}$$

Substituting $\hat{a}_{\text{out}}(\omega)$ and $\hat{a}^\dagger_{\text{out}}(\omega)$ from Eq. 3.21 we find a general expression for the single sided noise spectrum

$$\begin{aligned} S(\omega) = n_{b,\text{wg}} \left| \left(1 - \frac{\kappa_e \widetilde{\chi}_\text{r}}{1 + G^2 \widetilde{\chi}_\text{m} \widetilde{\chi}_\text{r}} \right) \right|^2 + n_{b,r} \frac{|\kappa_e \kappa_i \widetilde{\chi}_\text{r}|^2}{|1 + G^2 \widetilde{\chi}_\text{m} \widetilde{\chi}_\text{r}|^2} + n_{b,m} \frac{\kappa_e \gamma_{m,i} G^2 |\widetilde{\chi}_\text{m}|^2 |\widetilde{\chi}_\text{r}|^2}{|1 + G^2 \widetilde{\chi}_\text{m} \widetilde{\chi}_\text{r}|^2} \\ + (n_{b,\text{wg}} + 1) \left| \left(1 - \frac{\kappa_e \chi_\text{r}}{1 + G^2 \chi_\text{m} \chi_\text{r}} \right) \right|^2 + (n_{b,r} + 1) \frac{\kappa_e \kappa_i |\chi_\text{r}|^2}{|1 + G^2 \chi_\text{m} \chi_\text{r}|^2} + (n_{b,m} + 1) \frac{\kappa_e \gamma_{m,i} G^2 |\chi_\text{m}|^2 |\chi_\text{r}|^2}{|1 + G^2 \chi_\text{m} \chi_\text{r}|^2} . \end{aligned} \tag{3.28}$$

Here, $n_{b,\text{wg}}$ and $n_{b,r}$ represent the bath of noise photons from the waveguide and the microwave resonator environment respectively; $n_{b,m}$ corresponds to the phonon bath at the mechanical frequency (see Fig. 3.1). We assume thermal input noise correlations for all input noise terms, *i.e.*, $\langle \hat{b}_{b,m}(\omega) \hat{b}^\dagger_{b,m}(\omega') \rangle = (n_{b,m} + 1)\delta(\omega + \omega')$, $\langle \hat{b}^\dagger_{b,m}(\omega) \hat{b}_{b,m}(\omega') \rangle = n_{b,m}\delta(\omega + \omega')$, $\langle \hat{a}_{b,r}(\omega) \hat{a}^\dagger_{b,r}(\omega') \rangle = (n_{b,r} + 1)\delta(\omega + \omega')$, $\langle \hat{a}^\dagger_{b,r}(\omega) \hat{a}_{b,r}(\omega') \rangle = n_{b,r}\delta(\omega + \omega')$, $\langle \hat{a}_{b,\text{wg}}(\omega) \hat{a}^\dagger_{b,\text{wg}}(\omega') \rangle = (n_{b,\text{wg}} + 1)\delta(\omega + \omega')$ and $\langle \hat{a}^\dagger_{b,\text{wg}}(\omega) \hat{a}_{b,\text{wg}}(\omega') \rangle = n_{b,\text{wg}}\delta(\omega + \omega')$.

In the sideband resolved regime and positive detuning (red sideband pump) we can drop the terms proportional to $\widetilde{\chi}_\text{m}$ and $\widetilde{\chi}_\text{r}$. In order to represent a realistic experimental setup, we introduce the fixed gain $\mathcal{G}$ in units of dB and the system noise temperature n_{add} in units of resonator quanta and referenced to the cavity output. We can now write the full expression for the single sided power

spectral density as measured by a spectrum analyzer, valid in the presence of all relevant noise baths

$$S(\omega) = \hbar\omega_d 10^{\mathcal{G}/10}\Big[n_{\text{add}} + n_{b,\text{wg}} + (n_{b,\text{wg}}+1)\Big|\Big(1 - \frac{\kappa_e\chi_\text{r}}{1+G^2\chi_\text{m}\chi_\text{r}}\Big)\Big|^2 + (n_{b,r}+1)\frac{\kappa_e\kappa_i|\chi_\text{r}|^2}{|1+G^2\chi_\text{m}\chi_\text{r}|^2} + (n_{b,m}+1)\frac{\kappa_e\gamma_{m,i}G^2|\chi_\text{m}|^2|\chi_\text{r}|^2}{|1+G^2\chi_\text{m}\chi_\text{r}|^2}\Big]. \quad (3.29)$$

We minimize the number of free parameters by eliminating the resonator bath $n_{b,r}$ using the relation

$$\kappa n_\text{r} = \kappa_e n_{b,\text{wg}} + \kappa_i n_{b,r}. \quad (3.30)$$

With the Eqs. 3.19 and 3.20 we can calculate [71] the mechanical occupation n_m

$$n_m = n_{b,m}\left(\frac{\gamma_{m,i}}{\kappa}\frac{4G^2+\kappa^2}{4G^2+\kappa\gamma_{m,i}}\right) + n_r\left(\frac{4G^2}{4G^2+\kappa\gamma_{m,i}}\right), \quad (3.31)$$

which we use to also replace the mechanical bath occupation $n_{b,m}$ in Eqs. 3.29.

3.4.1 Thermal waveguide noise

Thermal waveguide noise term could originate from a rise of the electronic temperature of the on-chip feedline circuit.

Figure 3.2 a shows a comparison of noise spectra with and without waveguide noise. In the presence of a broad band thermal input field, the background rises and the resonator noise peak shrinks, even though the resonator noise bath is kept constant. The reason is that the cavity filters the broad band input noise, effectively changing the background of the cavity noise peak. If the waveguide noise bath matches the cavity noise bath, no cavity noise peak is observed even though the cavity temperature is increased.

Compared to a model which attributes this background change to a modification of the amplifier noise temperature or an increased attenuation at the output of the detection circuit, *i.e.*, a change of n_{add} only, we extract almost twice the cavity occupation n_r using Eq. 3.29. This also affects the lowest observed mechanical occupation and raises it. Figure 3.2 b shows the extracted noise baths for the dataset measured at 26 mK.

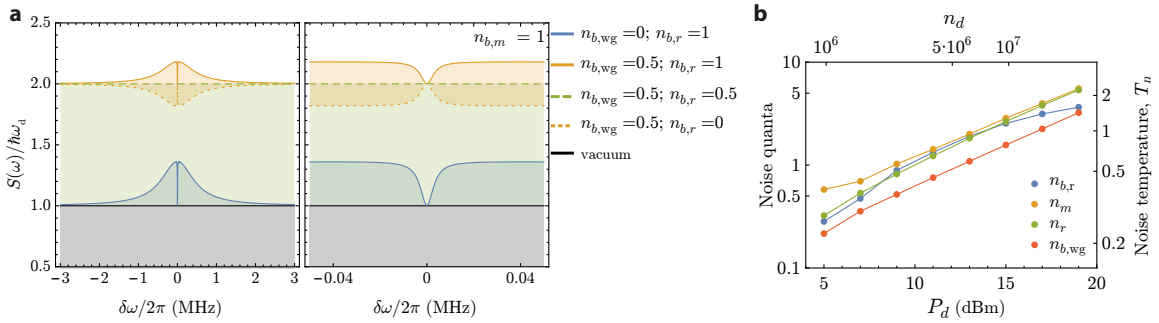

Figure 3.2: **Noise Budget. a,** Shown are solutions to Eq. 3.29 over the resonator bandwidth (left) and the mechanical bandwidth (right). The different curves are plotted for a set of different noise bath parameters, as indicated in the legend. **b,** The fitted noise occupancies n_m, n_r, and $n_{b,\mathrm{wg}}$ are shown together with the resonator bath $n_{b,r}$.

3.4.2 Asymmetric noise spectra

In most electromechanical measurements the cavity noise bath exceeds the waveguide noise bath for all relevant pump powers. In this case the microwave resonator bath n_r manifests itself as a broad band resonator noise peak on top of the background. This power dependent noise peak shows a small asymmetry for the highest pump powers. Such an asymmetry is qualitatively expected from interference between narrow band cavity noise and broad band waveguide noise. We follow a similar procedure as outlined above and introduce a complex waveguide coupling constant to find better agreement with the measured data in this $\kappa_e \rightarrow \kappa_e - iq$ in the first term proportional to $n_{b,\mathrm{wg}}$ in Eq. 3.29 and expand it. For $\kappa_e^2 \gg q^2$ we can only keep q to linear order and simplify the expressions. We can then write the asymmetric noise power spectrum with two additional terms as

$$S_{\mathrm{as}}(\omega) = S(\omega) + \hbar\omega_d 10^{\mathcal{G}/10}(n_{b,\mathrm{wg}}+1)\left[\frac{2qG^2(\omega_m-\omega)|\chi_{\mathrm{m}}|^2|\chi_{\mathrm{r}}|^2}{|1+G^2\chi_{\mathrm{m}}\chi_{\mathrm{r}}|^2} + \frac{2q(\Delta_{r,d}-\omega)|\chi_{\mathrm{r}}|^2}{|1+G^2\chi_{\mathrm{m}}\chi_{\mathrm{r}}|^2}\right]. \quad (3.32)$$

The additional two terms are odd functions with a vanishing integral. This ensures the same fit results as obtained compared to using the symmetric model Eq. 3.29. Defined in this way, the asymmetry scales with the waveguide noise bath and the Fano parameter q, which is independent of any other parameters. We find excellent agreement between this model and the measured broad band noise spectra at high pump powers (see chapter 3). It is important to point out that only the relevant bath occupancies n_m, n_r, and $n_{b,\mathrm{wg}}$ as well as q (in the case of the highest drive powers) are actual fit

parameters, while all other relevant parameters should be extracted from - or verified in - independent (low drive power) measurements.

3.4.3 Relation to the displacement spectrum

In the weak coupling regime we can relate the single sided displacement spectrum $S_{\mathrm{x}}(\omega)$ using

$$\frac{S(\omega)}{\hbar\omega} = \frac{S_{\mathrm{x}}(\omega)}{x_{\mathrm{zpf}}^2}\frac{\kappa_e}{\kappa}\Gamma_+ \tag{3.33}$$

with the photon scattering rate $\Gamma_+ \approx 4G^2/\kappa$ for the optimal detuning $\Delta_{r,d} = \omega_m$, and the factor κ_e/κ taking into account the limited collection efficiency of photons leaving the cavity.

3.5 Low drive power limits

At low drive powers and sufficient shielding from room temperature Johnson noise, it is a very good approximation to set $n_{b,\mathrm{wg}} \to 0$. Eliminating the waveguide noise input allows for a significant simplification of the power spectrum

$$S(\omega) = \hbar\omega_d 10^{\mathcal{G}/10}\Big(1 + n_{\mathrm{add}} + \frac{4\kappa_e(n_r\kappa(\gamma_{m,i}^2 + 4(\omega_m-\omega)^2) + 4n_{b,m}\gamma_{m,i}G^2)}{|4G^2 + (\kappa + 2i(\Delta_{r,d}-\omega))(\gamma_m + 2i(\omega_m-\omega))|^2}\Big), \tag{3.34}$$

with the mechanical noise bath $n_{b,m}$ related to the mechanical occupation n_m in Eq. 3.31. The chosen attenuation and shielding of input and output microwave lines connecting the sample to room temperature Johnson noise limits the expected cavity occupation. (see for example Ref. [73] for an independent temperature measurement in a similar setup). Under these assumptions, which must be verified by low power measurements (constant background noise, no cavity noise peak), we can simplify the power spectrum to the more standard form used in cavity electro- and optomechnics

$$S(\omega) = \hbar\omega_d 10^{\mathcal{G}/10}\Big(1 + n_{\mathrm{add}} + \frac{16n_{b,m}\kappa_e\gamma_{m,i}G^2}{|4G^2 + (\kappa + 2i(\Delta_{r,d}-\omega))(\gamma_m + 2i(\omega_m-\omega))|^2}\Big). \tag{3.35}$$

Without resonator occupation, Eq. 3.31 simplifies to

$$n_m = n_{b,m}\left(\frac{\gamma_{m,i}}{\kappa}\frac{4G^2+\kappa^2}{4G^2+\kappa\gamma_{m,i}}\right) \approx n_{b,m}\Big(\frac{1}{C+1}\Big), \tag{3.36}$$

where we introduced the cooperativity $C = 4G^2/(\kappa\gamma_{m,i})$ and assumed moderate coupling strength $4G^2 \ll \kappa^2$ in the last step.

3.6 Linear response limit - system calibration

For very small drive powers where $C \ll 1$ we can simplify the expected thermal noise spectrum further. Dropping terms associated with backaction allows to measure the displacement noise in a self-calibrated way. This compact model is particularly useful to back out g_0 and the system noise temperature with a minimal number of assumptions.

Starting with Eq. 3.35 we can make the replacement $n_{b,m} \approx n_m$ and drop the backaction term in the denominator. Both is valid for $C \to 0$. We then insert $G = \sqrt{n_d} g_0$ with the drive photon number defined in Eq. 3.5. We furthermore assume that the gain of the system is flat over the relevant detuning such that we can introduce the directly reflected pump power measured at the spectrum analyzer $P_\mathrm{r} = 10^{\mathcal{G}/10} P_\mathrm{out}$. The cavity output power is related to the cavity input power via Eq. 3.4

$$|S_{11}|^2 = \frac{P_\mathrm{out}}{P_\mathrm{in}} = \frac{4\Delta_{r,d}^2 + (\kappa - 2\kappa_e)^2}{4\Delta_{r,d}^2 + \kappa^2}. \tag{3.37}$$

Finally, we can write the measured noise spectrum, normalized by the measured reflected pump tone

$$\frac{S(\omega)}{P_\mathrm{r}} = \mathcal{O} + \frac{64 n_m \kappa_e^2 \gamma_{m,i} g_0^2}{(4\Delta_{r,d}^2 + (\kappa - 2\kappa_e)^2)(\kappa^2 + 4(\Delta_{r,d} - \omega)^2)(\gamma_{m,i}^2 + 4(\omega_m - \omega)^2}. \tag{3.38}$$

Only directly measurable system parameters and the temperature of the mechanical mode need to be known to extract g_0 without any further assumptions about the particular gain, attenuation or noise temperature of the chosen measurement setup. Knowing g_0, it is easy to accurately back out the input attenuation $\mathcal{A} = -66.3$ dB and drive photon number n_d (for example from an EIT measurement). Furthermore, from the measured offset

$$\mathcal{O} = (1 + n_\mathrm{add}) \frac{4\kappa_e}{n_d(4\Delta_{r,d}^2 + (\kappa - 2\kappa_e)^2)} \tag{3.39}$$

we conveniently infer the system noise temperature in units of photons $n_\mathrm{add} \approx 30$. The system gain $\mathcal{G} \approx 46$ dB is then easily determined from the not-normalized wide band background of the

measured noise spectrum $S(\omega)$.

Chapter 4

Electromechanics on Silicon Nitride Nanomembranes

Here in this chapter, we explore Si_3N_4 nanomembranes as a low-loss substrate for integrating superconducting microwave circuits and planar nanomechanical structures. In particular, we exploit the thinness of the nanomembrane to reduce parasitic capacitance and greatly increase the attainable impedance of the microwave circuit. We also use the in-plane stress to engineer the post-release geometry of a patterned membrane [74, 75], resulting in planar capacitors with vacuum gaps down to tens of nanometers. Combining the large capacitance of planar vacuum gap capacitors and the low stray capacitance of compact spiral inductor coils formed on a Si_3N_4 nanomembrane, we show theoretically that it is possible to realize large electromechanical coupling to both in-plane flexural modes and localized phononic bandgap modes of a patterned beam structure.

4.1 Device Design

The key elements of the membrane microwave circuits studied in this chapter are shown schematically in Fig. 4.1(a). The circuits are created through a series of patterning steps of an aluminum-coated 300 nm thick Si_3N_4 nanomembrane, and consist of a mechanical beam resonator, a planar vacuum gap capacitor, a spiral inductor (L), and a 50 Ohm coplanar waveguide feedline. The vacuum gap capacitor, formed across the nanoscale cuts in the membrane defining the beam resonator, is connected in parallel with the coil inductor to create an LC resonator in the microwave C band. Each LC resonator sits within a 777 μm $\times$777 μm square membrane and is surrounded on all sides by a ground plane. The coplanar waveguide feedline is terminated by extending the center conduc-

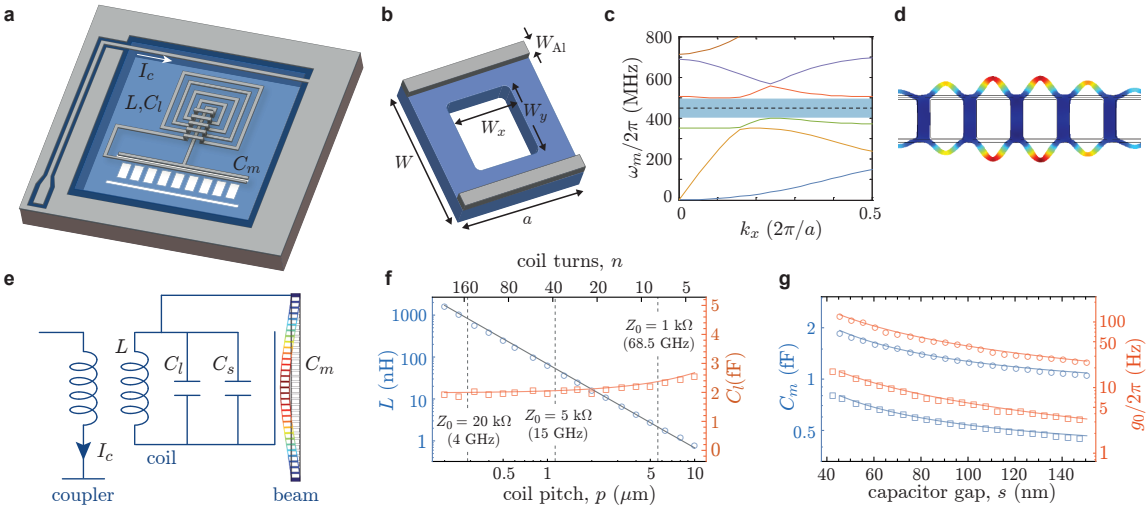

Figure 4.1: **Device design. a,** Schematic of the membrane electromechanical circuit. **b,** Unit cell of the phononic crystal nanobeam. **c,** Acoustic band diagram of the phononic crystal nanobeam with $a = W = 2.23$ μm, $W_x = W_y = 1.52$ μm, and $W_{Al} = 170$ nm. The nitride membrane thickness and aluminum wire thickness are $t_{mem} = 300$ nm and $t_Al = 65$ nm, respectively. The acoustic bandgap is shaded in blue, with the localized breathing mode frequency indicated as a dashed line. **d,** Plot of the FEM-simulated breathing mode profile. Mechanical motion is indicated by an exaggerated displacement of the beam structure and by color, with red (blue) color indicating regions of large (small) amplitude of the motion. **e,** Electrical circuit diagram, where I_c is the current through the reflective coupler, L is the coil inductance, C_l is the coil capacitance, C_s is additional stray capacitance, and C_m is the motional capacitance. The simulated displacement of the in-plane fundamental flexural mode of the beam is shown. **f,** Inductance (L) and capacitance (C_l) of a planar square coil inductor of constant area $A_{coil} = 87$ μm $\times 87$ μm and variable wire-to-wire pitch p. Wire width and thickness are 500 nm and 120 nm, respectively. Method of moments [76] numerically simulated values are shown as open circles (inductance) and open squares (capacitance). Calculations using an analytical model of the planar coil inductor [77] are shown as a solid line. Vertical lines are shown for coils with a characteristic impedance of $Z_o = 1$ kΩ, 5 kΩ, and 20 kΩ, with the coil self resonance frequency indicated in brackets. **g,** FEM simulations of the modulated capacitance C_m (blue symbols) and the electromechanical coupling $g_0/2\pi$ (red symbols) of the in-plane fundamental flexural mode (circles) and the phononic crystal breathing mode (squares) as a function of the capacitor gap size s. Solid curves indicate a $1/s$ fit to the capacitance and coupling data.

tor from one side of the membrane to the other, where it is shorted to the ground plane. Electrical excitation and read-out of the LC resonator is provided by inductive coupling between the center conductor and the spiral inductor. Note that although thinner membranes could have been used, our choice of a 300 nm thick membrane allows for compatibility with single-mode near-IR photonic devices, and is guided by an ultimate goal of integrating planar optical components with electromechanical ones as per Ref. [26].

The electromechanical coupling between the beam resonator and the LC circuit in general depends upon the particular resonant mode of the beam, and is given in terms of the linear dispersion ($g_{\rm EM}$) of the microwave circuit resonance frequency (ω_r) with respect to modal amplitude coordinate u,

$$g_{\rm EM} = \frac{\partial \omega_r}{\partial u} = -\eta \frac{\omega_r}{2C_{\rm m}} \frac{\partial C_{\rm m}}{\partial u}. \tag{4.1}$$

Here C_m is the vacuum gap capacitance across the beam, C_{tot} is the total capacitance of the circuit, and $\eta \equiv C_m/C_{tot}$ is the motional participation ratio. In the case of uniform in-plane beam motion, and assuming C_m behaves approximately as a parallel plate capacitor, the cavity dispersion simplifies to $g_{EM} = \eta\,(\omega_r/2s_0)$, where s_0 is the nominal capacitor gap size. The vacuum coupling rate, describing the interaction between light and mechanics at the quantum level, is given by $g_0 \equiv g_{EM} x_{\rm zpf}$, where $x_{\rm zpf} = (\hbar/2m_{\rm eff}\omega_m)^{1/2}$ is the zero-point amplitude, $m_{\rm eff}$ is the motional mass, and ω_m is the mechanical resonance frequency of a given mechanical mode of the beam.

In this work we consider a patterned beam resonator of width $W = 2.23$ μm and length $l_{beam} = 71.4$ μm which supports two in-plane resonant modes which can be coupled efficiently to microwave or optical cavities [26]. The beam unit cell, shown in Fig. 4.1(b), has a lattice constant a and contains a central hole of width W_x and height W_y. A pair of upper and lower aluminum wires of thickness 65 nm and width 170 nm at the edges of the beam form one half of the vacuum gap capacitor electrodes. Simulations of the mechanical modes of the beam are performed using a finite-element method (FEM) solver [54], and include the internal stress of the nitride film ($\sigma \approx 1$ GPa).

The simulated fundamental in-plane flexural mode of the patterned and wired beam, a displacement plot of which is inserted into the microwave circuit of Fig. 4.1(e), occurs at a frequency of $\omega_m/2\pi = 4.18$ MHz. As shown in Fig. 4.1(c,d), a higher frequency mode also results from Bragg

diffraction of acoustic waves due to the patterning of holes along the beam's length. In the structure studied here the nominal hole parameters are chosen to be $a = 2.23$ μm and $W_x = W_y = 1.52$ μm, which results in a 100 MHz phononic bandgap around a center frequency of 450 MHz. A defect is formed in the phononic lattice by increasing the hole width (W_x) over the central 12 holes of the beam, resulting in a localized "breathing" mode of frequency $\omega_{\rm m}/2\pi = 458$ MHz that is trapped on either end by the phononic bandgap. From the simulated motional mass of both mechanical resonances, the zero-point amplitude is estimated to be $x_{\rm zpf} = 8.1$ fm and 4.2 fm for the flexural and breathing modes, respectively. As motional capacitance scales roughly with mechanical resonator size, realizing large electromechanical coupling to nanomechanical resonators depends crucially on minimizing parasitic capacitance of the microwave circuit as per Eq. (4.1). Utilizing a planar spiral inductor coil of multiple turns greatly increases the coil inductance per unit length through mutual inductance between coil turns, and consequently, reduces coil capacitance. One can determine the capacitance (C_l) and inductance (L) of a given coil geometry by numerically simulating its self resonance frequency with and without a known small shunting capacitance. Figure 4.1(f) displays a method of moments numerical simulation [76] of the self resonance frequency ($\omega_{\rm coil}$) of a series of square planar coil designs with constant area ($A_{coil} = 87$ μm $\times 87$ μm) but varying wire-to-wire pitch p, or equivalently, coil turns n. Here we assume a coil wire width and thickness of 500 nm and 120 nm, respectively, deposited on top of the 300 nm nitride membrane. While the coil capacitance is roughly constant at $C_l \approx 2$ fF, the coil inductance varies over 3 orders of magnitude, in good agreement with an analytical model for planar inductors [77]. An additional stray capacitance of $C_s \approx 2.4$ fF is estimated for the full integrated microwave circuit.

Figure 4.1(g) displays the simulated motional capacitance and vacuum coupling rate versus capacitor slot size s for both the flexural and breathing modes of the beam resonator assuming a coil of pitch $p = 1$ μm ($n = 42$, $L = 68$ nH, $C_l = 2.1$ fF, $\omega_{\rm coil}/2\pi = 13.68$ GHz). Here, $\partial C_{\rm m}/\partial u$ is calculated for each specific mechanical mode utilizing a perturbation theory depending on the integral of the electric field strength at the dielectric and metallic boundaries of the vacuum gap capacitor [78]. For a gap size of $s = 80$ nm, the vacuum coupling rate is estimated to be $g_0/2\pi = 58$ Hz (240 Hz for $\eta = 1$) for the flexural mode and $g_0/2\pi = 8$ Hz (65 Hz for $\eta = 1$) for the breathing mode. Note that here we assume the outer electrode of the vacuum gap capacitor extends along the entire

length of the beam in the case of the flexural mode, whereas for the breathing mode we limit the outer capacitor electrode to the central 6 lattice constants of the beam where the breathing mode has significant amplitude. Also, for the breathing mode simulations the two vacuum gap capacitors are assumed to be connected in parallel, which doubles the vacuum coupling rate due to the mode symmetry.

4.2 Circuit properties

4.2.1 Coil simulation

Our device is fabricated and simulated on a 300 nm thick and $(777\ \mu\text{m})^2$ large Si_3N_4 membrane. The coil wire is 500 nm wide and 120 nm thick, with a 1 μm pitch, 42 turns forming a square with lateral length of only 87 μm, well in the lumped element limit. According to finite element simulations, which include wire cross-overs, the coil is inductive up to its self resonance frequency of $\nu_{\text{srf}} = 13.38$ GHz, where the half wavelength roughly matches the total wire length of $l = 7.7$ mm. We repeat this simulation with a small additional shunt capacitor of known value ($\Delta C = 0.1$ fF) and extract the new self resonance frequency $\nu_{\text{srf,2}}$. Solving the two simple relations $\omega_{\text{srf}} = (LC_{\text{l}})^{-1/2}$ and $\omega_{\text{srf,2}} = (L(C_{\text{l}} + \Delta C))^{-1/2}$, we extract $L = 68$ nH and $C_{\text{l}} = 2.1$ fF. These results are valid close to, but below, the self resonance frequency of the coil. In this limit we realize a maximum impedance of $Z_0 = \sqrt{L/C_{\text{l}}} \approx 5.7$ kΩ, far exceeding the vacuum impedance $Z_{\text{vac}} \approx 377\ \Omega$, and approaching the resistance quantum $R_{\text{q}} = h/(2e)^2 \approx 6$ kΩ.

4.2.2 Full circuit parameters

Knowing the inductance L of the fabricated inductor, as well as the actually measured resonance frequency of $\omega_{\text{r}}/(2\pi) = 7.965$ GHz, yields a total capacitance of $C_{\text{tot}} = C_{\text{l}} + C_{\text{m}} + C_{\text{s}} = 5.87$ fF and a total circuit impedance of $Z_{\text{tot}} = 3.4$ kΩ (see Fig. 7.6). The modulated capacitance C_{m} is a function of the capacitor slot size, which we estimate from SEM images to be on the order of $s \approx 80-100$ nm. Numerical finite element simulations yield a nanobeam capacitance of $C_{\text{m}} \approx 1.4$ fF for this gap size (see Fig. 4.1), which gives a participation factor of $\eta \approx 0.25$.

Using a self resonance frequency simulation of the full electrical circuit including C_{m}, we can

attribute the remaining stray capacitance of $C_s \approx 2.4$ fF to the coil to capacitor wiring (57 %), the presence of a second resonant circuit (14 %), the coupling wire (7 %), and non-ideal crossovers (7 %). The remaining 0.35 fF (15 %) we attribute to frequency dependence, packaging and our uncertainty of the relative permittivity of silicon nitride at low temperature $\epsilon_r \approx 8$. As expected, for these full circuit simulations we extract the same inductance L as for the coil only simulations. The value of $L = 68$ nH is consistent with both, the modified Wheeler and the current sheet method [77], to within ± 2 nH.

4.2.3 High frequency mechanical mode

In order to estimate the electromechanical coupling of the high frequency acoustic mode, we consider that the identical microwave circuit is coupled to both sides of the nanobeam. Here the outer capacitor length is taken to match the acoustic defect region of 2×3 lattice constants. We find a reduced participation ratio $\eta = 0.11$ due to the reduced C_m in this case. Further improvements in reducing the circuit's stray capacitance will have a big impact for efficient coupling to high frequency modes.

4.3 Device Fabrication

4.3.1 Wafer preparation

After a thorough RCA clean we grow a 300 nm thick film of stoichiometric Si_3N_4 at a temperature of 835 C, using low pressure chemical vapor deposition on both sides of a doubly polished 200 μm thick, high resistivity (> 10 kΩ-cm), Si $\langle 100 \rangle$ wafer. After cooldown, the dielectric film has a stress of ≈ 1 GPa due to the differential expansion coefficient. We spin a protective layer of photoresist and dice the wafer in 10 mm $\times$10 mm chips.

4.3.2 Membrane patterning

The chips are cleaned using weak sonication in ACE and IPA and prebaked at 180 °C for 2 min on a hotplate. We then spin the front side with ZEP 520A at 4000 rpm (for protection), bake at 180 °C for 2 min, spin the back side with ZEP 520A at 2000 rpm and bake at 180 °C for 2 min. Patterning

of the 16 membrane areas of size 1 mm $\times$1 mm each is done with 100 keV electron beam exposure with a 200 nA electron beam, 50 nm fracturing size, and a dose of 250 μC/cm^2 on the chip back side. This layer is carefully aligned to the chip corners. We develop with ZND-N50 for 2.5 min and rinse in MIBK for 0.5 min. This is followed by an ICP-RIE etch of the silicon nitride in the developed areas, using a C_4F_8/SF_6 (34/12 sccm) plasma, generated with an ICP power of 1000 W, RF power of 30 W and a DC bias of 84 V, at a pressure of 15 Torr and a temperature of 25 °C for 7 min 15 s. We finish this layer by a thorough cleaning of the chips using weak sonication in TCE, IPA, ZDMAC, ACE, and IPA.

4.3.3 Nanobeam patterning and membrane pre-etching

This layer initially follows the same procedure to pattern the top side of the chip (no resist on the back side) with the nanobeams, pull-in cuts, and the global and pattern alignment markers of size $(20\ \mu\text{m})^2$, with these process parameters: 300 pA beam, 2.5 nm fracturing, 275 μC/cm^2 dose, and 7 min 50 s etch time. We then use an o-ring sealed holder to expose only the back side of the chip to 30 % KOH in water at 85 °C (stir bar at 400 rpm). This anisotropic Si wet etch is stopped when the wafer becomes semi-transparent (dark orange) in the membrane area, when illuminated with an LED on the sealed side of the chip. The color indicates a silicon thickness of $\approx$ 5 μm which is usually achieved after 2.5 h of etching. After cleaning the chip in ultra-pure deionized water and IPA, we wet etch both the front and back side of the chip in 30 % KOH in water at 65 °C (stir bar at 100 rpm) for 70 s. This partially undercuts ($\approx$ 100 nm) the nanobeams for a clean subsequent inverse shadow evaporation process [78], used to pattern the small gapped capacitors. The chips are then rinsed in hot water and fresh piranha solution (mix 45 mL H_2SO_4 with 15 mL H_2O_2 at 85 °C with stir bar at 300 rpm) for 8 min followed by a water and IPA rinse.

4.3.4 Capacitors and ground plane

This layer patterns all of the electrical circuit, except for the coil wires. We start with a prebake at 180 °C for 2 min, and spin the front side with ZEP 520A at 2000 rpm, followed by another bake at 180 °C for 2 min. We use 100 keV electron beam lithography to pattern the ground plane and transmission lines (200 nA beam, 50 nm fracturing, 290 μC/cm^2 dose with PEC), as well as

the capacitor wires, and the wires connecting the capacitors with the coil end and center (10 nA beam, 10 nm fracturing, 275 $\mu C/cm^2$ dose). This layer is carefully aligned to the etched negative markers from the previous step. We develop the chips in the same way and use a O_2 plasma ash process (50 sccm O_2, 0.74 bar, 13.56 MHz, 35 W, 2 min) to descum the surface before deposition of aluminum. For the deposition we use an electron beam evaporator (0.3 nm/s, 65 nm thickness at $1 \cdot 10^{-7}$ mbar to $2 \cdot 10^{-7}$ mbar). We then do a lift-off process in 80 °C NMP for $>$ 1 h and carefully rinse in ACE and IPA.

4.3.5 Scaffolding layer

Now we pattern a scaffolding layer to fabricate the cross-overs. After prebaking, we spin LOR 5B at 3000 rpm and bake at 180 °C for 5 min, followed by spinning PMMA 950k A2 at 4000 rpm and baking at 180 °C for 5 min. We then beam write the negative pattern of the cross-over support structure using aligned electron beam lithography (200 nA beam, 25 nm fracturing, 1000 $\mu C/cm^2$ dose). The resist is developed using MIBK:IPA (1:3) for 1 min, and rinsed in IPA for 30 s. We then wet etch the scaffolding layer using MF-319 for 8 s, followed by a water rinse and IPA which stops the etch. Finally we remove the remaining PMMA layer with ACE (30 s) and reflow the LOR cross-over support layer on a hot plate at 200 °C for 10 min. This creates a structurally stable arc shaped cross over scaffolding.

4.3.6 Coil wire patterning

In order to pattern the narrow pitch coils, we spin PMMA 495 A8 at 2000 rpm, bake, spin PMMA 950k A2 at 2000 rpm and bake again. Then we lithographically define the coil wires, which overlap the capacitor wires (10 nA beam, 10 nm fracturing, 1800 $\mu C/cm^2$ dose) and develop the resist as described previously. Development is followed by the same plasma ashing, deposition of aluminum (1 nm/s, 120 nm, p$\approx 2 \cdot 10^{-7}$ mbar), and lift off, during which the NMP (at 80 °C, 3 h) dissolves the LOR scaffolding layer.

4.3.7 DC contact wire

After a careful rinse with ACE and IPA we reproduce the previous layer recipe to pattern a small (500 nm$\times$4 μm) DC contact wire that symmetrically covers all overlap regions between capacitor wire and coil wire (two per coil and capacitor). Here we use an in-situ ion gun etch process (normal incidence with 4 cm gridded Kaufman source, 400 V, 21 mA for 5 min) right before the aluminum deposition of thickness 140 nm, in order to establish reliable contact. Contact is tested after lift-off on DC test structures of the same contact size located in the center of the chip. High resistance contacts with low capacitance at microwave frequencies would lead to additional parasitic in-series capacitances of the fabricated circuit.

4.3.8 Release

For the final release step we prepare a silicon enriched solution of TMAH to selectively etch the silicon without aluminum corrosion [79, 80]. We use a custom built reactor vessel with thermometer port and a hotplate with magnetic stir bar to mix 60 g of TMAH (25 %, 6N) and 250 g water, and then add 5.12 g of silicon powder (-325 mesh, 5N) and stir at 300 rpm. After the chemical reaction calms down we start heating the solution up to 80 °C. When the solution is clear, we wait for 1 h and prepare a clear mixture of 5.21 g of TMAH (25 %, 6N) and 2.11 g of the oxidizing agent ammonium persulfate in a small beaker. We add the mixture to the solution (stir bar at 1000 rpm), wait 10 min to 15 min, reduce the stir speed and add the sample in a vertical position. The sample is securely clamped, but with the membranes open to a steady flow of solution on the back and front side of the chip. We keep the solution at 80 °C and wait for the membranes to become fully transparent (1 h to 2 h). As a last step we carefully remove the sample, rinse it throughly in hot water, cold water, IPA, ultra purified IPA, and dry it using a CO_2 critical point dryer.

4.4 Coherent electromechanical response

Sweeping a narrowband microwave source across the 6 GHz-12 GHz frequency range, and measuring in reflection, we find a high-Q, strongly coupled microwave resonance at $\omega_r/2\pi = 7.965$ GHz corresponding to the larger coil of 42 turns. This is very close to the expected LC resonance fre-

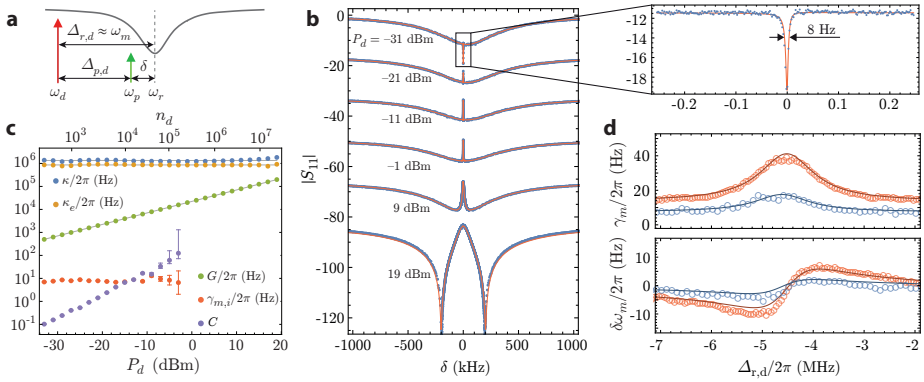

Figure 4.2: **Coherent response. a,** Schematic of the two-tone EIT spectroscopy measurement. **b,** Measured (blue points) probe spectra for different drive powers, all with a fixed drive detuning of $\Delta_{r,d} \approx \omega_m = 4.815$ MHz. Each spectrum is offset by -16.5 dB for better visibility. Fits to measured spectra using Eq. (3.24) are shown as solid red curves. Inset shows a zoomed-in view of the lowest power measurement with a mechanical linewidth of $\gamma_m/2\pi = 8$ Hz. **c,** Extracted system parameters (symbols) as a function of drive power using Eq. (3.24) to fit the measured spectra. Error bars correspond to a 95 % confidence interval in the fit to the measured spectra. **d,** Mechanical linewidth γ_m (top) and the mechanical frequency shift $\delta\omega_m$ due to the optical spring effect (bottom) versus drive detuning $\Delta_{r,d}$ at a fixed intra-cavity drive photon number. Shown are the fit values from the measured probe spectra for two different fridge temperatures, $T_f = 11$ mK (blue circles) and $T_f = 114$ mK (red circles). The drive photon number at $T_f = 11$ mK ($T_f = 114$ mK) is equal to $n_d = 2350$ (5980). The solid line curves are a fit to the damping and spring shift using a radiation pressure back-action model as per Ref. [81].

quency based upon the above simulations, indicating that the stray and motional capacitance of the circuit are close to the expected values. Using a two-tone pump and probe scheme we are able to study the coherent interaction between the microwave electrical circuit and the coupled nanobeam mechanical resonator. In the driven linearized limit [82], the circuit electromechanical system is approximately described by an interaction Hamiltonian $H_{\rm OM} = \hbar G(\hat{a}^\dagger \hat{b} + \hat{a}\hat{b}^\dagger)$, where $\hat{a}$ ($\hat{a}^\dagger$) is the microwave photon annihilation (creation) operator for the LC resonator mode of the circuit and $\hat{b}$ ($\hat{b}^\dagger$) are the phonon annihilation (creation) operators of the mechanical resonance. $G = g_0\sqrt{n_d}$ is the parametrically enhanced electromechanical coupling strength, with n_d corresponding to the number of intra-cavity microwave drive photons inside the resonator. As schematically indicated in Fig. 4.2, pumping with a strong drive at a detuning $\Delta_{r,d} \equiv \omega_r - \omega_d \approx \omega_m$ from the LC resonance of the circuit produces a two-photon resonance condition with a second (weaker) probe tone as it is swept across the microwave resonance. Interference in the reflected probe signal occurs between that part of the probe field which enters the microwave resonator and is directly re-emitted, and that

part of the probe field which enters the cavity, interacts with the mechanical resonator, and is then re-emitted from the cavity. Probing this interference as a function of the probe detuning δ yields the optomechanical analog of electromagnetically induced transparency (EIT) [83, 84].

For red-sideband pumping ($\Delta_{r,d} \approx \omega_m$) the expected probe reflection spectrum is given by Eq.3.24. In this work we focus on the fundamental in-plane flexural mode of the beam. The phononic crystal breathing mode at a frequency of 450 MHz is not accessible in our current single microwave resonator circuit given the high drive power required to excite the circuit at the large cavity detuning required for two-photon resonance. In future work a double resonant system [85] may be employed to overcome this limitation and allow for efficient excitation and detection of high frequency mechanical resonators such as the breathing mode. By stepping the pump detuning frequency ($\Delta_{r,d}$) and sweeping the probe signal across the cavity resonance, an EIT-like transparency window in the microwave cavity response is found at a drive detuning of 4.4815 MHz, close to the theoretically simulated resonance frequency (4.18 MHz) of the fundamental in-plane flexural mode. Figure 4.2(b) shows a series of measured probe spectra (blue points) at different applied drive powers for a drive detuning fixed close to the two-photon resonant condition of $\Delta_{r,d}/2\pi \approx \omega_m = 4.48$ MHz. Fits to the measured spectra are performed using Eq. (3.24) and plotted as solid red curves in Fig. 4.2(b). From each fit we extract the loaded microwave resonator properties (κ, κ_e, ω_r), the parametric coupling rate (G), the mechanical frequency (ω_m), and the intrinsic mechanical damping rate ($\gamma_{m,i}$). These fit values are plotted versus drive power in Fig. 4.2(c). The microwave cavity parameters ($\kappa/2\pi \approx 1.28$ MHz, $\kappa_e/2\pi \approx 0.896$ MHz) are found to be approximately constant over 5 orders of magnitude in drive power, up to an intra-cavity photon number of $n_d \approx 2 \times 10^6$. For $n_d \gtrsim 2 \times 10^6$ the intrinsic damping of the cavity begins to rise, and above $n_d \approx 4 \times 10^7$ ($P_d = 19$ dBm) the LC circuit goes normal. Conversion from drive power to intra-cavity photon number n_d is performed using the thermometry calibrations described in the next section. At low drive power ($C \lesssim 100$) the fits yield high confidence estimates of both C and $\gamma_{m,i}$, with the intrinsic mechanical damping of the resonator estimated to be $\gamma_{m,i}/2\pi = 8$ Hz at the lowest drive powers (see inset to Fig. 4.2(b)). At high drive powers ($C \gtrsim 100$) the transparency window saturates and becomes too broad to accurately determine either C or $\gamma_{m,i}$. As such we only provide fit estimates for C and $\gamma_{m,i}$ below a cooperativity of 100. Figure 4.2(d) shows a plot of the measured mechanical frequency shift ($\delta\omega_m$)

and damping ($\gamma_m \equiv \gamma_{m,i} + \gamma_{\rm EM}$) versus drive detuning $\Delta_{r,d}$. Here we adjust the drive power as a function of drive detuning so as to maintain a constant intra-cavity drive photon number, and fit the transparency window using a Fano lineshape (see SI). Data was taken at $T_f = 11$ mK as well as at an elevated fridge temperature of $T_f = 114$ mK. The intra-cavity drive photon number in both cases was chosen to yield a peak cooperativity of order unity. We observe broadening of the mechanical linewidth that peaks at a detuning $\Delta_{r,d}$ equal to the mechanical resonance frequency, and stiffening (softening) of the mechanical mode for drive detuning above (below) the mechanical resonance frequency. Plots of the theoretical damping and frequency shift due to radiation pressure backaction [81] are shown as solid back curves in Fig. 4.2(d). We find a parametric coupling rate $G/2\pi = 1.80$ kHz (2.98 kHz) and intrinsic mechanical damping rate $\gamma_{m,i}/2\pi = 7.7$ Hz (14 Hz) that fit both the damping and spring shift curves at $T_f = 11$ mK (114 mK), in close agreement with the estimated values from the fixed detuning data in Fig. 4.2(b).

4.5 Mode thermometry and backaction cooling

Measurement of the mechanical resonator noise is used to calibrate the delivered microwave power to the circuit and study the backaction cooling of the mechanical resonator. In the resolved sideband limit ($\omega_m/\kappa \gg 1$), efficient scattering of drive photons by mechanical motion occurs for $\Delta_{r,d} = \pm\omega_m$, in which either anti-Stokes ($\Delta_{r,d} = \omega_m$) or Stokes ($\Delta_{r,d} = -\omega_m$) scattering is resonant with the cavity. Blue detuned pumping at $\Delta_{r,d} = -\omega_m$ results in Stokes scattering of the drive field, down-converting a photon to the cavity resonance and emitting a phonon into the mechanical resonator in the process. Red detuned pumping at $\Delta_{r,d} = \omega_m$, as illustrated in Fig. 4.3(a), leads to predominantly anti-Stokes scattering in which a drive photon is up-converted to the cavity resonance and a phonon is absorbed from the mechanical resonator. The per-phonon anti-Stokes scattering rate for this pumping geometry is $\Gamma_{\rm AS} \approx 4G^2/\kappa$, to a good approximation equal to the backaction damping rate $\gamma_{\rm EM}$ which leads to cooling of the mechanical resonator [70].

Figure 4.3(b) shows a plot of the measured area underneath the Lorentzian noise peak of the fundamental in-plane mechanical resonance versus fridge temperature. Here, data for blue detuned ($\Delta_{r,d} = -\omega_m$) driving has been averaged over several different temperature sweeps, with the area at each temperature normalized to units of phonon occupancy ($n_{b,m}$) using the high temperature

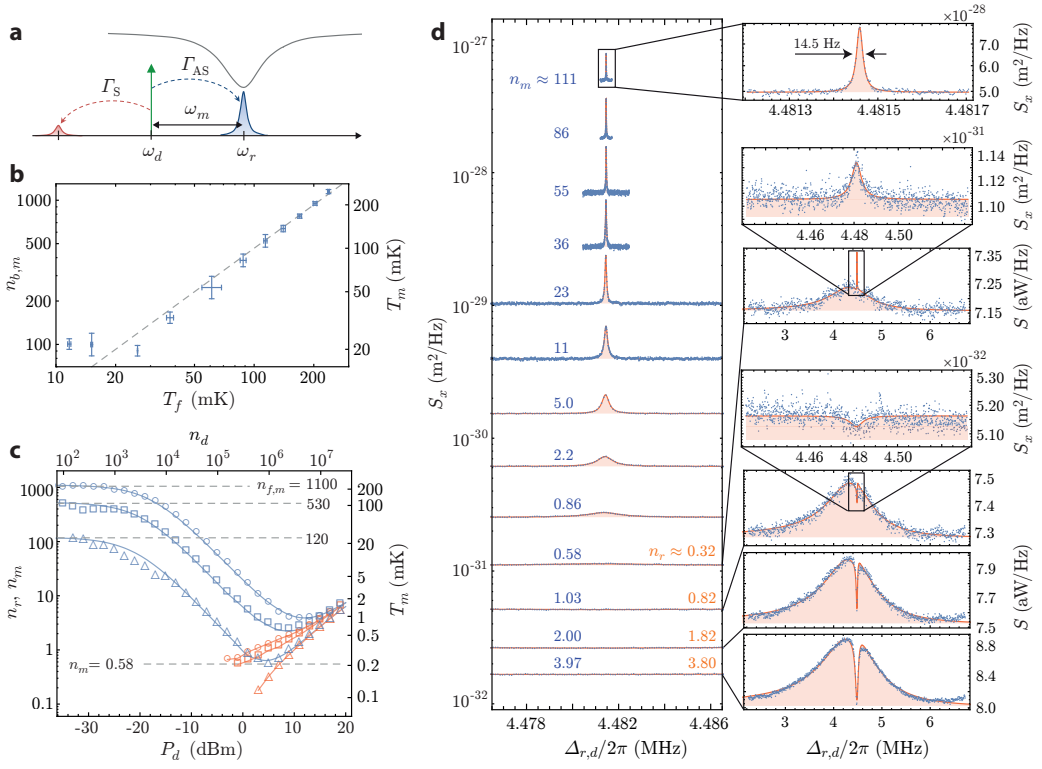

Figure 4.3: **Mechanical displacement noise a,** Schematic showing the pump detuning and scattered microwave signals used to measure the mechanical resonator's displacement noise. **b,** Plot of the measured mechanical resonator bath phonon occupation ($n_{b,m}$) and effective temperature (T_m) as a function of the fridge temperature (T_f). Each data point corresponds to the average inferred occupancy for blue detuned driving ($\Delta_{r,d} = -\omega_m$) at low cooperativity ($C \ll 1$). Error bars corresponding to the standard deviation in the inferred occupancy over several temperature sweeps. Calibration in units of occupancy is performed using a fit to Eq. (4.2) as described in chapter. 3. The gray dashed lines show the expected Bose-Einstein distribution ($n_m = (\exp(\frac{\hbar\omega_m}{k_B T_f}) - 1)^{-1}$) assuming perfect thermalization to the fridge. **c,** Plot of the dynamic backaction cooling of the mechanical resonator versus drive power at three different fridge temperature: $T_f = 235$ mK ($n_{f,m} = 1100$; open circles), $T_f = 114$ mK ($n_{f,m} = 530$; open squares), and $T_f = 26$ mK ($n_{f,m} = 120$; open triangles). Data points showing the estimated average phonon occupancy of the fundamental in-plane flexural mode at $\omega_m/2\pi \approx 4.48$ MHz (n_m) are shown as blue symbols, whereas data points for the estimated microwave cavity photon occupancy at $\omega_r/2\pi = 7.498$ GHz (n_r) are shown as orange symbols. The corresponding effective mode temperature, T_m, of the flexural mechanical mode is also shown on the right vertical axis. The solid line blue curves correspond to a model for the expected mechanical mode occupancy using the a fit to the measured drive power relation for G and the microwave cavity parameters from coherent two-tone spectroscopy, the intrinsic mechanical damping from low power thermometry measurements, and a fit to the power dependence of the microwave resonator occupancy. **d,** Measured anti-Stokes noise displacement spectrum for several different drive powers at $T_f = 26$ mK (blue data points). Fits to the measured spectra are shown as red solid lines. Extracted values for n_m and n_r are indicated and correspond to the results presented in panel (c). Zoom-ins of the cavity noise and measured noise peaks are shown as insets.

measurement ($T_f = 235$ mK) as a reference point. In these measurements the drive power was kept at a low enough value to ensure $C \ll 1$ and negligible backaction damping or amplification. The mechanical flexural mode is seen to thermalize with the fridge temperature all the way down to $T_f \approx 25$ mK, at which point the mechanical mode temperature saturates. The source of this temperature saturation in the mechanics is not fully understood, but is thought to be due to coupling to two-level systems (TLS) in the amorphous Si_3N_4 membrane [86]. These TLS can be driven by the microwave input signal into an elevated temperature state, and, as presented in the SI, can also strongly couple with the high impedance microwave cavity resonance. This latter property may interfere with the mechanical transduction process, leading to unreliable thermometry of the mechanical mode.

For a known temperature of the mechanical resonator, one may also employ the above low-cooperativity thermometry measurement to calibrate the vacuum coupling rate g_0 between the mechanics and the microwave circuit [87]. As the reflected drive signal and the scattered photons by the mechanical mode experience the same amount of gain, normalizing the measured reflected noise spectrum ($S(\omega)$) by the measured reflected drive tone amplitude (P_{refl}) yields a Lorentzian of the following form for a drive detuning of $\Delta_{r,d} = \omega_m$,(see Chapter 2):

$$\frac{S(\omega)}{P_{refl}} \approx \mathcal{O} + \frac{16 g_0^2 \kappa_e^2}{\left((\kappa - 2\kappa_e)^2 + 4\omega_m^2\right)\left(\kappa^2 + 4(\omega_m - \omega)^2\right)} \times \frac{4 n_{b,m} \gamma_{m,i}}{\gamma_{m,i}^2 + 4(\omega - \omega_m)^2}. \tag{4.2}$$

The background offset $\mathcal{O}$ yields the added noise of the measurement amplifier chain; $n_{\text{add}} \approx 30$ for our current set-up. Integrating the normalized spectral density for the reference fridge temperature of $T_f = 235$ mK ($n_{f,m} = 1100$), and assuming $n_{b,m} = n_{f,m}$, yields a vacuum coupling rate of $g_0/(2\pi) = 41.5$ Hz, comparable to that estimated from numerical simulation (58 Hz for $s = 80$ nm). With g_0 calibrated, the conversion factor between drive power and intra-cavity drive photon number can now be determined from the coherent two-tone spectroscopy measurements of $G = g_0\sqrt{n_d}$, as displayed in Fig. 4.2(c).

Increasing the drive power to large cooperativity levels results in backaction cooling of the mechanical resonator for detuning $\Delta_{r,d} = \omega_m$. Figure 4.3(c) plots the measured occupancy of the mechanical resonator versus drive power for three different fridge temperatures, $T_f = 235$, 114, and 26 mK. For the lowest of these temperatures ($T_f = 26$ mK), the measured noise power spec-

tral density from low to high drive power is shown in Fig. 4.3(d). At low drive powers we find excellent agreement between the inferred n_m and the bath occupancy corresponding to the fridge temperature, $n_{f,m}$, for all three temperatures. At intermediate drive powers the mechanical mode is both damped and cooled according to $n_m = n_{f,m}/(C+1)$. At the highest drive powers we measure both an increase in broadband added noise and Lorentzian microwave cavity noise. We attribute this excess noise to absorption of the input microwave drive. These two additional noise inputs can lead to noise squashing in the measured output spectrum and heating of the mechanical resonator [71, 84, 88, 89]. Using a model that includes microwave (thermal) noise in the input line ($n_{b,\mathrm{wg}}$) and in the microwave cavity ($n_{b,r}$) we fit the measured spectra at higher drive power for the mechanical mode occupancy n_m (blue symbols) and the microwave cavity noise occupancy n_r (orange symbols). The lowest mechanical occupancy is found to be $n_m = 0.58$ for a drive photon number of $n_d = 10^6$ and a fridge temperature of $T_f = 26$ mK, and is similar to the lowest occupancies realized to date for other backaction cooled electromechanical resonators [84, 90, 91]. Measurements at the lowest fridge temperature of $T_f = 11$ mK resulted in inconsistent and fluctuating cooling curves, attributable we believe to drive-power-dependent coupling of individual TLS to the microwave cavity.

4.6 Vacuum Rabi splitting and ac Stark tuning of a nanoscopic two-level system

The demonstrated motional sideband cooling is facilitated by the small capacitor gap size, the high impedance, and small stray capacitance of the electrical circuit. These are very desirable properties in the context of quantum electrodynamics (QED), e.g. with atomic systems. The vacuum fluctuations of the tested resonator give rise to a large root mean square voltage of $V_{\mathrm{vac}} = \sqrt{\hbar\omega_r/(2C_{\mathrm{tot}})} = \omega_r\sqrt{\hbar Z_{\mathrm{tot}}/2} \approx 21\ \mu$V. With a gap size of only $s \approx 80$ nm, the electric field across the capacitor C_{m} is as large as $E_{\mathrm{vac}} \approx 260$ V/m, about 10^3 times larger than in typical coplanar waveguide resonators and $> 10^5$ times that of typical small 3D microwave cavities of similar frequency. For the largest pump photon numbers $n_d \approx 4 \cdot 10^7$ we apply an rms voltage of $V_{\mathrm{max}} \approx 1.7$ kV, corresponding to a maximum field strength of $E_{\mathrm{max}} \approx 21$ GV/m. To our knowledge this is a record high value for a low loss superconducting microwave resonator.

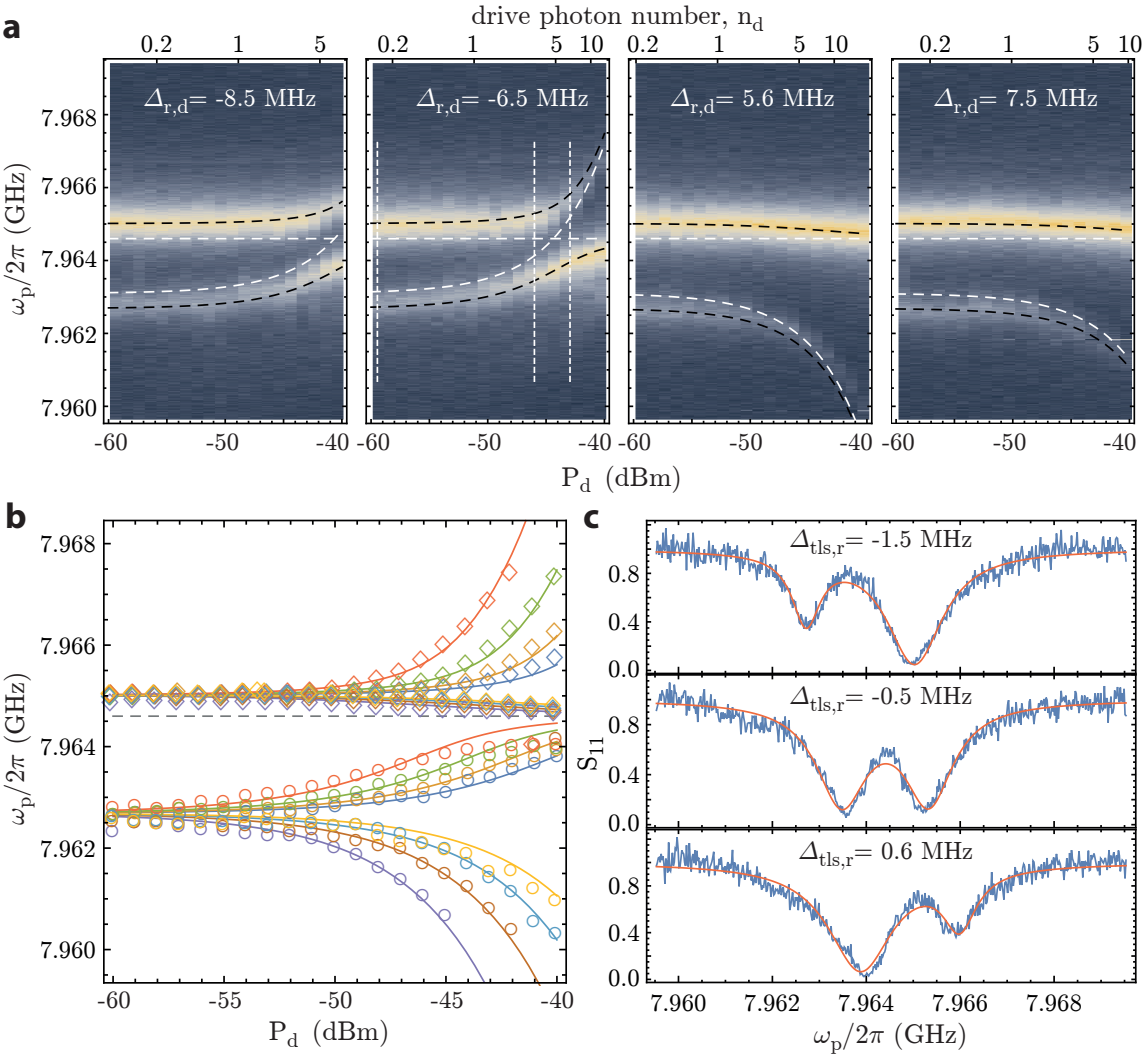

Figure 4.4: **a,** Color plot of the measured reflection S_{11} (blue is high, yellow is low) of a weak coherent probe tone ω_p as a function of the drive power P_d for 4 different drive detunings $\Delta_{r,d}$. Dashed lines show uncoupled (white) and coupled TLS-resonator eigenvalues. **b,** Measured eigenfrequencies extracted from a double Lorentzian fit (circles), theory (solid lines) and the bare resonator frequency (dashed line) for different negative $\Delta_{r,d} = (-8.5, -7.5, -6.5, -5.5)$ MHz and positive $\Delta_{r,d} = (4.5, 5.5, 6.5, 7.5)$ MHz drive detunings. **c,** Measured spectrum (blue) and double Lorentzian fit (red) for $\Delta_{r,d} = -6.5$ MHz and three different drive powers; see vertical dotted lines in panel a.

Large vacuum fields enable efficient dipole coupling $g_{0,\mathrm{tls}} = \vec{E} \cdot \vec{d}$ to microscopic systems with small dipole moments $\vec{d}$, such as molecular two level systems (TLS) [86], single atoms, or charge quantum dots. We demonstrate this by observing coherent coupling between the resonator vacuum field and a nanoscopic TLS on the substrate (see Fig. 4.4). The demonstrated ac-Stark control of this

nanoscopic system complements previous strain based control techniques [92], and will be useful to suppress the negative impact of TLS in engineered solid state quantum systems. The quantum nonlinearity of the TLS furthermore represents a unique calibration tool, which is generally missing in electro- and opto-mechanical systems. More importantly, it could point the way to how to better understand the origin and location of TLS, which are believed to be the limiting factor not only for ground state cooling of electromechanical systems but more generally for improving the integration density of low loss superconducting circuits.

In order to observe vacuum Rabi mode splitting, we reduce the probe power significantly such that the probe photon number $n_p \ll 1$. In order to control the interaction, we use a second off-resonant drive tone at frequency ω_d to Stark-shift the TLS into and out of resonance with the resonator. For sufficient detuning $\Delta_{\text{tls},d} \equiv \omega_{\text{tls}} - \omega_d$ we can adiabatically eliminate direct transitions of the TLS [93] and define the new Stark-shifted TLS frequency as

$$\tilde{\omega}_{\text{tls}} \approx \omega_{\text{tls}} + \frac{\Omega_R^2}{2\Delta_{\text{tls},d}}, \tag{4.3}$$

with $\Omega_R = 2g_{0,\text{tls}}\sqrt{n_d}$ the Rabi frequency due to the off-resonant drive tone.

Using this linearized model we find very good agreement for different drive detunings $\Delta_{r,d} \equiv \omega_r - \omega_d$ and drive strength in the range $|\Omega_R/(2\Delta_{\text{tls},d})| < 1$ for which the linearization is valid, see Fig. 4.4. The attenuation $\mathcal{A} = -66.8$ dB, entering via the drive photon number n_d, is the only fit parameter and agrees with our previous calibration to within 0.5 dB. The presented Stark-shift measurements therefore independently confirm the previously calibrated drive photon numbers and the electromechanical coupling g_0. Similar Stark-shift calibrations are quite common in superconducting qubit experiments [94]. Opto- and electromechanics experiments on the other hand typically lack the necessary strong vacuum nonlinearities for an absolute calibration with the vacuum field.

It is now clear that the presence of a coupled TLS can strongly modify the resonator lineshape. This could explain why at low drive powers, where the TLS happens to be close to the resonator frequency, the electromechanical transduction efficiency is reduced and the mechanical occupancy appears to be lower than expected (see Fig. 4.3 (c)). Although the studied TLS should be far detuned in the relevant power range, there may be other weakly coupled TLS which do not Stark tune as easily, but still absorb and scatter photons at a high rate. At high drive powers on the other hand, all

TLS are either saturated due to the high intra-cavity photon numbers, or far detuned from the drive and resonator frequencies.

On resonance, the vacuum Rabi split linewidths are approximately given by an equal mixture of resonator and TLS linewidth, which we use to estimate $\gamma_{\text{tls}}/(2\pi) = 1.3$ MHz. We extract a TLS coupling of $g_{0,\text{tls}}/(2\pi) = 0.9$ MHz from the minimum separation of the measured spectroscopic lines (see Fig. 4.4 c). This puts our system very close to the strong coupling limit $g_{0,\text{tls}} \geq (\kappa, \gamma_{\text{tls}})$. We can also put a lower bound on the electric dipole moment of this TLS $|d| \geq 0.7$ Debye depending on the TLS orientation and the exact position on the capacitor.

This value is comparable to many atomic, nano- and microscopic systems, where strong coupling is not readily observed. The presented techniques therefore open up new possibilities to realize hybrid systems and can help study the loss mechanism that plagues superconducting quantum processors more directly, selectively, and with higher sensitivity.

Chapter 5

Electromechanics on Silicon-On-Insulator

5.1 Introduction

In this chapter, we develop a new fabrication process for the creation of high-Q microwave superconducting aluminum (Al) resonators on thin-film silicon membranes suitable for integration with mechanical and photonic devices. Compared to the silicon nitride Si_3N_4 nanomembrane, the higher dielectric index of silicon membrane makes them more suitable for photonics application within the communication wavelength band. Simultaneously, the platform is compatible with superconducting qubit. Moreover, the silicon has a crystalline structure and is known to have less defects compared to amorphic structure of Si_3N_4 membrane, allowing for fabrication of higher quality microwave and mechanical cavities. As a proof of concept, we demonstrate parametric radiation pressure coupling of an 8.9 GHz microwave superconducting resonator to the motion of a 9.7 MHz silicon micromechanical resonator. The electromechanical circuit, shown schematically in Fig. 5.1(a), consists of a high-impedance microwave coil resonator capacitively coupled to the fundamental in-plane differential mode of a pair of patterned silicon slabs. Although not a feature exploited in the present study, the patterned slabs also form a slotted photonic crystal cavity which supports an optical resonance in the 1500 nm telecom wavelength band [78, 95, 96]. In principle, this mechanical resonator (what we hereafter refer to as the "H-slot" resonator) could simultaneously couple to optical photons in the photonic crystal cavity and microwave photons in the superconducting microwave resonator. We present the preliminary results measured from "H-slot" resonator and the fabrication process is discussed.

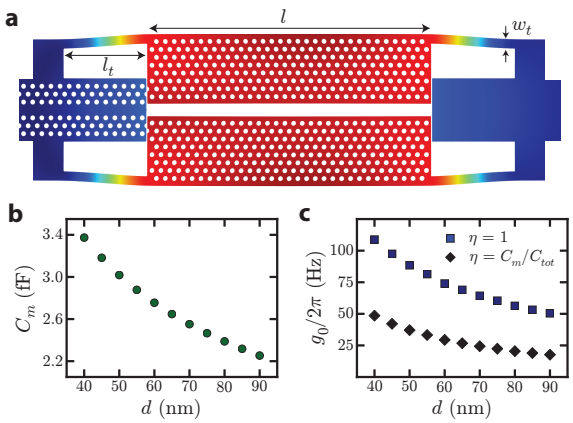

Figure 5.1: **a**, FEM simulation of the differential mechanical mode. In this work, $l = 13.5$ μm, $w_t = 440$ nm, and $l_t = 4$ μm. These values give a simulated mechanical mode frequency of $\omega_m/2\pi = 9.76$ MHz. **b**, Plot of FEM simulation values of C_m versus slot size d. **c**, Plot of FEM simulation values of g_0 versus slot size d for: (i) $C_s = C_l = 0$ fF corresponding to an ideal $\eta = 1$ (blue squares) and (ii) $C_l = 3.05$ fF and $C_s = 1.13$ fF from FEM simulations of the circuit (black diamonds). For these plots, the resonance frequency is fixed at the measured frequency of $\omega_r/2\pi = 8.872$ GHz. At the estimated capacitor gap of $d \approx 60$ nm from SEM images, the theoretical values of the motional capacitance and the vacuum coupling rate are $C_m = 2.76$ fF and $g_0/2\pi = 29.3$ Hz, respectively.

5.2 Design

The H-slot mechanical resonator is depicted in Fig. 5.1(a), where finite-element method (FEM) numerical simulations [54] are used to solve for the fundamental in-plane mechanical motion of the structure. The resonator is formed from a Si layer of 300 nm thickness, and consists of two patterned slabs that are separated by a central nanoscale slot and tethered on each end to a central clamp point. As mentioned, the hole patterning in the two slabs produces a localized photonic crystal cavity. The hole patterning on the left side of the H-slot resonator forms a photonic crystal optical waveguide which can be used to efficiently excite the optical cavity. Aluminum electrodes are fed into the H-slot resonator from the right side of the structure, and span the outer edges of the two slabs forming one half of a vacuum gap capacitor [labeled C_m in Fig. 5.1(a)]. The length ($l = 13.5$ μm) of the photonic crystal slabs is chosen long enough to support a high-Q optical mode and to realize a motional capacitance on the scale of a few femtoFarad. The width (w) of the photonic crystal slabs is chosen to accommodate a number of photonic crystal periods that should (again) provide high optical Q, but otherwise is minimized to limit the motional mass of the resonator. The slab photonic

crystals are supported by tethers whose length ($l_t = 4$ μm) and width ($w_t = 440$ nm) produce a simulated mechanical frequency of $\omega_m/2\pi \approx 9.76$ MHz for the fundamental in-plane differential mode, compatible with resolved-sideband pumping through the coupled microwave circuit.

The simulated effective mass and zero-point amplitude of the differential mode are $m_{\text{eff}} = 42.9$ pg and $x_{\text{zpf}} = 4.5$ fm, respectively. These figures include the aluminum wires (width $= 250$ nm, thickness $= 60$ nm) that form the vacuum gap capacitor. By using a tuning fork design in which the upper and lower slabs are coupled together at each end through the central tether clamp points, acoustic radiation out the ends of H-slot resonator can be greatly reduced. Optimization of the tether clamp point geometry yields a numerically simulated mechanical quality factors as high as $Q_m = 3.7 \times 10^7$. As shown in Chapter 3, the vacuum electromechanical coupling rate of the H-slot mechanical resonator to the microwave coil resonator is given by

$$g_0 = x_{\text{zpf}} \frac{\partial \omega_r}{\partial u} = -\eta x_{\text{zpf}} \frac{\omega_r}{2C_m} \frac{\partial C_m}{\partial u}, \tag{5.1}$$

where u is the generalized amplitude coordinate of the fundamental in-plane differential mode of interest, $x_{\text{zpf}} = \sqrt{\hbar/(2\omega_m m_{\text{eff}})}$ is the zero-point amplitude of the mechanical resonance, $\eta = C_m/C_{tot}$ is the participation ratio of the motional capacitance (C_m) to the total capacitance of the circuit ($C_{tot} = C_m + C_l + C_s$). In addition to the motional capacitance, the total circuit capacitance consists of the intrinsic self-capacitance of the inductor coil (C_l) and any additional stray capacitance of the circuit (C_s). This ratio — and hence the electromechanical coupling — is maximized for small $C_s + C_l$ and large C_m. We achieve a relatively small value of coil capacitance by using a tightly wound rectangular spiral inductor [22, 77] with wire width of 550 nm and wire-to-wire pitch of 1 μm. A simulation of the entire circuit layout, including nearby ground-plane, coupling wire, and connecting wires between the coil and the motional capacitor yields an additional stray capacitance of $C_s = 1.13$ fF. For a coil of 34 turns, with an estimated inductance of $L = 46.3$ nH and capacitance $C_l = 3.05$ fF, connected in parallel to a motional capacitance of $C_m = 2.76$ fF corresponding to a vacuum gap of $d = 60$ nm, the microwave resonance frequency of the coupled circuit is estimated to be $\omega_r/2\pi = 8.88$ GHz. Using these circuit parameters in conjunction with a perturbative calculation [78,97] of $(1/C_m)\partial C_m/\partial u$ based upon FEM simulations of the differential mechanical mode and the electric field distribution in the vacuum gap capacitor yields a calculated

vacuum electromechanical coupling strength of $g_0/2\pi = 29.3$ Hz. The trend of both C_m and g_0 with gap size d is shown in Fig. 5.1(c).

The devices studied in this work are fabricated from 1 cm $\times$ 1 cm chips diced from a high-resistivity silicon-on-insulator (SOI) wafer manufactured by SOITEC using the Smart Cut process [98]. The SOI wafer consists of a 300 nm thick silicon device layer with (100) surface orientation and p-type (Boron) doping with a specified resistivity of 500 Ω-cm. Underneath the device layer is a 3 μm buried silicon dioxide (SiO_2) BOX layer. The device and BOX layers sit atop a silicon (Si) handle wafer of thickness 675 μm and a specified resistivity of 750 Ω-cm. Both the Si device layer and handle wafer are grown using the Czochralski crystal growth method.

5.3 Fabrication process of superconducting electromechanical circuit on silicon-on-insulator

Fabrication of the coupled coil resonator and H-slot resonator can be broken down into the following steps.

5.3.1 Device Patterning

In step (2), we pattern the H-slot resonator using electron beam (e-beam) lithography in ZEP-520A resist, and etch this pattern into the Si device layer using an inductively coupled plasma reactive ion etch (ICP-RIE). After the ICP-RIE etch, we clean the chips with a solvent chain (TCE, Acetone and IPA each for 4 mins) and a 12 sec buffered hydrofluoric acid (BHF) dip.

5.3.2 Capacitor Electrodes and Ground Plane

This layer patterns all of the electrical circuit, except for the coil wires. We start with a pre-bake at 180 °C for 2 min, and spin the front side with ZEP 520A at 2000 rpm, followed by another bake at 180 °C for 2 min. We use 100 keV electron beam lithography to pattern the ground plane and transmission lines (200 nA beam, 50 nm fracturing, 290 $\mu C/cm^2$ dose with PEC), as well as the capacitor wires, and the wires connecting the capacitors with the coil end and center (10 nA beam, 10 nm fracturing, 275 $\mu C/cm^2$ dose). This layer is carefully aligned to the alignment markers.

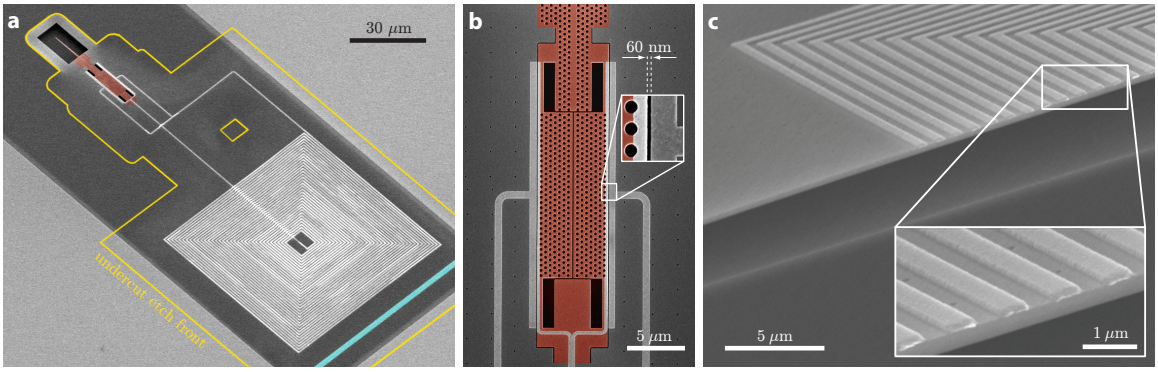

Figure 5.2: **a**, SEM image of the fabricated microwave coil resonator and H-slot mechanical resonator. The H-slot resonator region is colored red and the undercut region is outlined in yellow. The coupling wire is colored turquoise. **b**, A zoomed in SEM image of the H-slot mechanical resonator. Inset: a close-up of the 60 nm wide capacitor gap formed by a 250 nm wide Al electrode on the photonic crystal slab and a 550 nm wide Al electrode on the outer Si support membrane. Both wires are 60 nm thick, as is the ground plane. **c**, Cross-section image showing the suspended membrane with a coil on top. The Al forming the coil is 120 nm thick. The 3 μm thick dark area underneath the Si membrane is the undercut region where SiO_2 has been etched away. The bottom layer is the Si handle wafer.

We develop the chips in the same way and use a O_2 plasma ash process (50 sccm O_2, 0.74 bar, 13.56 MHz, 35 W, 2 min) to descum the surface before deposition of aluminum. For the deposition we use an electron beam evaporator (0.3 nm/s, 65 nm thickness at $1 \cdot 10^{-7}$ mbar to $2 \cdot 10^{-7}$ mbar). We then do a lift-off process in 80 °C NMP for $>$ 1 h and carefully rinse in ACE and IPA.

5.3.3 Scaffolding layer

Now we pattern a scaffolding layer to fabricate the cross-overs. After pre-baking, we spin LOR 5B at 3000 rpm and bake at 180 °C for 5 min, followed by spinning PMMA 950k A2 at 4000 rpm and baking at 180 °C for 5 min. We then beam write the negative pattern of the cross-over support structure using aligned electron beam lithography (200 nA beam, 25 nm fracturing, 1000 $\mu C/cm^2$ dose). The resist is developed using MIBK:IPA (1:3) for 1 min, and rinsed in IPA for 30 s. We then wet etch the scaffolding layer using MF-319 for 8 s, followed by a water rinse and IPA which stops the etch. Finally we remove the remaining PMMA layer with ACE (30 s) and reflow the LOR cross-over support layer on a hot plate at 200 °C for 10 min. This creates a structurally stable arc shaped cross over scaffolding.

5.3.4 Coil wire patterning

In order to pattern the narrow pitch coils, we spin PMMA 495 A8 at 2000 rpm, bake, spin PMMA 950k A2 at 2000 rpm, and bake again. Then we lithographically define the coil wires, which overlap the capacitor wires (10 nA beam, 10 nm fracturing, 1500 $\mu C/cm^2$ dose) and develop the resist as described previously. Development is followed by the same plasma ashing, deposition of aluminum (1 nm/s, 120 nm, p$\approx 2 \cdot 10^{-7}$ mbar), and lift off, during which the NMP (at 80 °C, 3 h) dissolves the LOR scaffolding layer.

5.3.5 DC contact wire

After a careful rinse with ACE and IPA we reproduce the previous layer recipe to pattern a small (500 nm$\times$4 μm) DC contact wire that symmetrically covers all overlap regions between capacitor wire and coil wire (two per coil and capacitor). Here we use an in-situ ion gun etch process (normal incidence with 4 cm gridded Kaufman source, 400 V, 21 mA for 5 min) right before the aluminum deposition of thickness 140 nm, in order to establish reliable contact. Contact is tested after lift-off on DC test structures of the same contact size located in the center of the chip. High resistance contacts with low capacitance at microwave frequencies would lead to additional parasitic in-series capacitances of the fabricated circuit.

5.3.6 Anhydrous HF Release

In a final step , we release the structure by using an anhydrous vapor hydrofluoric (HF) acid etch using the SPTS uEtch system. This etch is used to selectively remove the underlying BOX layer without attacking the Al metal or Si device layers. Not only is the removal of the SiO_2 BOX layer desirable from the standpoint of allowing the mechanical structure to move, but we have found that the presence of the underlying BOX layer results in a significant amount of electrical loss in the microwave resonator. Measurements of both co-planar waveguide and lumped element microwave resonators have shown that the microwave Q-factor is substantially degraded (resonances are difficult to detect; $Q_r \lesssim 100$) with the BOX layer present. Stripping off the Si device layer and forming microwave resonators directly on the BOX layer marginally improves the microwave Q-factor ($Q_r \approx 300$), whereas stripping off both the device layer and BOX layer realize microwave

Layers		
L1: markers	Chip Cleaning	TCE, 5' at power 2
		ACE: 3' at power 2
		IPA: 2' at power 2
		O2 Plasma ash, 5', 70% power, 0.7mBar, ~50 sccm flow.
		BHF dip: 12" HF, 10" water, 5" water, dry
	Spin & Bake	Prebake: 2' at 180C / Cooldown roughly 3'
		Resist: ZEP 520A
		Spin: 2000 rpm, 1500 rpm/s, 60"
		Bake: 2' at 180 ± 2 C / 1' cooldown
	Beam write, markers	10 nA beam, 10 nm fracturing
		295 uC/cm^2, global align
	Develop	2.5' ZEDN50, 30" MIBK rinse
	Cleaning	O2 Plasma ash, 2', 70% power, 0.7mBar, ~50 sccm flow.
		BHF dip: 12" HF, 10" water, 5" water, dry
	Evaporation	5 nm Cr (0.05 nm/s), 100 nm Gold (0.3 nm/s), 10 nm Cr, 20 nm Gold
	Lift Off	40' NMP at 150 C (hot plate), pipette, 60' NMP at 150 C (hot plate) in holder (vertical)
		Rinse and pipette in NMP individually, rinse in Acetone and IPA
L2: Patterning Si Membrane	Chip Cleaning	O2 Plasma ash, 5, 70% power, 0.7 mBar, ~50 sccm flow.
		BHF dip: 5" HF, 10" water, 5" water, dry
	Spin & Bake	Prebake: 2' at 180C / Cooldown roughly 3'
		Resist: ZEP 520A
		Spin: 5000 rpm, 1500 rpm/s, 60"
		Bake: 2' at 180 ± 2 C / 1' cooldown
	Beam write, holes / nanostrings / trenches	300 pA beam, 2.5 nm fracturing / 300 pA, 2.5 nm / 10 nA, 10 nm
		holes: 390 uC/cm^2 / nanostring: 220 uC/cm^2 with PEC / trenches: 245 uC/cm^2 (global align)
	Develop	2.5' ZEDN50, 30" MIBK rinse
	Etch	39 sccm C4F8, 12 sccm SF6, stabalize bias to 72-73 V DC bias,22 W RF forward power, 600W ICP, 20C Table Temperature, 5 min 45 sec
	Chip Cleaning	remove thermal paste with tce and wipe, 2 min tce (US1 hold with tweezer) 30 min hot (HP at 150 deg) nmp, ace and ipa rinse
		O2 Plasma ash, 5', 70% power, 0.7mBar, ~50 sccm flow.
	Undercut	BHF dip: 5" HF, 10" water, 5" water, dry
L3: Groundplane, TL, capacitors, crosswire, bondpads, DC test and coupler wires	Spin & Bake	Prebake: 2' at 180C / Cooldown roughly 3'
		Resist: ZEP 520A
		Spin: 2000 rpm, 1500 rpm/s, 60"
		Bake: 2' at 180 ± 2 C / 3' cooldown
	Beam write: ground plane, transmission lines, coupler wires, dc wires and coil cross wires	ground plane: 201 nA beam, 50 nm fracturing / 295 dose (with simple PEC)
		all wires: 10 nA beam / 10 nm fracturing / 295 dose (couplers global aligned, others with pattern markers)
	Develop	2.5' ZEDN50, 30" MIBK rinse
	Cleaning	O2 Plasma ash, 2', 70% power, 0.7mBar, ~50 sccm flow.
		Buffered HF dip: 1' 30" BHF, 5' water, 10' water, careful blowdry
	Evaporation	3 min Ti on wall (0.2 nm/s) for better vacuum
		60 nm Al (0.2 nm/s)
	Lift Off	in NMP (preheated, hotplate at 150C) for at 1 h then pipette and change to second preheated beaker. Another 3 h then pipette again. Ace rinse, IPA rinse, check, Rinse and dry
L4: scaffolding layer for air bridges	Spin & Bake	prebake 2 min 180C, LOR 5B - 3000 RPM, 1500 ramp, 5 min hot plate bake at 180 C PMMA 950k A2 - 4000 RPM, 1500 ramp, 6 min hot plate bake at 180 C
	Beam write: device outline and cut outs	201 nA beam, 25 nm fracturing / 800 dose (no PEC)
	Develop	1 min MIBK:IPA (1:3), 30 sec IPA
	Wet etch	MF319: 6" (exact), Water: 5", IPA 10"
	Clean	Acetone: 45", IPA rinse (10")
	Reflow	on HP, 200 C for 5 min uncovered, and 5 min covered with Al cover, cooldown 3'
L5: coils	Cleaning	no cleaning
	Spin & Bake	2 min. hotplate bake at 180 C, 3 min cooldown, PMMA 495k A8, 2000 rpm, 1000 rpm/s, for 60", 2 min. bake on hotplate at 180 C, 3 min cooldown, PMMA 950k A2, 2000 rpm, 1000 rpm/s for 60", 2 min bake on hotplate at 180C
	Beam write: coils wires and qubit capacitors	10 nA beam, 10 nm fracturing / 1500 dose (no PEC)
	Develop	1 min MIBK:IPA (1:3), 30 sec IPA
	Cleaning	O2 Plasma ash, 2', 70% power, 0.7mBar, ~50 sccm flow., HF vapor 2x tiny flashes
	Evaporation	3 min Ti on wall (0.2 nm/s) for better vacuum, 120 nm Al (1 nm/s)
	Liftoff	in NMP (preheated, hotplate at150C) for at 1 h, then pipette change to second preheated beaker. Another 3 h then pipette again. Ace rinse, IPA rinse, check, rinse and dry
L6: Band aids	cleaning	no cleaning
	Spin & Bake	2 min prebake on hot plate at 180 C, 3 min cooldown, PMMA 495k A8, 2000 rpm, 1000 rpm/s, for 60", 2 min bake on hotplate at 180 C, 3 min cooldown, PMMA 950k A2, 2000 rpm, 1000 rpm/s for 60", 2 min bake on hotplate at 180C, 3 min cooldown
	Beam write: band aids and undercuts	10 nA beam, 10 nm fracturing, 1000 dose for Ion gun area 10nA beam, 10 nm fracturing, 400 dose for undercut area
	Develop	1 min MIBK:IPA (1:3), 30 sec IPA
	Cleaning	O2 Plasma ash, 2', 70% power, 0.7mBar, ~50 sccm flow
	Evaporaion	ION gun 5 min, 400 V, 21 mA, 0 degree, then 3 min Ti on wall (0.2 nm/s) for better vacuum, 140 nm Al (1 nm/s)
	Lift Off	in NMP (preheated, hotplate at150C) for at 1 h, then pipette and change to second preheated beaker, Let it be in solution 1-2 h and then pipette again. Ace rinse, ipa rinse, check, rinse dry

Table 5.1: step by step fabrication process of aluminum(Al) on Silicon-on-insulator process involving anhydrous HF vapor release of the substrate

resonators with $Q_r \approx 4 \times 10^4$ when fabricated directly on the Si handle wafer. The release of the structure is facilitated by patterning an array of small (100 nm diameter) holes into the Si device layer during step (1). The array of release holes are on a 2 μm pitch and cover the region containing

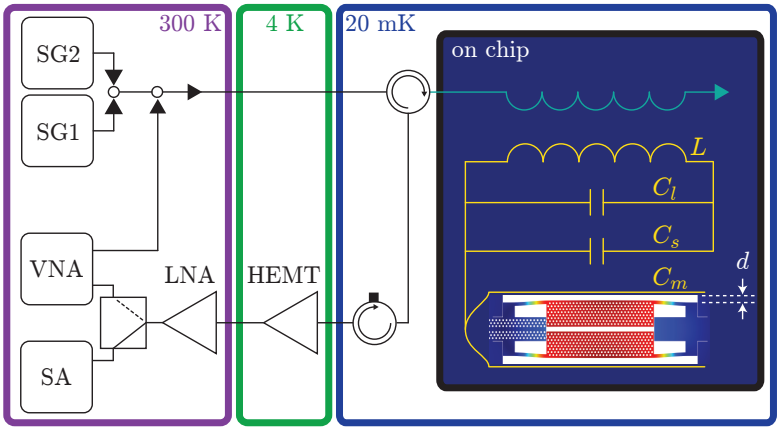

Figure 5.3: Schematic of the electromechanical circuit and measurement setup. The electromechanical circuit (yellow) is inductively coupled to a 2 μm wide wire (turquoise) which shorts to ground and reflects the signal. Acronyms: SG_i = microwave signal generator, VNA = vector network analyzer, SA = spectrum analyzer, LNA = low-noise amplifier, HEMT = high-electron-mobility transistor amplifier.

the coil and H-slot resonator. A timed etch of 75 min is used to remove $\approx$ 6 μm of SiO_2, resulting in complete removal of the BOX layer underneath the microwave circuit. A scanning electron microscope (SEM) image of the fully released structure is shown in Fig. 5.2(a). Zoom-in images of the H-slot mechanical resonator and undercut inductor coil are shown in Figs. 5.2(b) and (c), respectively.

5.4 H-Slot Resonator Measurements

Electromechanical measurements of the fabricated coil resonator are performed in a dilution refrigerator down to a temperature of $T_f \approx 11$ mK. Microwave signals are launched onto the SOI chip using a 50 Ω co-planar waveguide. The co-planar waveguide is terminated by extending the center conductor with a 2 μm wide wire and then shorting it into ground. The wire is passed within 9 μm of the side of the inductor coil [see Fig. 5.2(a)], thus providing large inductive coupling to the microwave resonator. A region extending roughly 10 μm from the edge of the surrounding ground plane of the co-planar waveguide an inductive coupling wire is also undercut and the BOX layer fully removed. Read-out of the reflected microwave signal is performed using the measurement scheme shown in Fig. 5.3. The input line is thermalized at each stage of the fridge with a series of

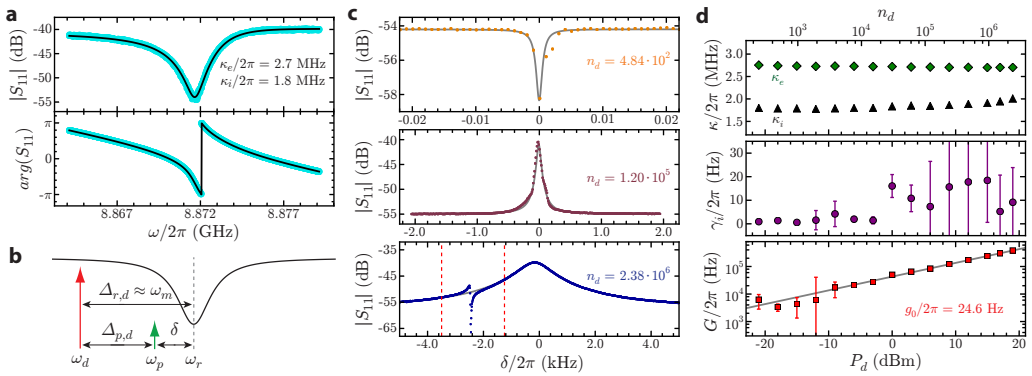

Figure 5.4: **a**, Phase and amplitude response of the microwave resonator at fridge temperature $T_f \approx 11$ mK and on-resonance cavity photon number of $n_p = 3.3$. The intrinsic loss rate κ_i and external coupling rate κ_e are extracted by fitting the curves with a modified Lorentzian cavity model to take into account the asymmetry in the background frequency response. **b**, Schematic showing two-tone EIT measurement procedure. A strong drive tone at frequency ω_d is placed on the red sideband of the microwave cavity and the cavity response is swept by a weak VNA probe at ω_p. **c**, Plot of the measured EIT spectra at a series of drive intra-cavity photon numbers for a fridge temperature of $T_f \approx 11$ mK. From top to bottom: $n_d = 484$ (orange curve), 1.20×10^5 (maroon curve), and 2.38×10^6 (blue curve). Note for the blue curve at $n_d = 2.38 \times 10^6$, a weakly coupled auxiliary mechanical mode can be observed. The frequency range between the vertical red dashed lines, surrounding the auxiliary mechanical resonance, were omitted for fitting purposes. **d**, Plot of the fit values from the measured EIT spectra using Eq. (3.24) for cavity coupling rates (top), intrinsic damping (middle), and parametrically enhanced coupling rate (bottom). Error bars correspond to a 95% confidence interval in the estimated fit parameter.

attenuators to eliminate Johnson thermal noise from the room temperature environment, yielding a calibrated input line attenuation of $\mathcal{A} = -73.9$ dB. The reflected signal is redirected using a pair of circulators at the mixing chamber stage of the fridge and then sent into an amplifier chain consisting of a HEMT amplifier at the 4 K fridge stage and a low-noise amplifier at room temperature. The total amplifier gain is 52 dB, with an equivalent added microwave noise photon number of $n_{\text{add}} \approx 30$.

Figure 5.4(a) shows the measured magnitude and phase of the reflected microwave signal versus frequency from a vector network analyzer (VNA) used to probe the electrical properties of the device. The microwave resonance frequency is measured to be $\omega_r/2\pi = 8.872$ GHz, in close correspondence to the resonance frequency based upon the simulated values of the coil inductance and the motional and stray capacitance of the circuit. At the lowest base temperature of our fridge, $T_f \approx 11$ mK, we measure an intrinsic microwave cavity loss rate of $\kappa_i/2\pi = 1.8$ MHz at an intra-cavity photon number on resonance of $n_p = 3.3$, corresponding to an internal quality factor of

$Q_{r,i} = 4890$. The external coupling rate to the resonator is measured to be $\kappa_e = 2.7\,\text{MHz}$, putting the device well into the overcoupled regime. We note that for similar coil resonators (without an H-slot resonator and coil cross-overs) which were coupled more weakly using a transmission as opposed to reflection geometry, we have observed internal quality factors as high as $Q_{r,i} \approx 2 \times 10^4$, close to the measured Q-values for resonators fabricated directly on the Si handle wafer. The additional source of the microwave loss will be explained in the next chapter.

To characterize the mechanical properties of the H-slot resonator, and determine the strength of its radiation pressure coupling to the microwave coil resonator, we perform two-tone pump and probe measurements as illustrated in Fig. 5.4(b). Here, a strong drive tone of power P_d is applied at frequency ω_d on the red motional sideband of the microwave cavity resonance while a weak probe tone is scanned across the cavity resonance. Interference between the anti-Stokes sideband of the drive tone and the weak probe tone results in a form of mechanically-mediated electromagnetically-induced transparency (EIT) [63, 83, 84], which for pump detuning near two-photon resonance ($\Delta_{r,d} \equiv \omega_r - \omega_d \approx \omega_m$) yields a reflection spectrum given by Eq. (3.24). A subset of the measured spectra over a range of drive powers are shown in Fig. 5.4(c) around the EIT transparency window. The drive detuning at two-photon resonance corresponds to the mechanical resonance frequency, and is found to be $\omega_m/2\pi = 9.685$ MHz, very close to the numerically simulated resonance frequency of the in-plane differential mode of the H-slot resonator. The cooperativity associated with the coupling of the microwave cavity field to the mechanical resonator is given by $C \equiv 4G^2/\kappa\gamma_{m,i}$, where $\gamma_{\text{EM}} \equiv 4G^2/\kappa = 4n_d g_0^2/\kappa$ is the back-action-induced damping of the mechanical resonator by the microwave drive tone. At low drive powers corresponding to $C < 1$, we observe a narrow dip at the center of the broad microwave cavity resonance. As the drive power is increased and $C > 1$ the dip becomes a peak in the reflected signal and the bandwidth of the transparency window increases with pump power. At the highest powers we observe a substantially broadened transparency window, where we observe the presence of a second, spurious mechanical resonance about 2.4 kHz below that of the strongly coupled resonance. We attribute this spurious resonance to weak hybridization of the extended membrane modes of the undercut SOI with the localized in-plane differential mode of the H-slot resonator.

Ignoring the spurious mechanical mode, we fit the measured EIT spectra using Eq. (3.24 and

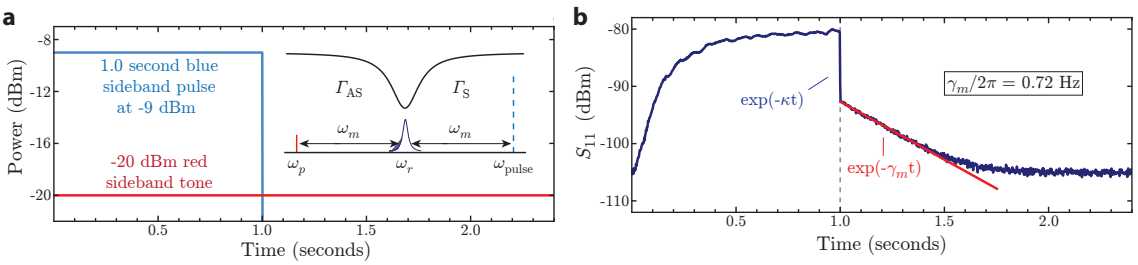

Figure 5.5: **a**, Schematic showing the time-domain mechanical ring-down protocol, wherein a strong blue pulse at $\omega_{pulse} = \omega_r + \omega_m$ populates the mechanics and a weak probe tone at $\omega_p = \omega_r - \omega_m$ is used to monitor the energy in mechanical resonator. Inset: schematic showing the frequency and scattering of the applied tones used to ring-up and monitor the mechanical resonator. Here, $\Gamma_S \approx (4n_{pulse}g_0^2/\kappa)(n_m + 1)$ [$\Gamma_{AS} \approx (4n_p g_0^2/\kappa)n_m$] is the Stokes [anti-Stokes] scattering rate of the pulse [probe] tone, where n_{pulse} [n_p] is the intra-cavity pulse [probe] tone photon number. **b**, Time-domain mechanical ring-down measurement at $T_f \approx 11$ mK. A steep decay resulting from the leakage of photons from the cavity is followed by a slow decay dominated the intrinsic mechanical damping of the resonator is observed.

extract the microwave cavity parameters (κ_i, κ_e, ω_r), the intrinsic mechanical damping ($\gamma_{m,i}$), the mechanical resonance frequency (ω_m), and the parametrically-enhanced electromechanical coupling rate ($G = \sqrt{n_d}g_0$). Figure 5.4(d) plots each of these fit parameters versus drive power and intra-cavity drive photon number (n_d). κ_i is found to weakly rise with n_d, most likely due to heating of the SOI membrane resulting from absorption of the microwave pump. For intra-cavity photon number $n_d \gtrsim 5 \times 10^6$, we no longer observe a microwave resonance, suggesting that absorption of the microwave pump causes the superconducting circuit to go normal. Fitting the measured curve of G versus pump photon number yields an estimate for the vacuum electromechanical coupling rate of $g_0/2\pi = 24.6$ Hz, in good correspondence with the simulated value of 29.3 Hz. The slight discrepancy is likely attributable to an under-estimation of the true capacitor gap size due to overhang of the Al electrode into the gap. For a 70 nm dielectric gap, consistent with an additional 10 nm overhang of Al estimated from cross-sectional images of similar devices, the simulated vacuum coupling rate drops to $g_0/2\pi = 24.4$ Hz

At low drive powers, the EIT transparency window bandwidth is dominated by the intrinsic mechanical linewidth, $\gamma_{m,i}$. However, we observe a frequency jitter of the mechanical resonance frequency. The range of the frequency jitter is of the order of several Hz on the second timescale, and saturates at approximately 20 Hz for timescales on the order of tens of minutes. The source of

the mechanical frequency jitter is unknown, but may be related to the excess heating we observe at the lowest fridge temperatures as described below. The resolution bandwidth of the VNA is also limited to 1 Hz, and combined with the frequency jitter leads to significant distortion and blurring of the measured EIT spectrum at low drive power as can be seen in the top plot of Fig. 5.4(c). Estimates of $\gamma_{m,i}$ and the corresponding cooperativity C are thus unreliable from the EIT spectra alone.

To directly measure the intrinsic damping rate $\gamma_{m,i}$ we perform a mechanical ring-down measurement as shown in Fig. 5.5. Here, a strong blue-detuned pulse tone at frequency $\omega_{pulse} = \omega_r + \omega_m$ is applied for 1 s to amplify the thermal mechanical motion of the mechanical resonator through dynamic back-action [99–101]. A weak red-detuned probe tone at $\omega_p = \omega_r - \omega_m$ is applied to the microwave cavity in order to read-out the phonon occupancy of the resonator after the blue detuned pulse is turned off. A spectrum analyzer with resolution bandwidth set to RBW$= 1$ kHz is used to measure the motionally scattered photons near the cavity resonance from the pulse and probe tones, providing a time domain signal proportional to the mechanical resonator phonon occupancy as shown in Fig. 5.5(b).

Fitting the decay of the spectrum analyzer signal after the pulse tone is turned off, and after the initial rapid decay of pulse photons from the cavity, yields a mechanical damping rate of $\gamma_m/2\pi = 0.72$ Hz. Note that as the probe tone power of -20 dBm corresponds to an intra-cavity photon number of only $n_p \approx 300$, the dynamic back-action damping of the probe is small but non-negligible at $\gamma_{\rm EM}/2\pi \approx 0.16$ Hz. The corresponding intrinsic mechanical damping rate is thus approximately, $\gamma_{m,i}/2\pi \approx 0.56$ Hz, corresponding to a mechanical quality factor of $Q_m = 1.7 \times 10^7$.

The red-sideband pump configuration ($\Delta_{r,d} = \omega_m$) used to measure the EIT spectra also cools the mechanical resonator. Using a spectrum analyzer to measure the anti-Stokes scattered drive photons near the microwave cavity resonance, as shown schematically in Fig. 5.6(a), and calibrating the measured noise spectrum allows one to infer the average (noise/thermal) phonon occupancy (n_m) of the mechanical resonator as a function of the drive power. This sort of mechanical mode thermometry [22, 84] at the lowest fridge temperature of $T_f \approx 11$ mK shows large fluctuations in the inferred mechanical mode temperature ($T_m = 20 - 200$ mK), as a function of both time and drive power. The source of this anomalous mechanical mode heating is not well understood at this point, but may be related to coupling between the driven microwave resonator and two-level

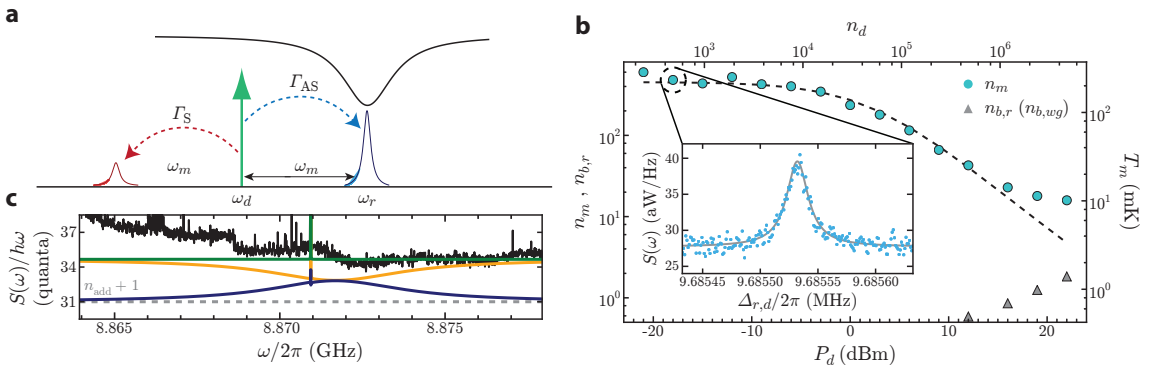

Figure 5.6: **a**, Schematic showing thermometry measurement scheme, wherein a red detuned drive tone is used to simultaneously cool and measure the average energy in the mechanical resonator through anti-Stokes scattering proportional to phonon occupancy of the resonator. $\Gamma_{AS} \approx (4n_d g_0^2/\kappa)n_m$ is the cavity-enhanced anti-Stokes scattering rate of the drive tone proportional to n_m. $\Gamma_S \approx (4n_d g_0^2/\kappa)(\kappa/4\omega_m)^2(n_m+1)$ is the cavity-suppressed Stokes scattering rate of the drive tone proportional to $n_m + 1$. **b**, Cooling curve obtained by fitting the measured microwave noise spectrum using a model which includes noise squashing and heating effects due to thermal noise in the microwave cavity and the input coupler. Spectra are taken at a fridge temperature of $T_f = 211$ mK. Blue circles correspond to the inferred average mechanical mode occupancy (n_m) from fits to the measured noise (see inset). Grey triangles are the fit input waveguide ($n_{b,wg}$) and cavity ($n_{b,r}$) thermal noise occupancies from the measured noise background level. The dashed line indicates the predicted occupancy as given by $n_{f,m}/(1+C)$, where C is determined from the EIT fit values for the vacuum coupling rate ($g_0/2\pi = 25.1$ Hz) and the intrinsic damping rate ($\gamma_{m,i}/2\pi = 25.7$ Hz) taken at a fridge temperature of $T_f \approx 211$ mK. **c**, Plot of the measured noise spectral density (black curve) and modeled noise background (green curve) at $P_d = 22$ dBm. The orange curve corresponds to the expected spectral noise density due to the waveguide bath ($n_{b,wg}$) alone while the navy curve shows the expected contribution from the resonator bath ($n_{b,r}$). The global offset of $n_{add} + 1$ is shown as a grey dashed line.

systems (TLS) [102] present in the native oxide on the surface of the silicon device [103–105]. TLS can not only absorb energy from the microwave drive, but also may hybridize with the microwave cavity and influence the transduction of mechanical motion yielding artificially high or low inferred mechanical mode occupancy [22].

To better characterize the back-action cooling of the mechanics, we performed a cooling sweep at a fridge temperature of $T_f \approx 211$ mK, where the anomalous heating effects seen at $T_f \approx 11$ mK are less significant in comparison to the thermal bath of the fridge. A plot of the inferred mechanical mode occupancy (n_m) and corresponding mode temperature (T_m) versus the drive power applied on the red-sideband ($\Delta_{r,d} \approx \omega_m$) is shown in Fig. 5.6(b). At low drive powers where $C \ll 1$ and back-action cooling is expected to be negligible, we find that the mechanics thermalizes to

an occupancy very close to the mechanical thermal occupancy at the fridge temperature, $n_{f,m} = 453$. For comparison a plot of the ideal cooling curve, $n_m = n_{f,m}/(1+C)$, due to radiation pressure back-action is shown as a dashed curve in Fig. 5.6(b). Here we use an intrinsic damping rate ($\gamma_{m,i}/2\pi = 25.7$ Hz) and vacuum coupling rate ($g_0/2\pi = 25.1$ Hz) inferred from EIT measurements at $T_f \approx 211$ mK. The measured mechanical mode occupancy is in good agreement with theory, except at powers $P_d > 10$ dBm where we again observe anomalous heating effects. Nonetheless, we are able to perform well over a decade of cooling and reach occupancies as low as $n_m \approx 16$.

In addition to the measured Lorentzian noise peak of the mechanical resonance, we also observe broadband noise which increases with the drive power. Figure 5.6(c) shows a plot of the measured broadband noise (back curve) at the highest intra-cavity drive photon number of $n_d = 4.75 \times 10^6$. This broadband noise does not seem to be phase noise of our microwave source as addition of a narrowband input filter had no effect on the measured noise spectrum. Assuming that the noise is associated with an elevated electrical noise temperature of the device, we include both an input waveguide thermal noise occupancy ($n_{b,wg}$) and a cavity thermal noise occupancy ($n_{b,r}$) to our model. Taking the waveguide and cavity to be at the same noise temperature (i.e., $n_{b,wg} = n_{b,r}$) yields a flat reflection noise spectrum as shown in Fig. 5.6(c). Fitting the noise background at each drive power yields an estimate for the cavity and waveguide noise photon numbers, which are shown versus drive power as grey triangles in Fig. 5.6(b). The inferred effective noise temperature of the microwave cavity at the highest drive power is $T_r \approx 1$ K, close to the critical temperature for Al [106] and consistent with the circuit going normal at higher drive powers.

Enhancement in the back-action cooling and electro-mechanical cooperativity of the current devices can be realized most straightforwardly through reduction in the microwave resonator loss. Significant reduction in the microwave loss and heating effects should be attainable through the use of higher resistivity Si [104, 105]. The vacuum electro-mechanical coupling rate may also be increased to $g_0/2\pi \approx 100$ Hz through optimization of the circuit layout and the mechanical mode to reduce stray capacitance, reduction of the capacitor gap to reported values of $d \approx 30$ nm [78] and increasing the zero point amplitude of the mechanical mode.

Chapter 6

Nano-String Electro-Opto-Mechanical Transducer

6.1 Introduction

As discussed in previous chapter, to achieve ground-state cooling of the mechanical resonator, we need to improve both the quality factor of the microwave resonator as well as enhance the electromechanical coupling. To achieve this, we first discuss the microwave loss sources and present an improved design of the silicon membrane, allowing us to achieve higher microwave quality factor, as high as $Q_r \approx 100$k. Secondly, we present a mechanical resonator with much less effective motional mass, allowing us to reach single photon electromechanical coupling $g_0/2\pi \approx 200$Hz.

6.2 Improvement on Microwave Quality Factor

SOI presents a unique platform for integrating microwave, mechanical, and optical circuits. This is particularly interesting in the context of recent proposals and experimental efforts to utilize mechanical elements as quantum converters between microwave and optical light [30, 83, 107–110]. But eliminating the additional source of loss for the microwave circuits is required before using SOI as a platform useful for quantum measurement. To reduce the sources of loss in the released silicon membrane, we used the high resistivity silicon wafer at the device layer. The resistance of the silicon membrane directly relates to the amount of impurities in the silicon structure which can perform as sources of loss either through TLS mechanism or a leakage current. The 'H-Slot' resonator presented in the previous chapter was fabricated on silicon with much lower resistivity (700 Ω). Therefore,

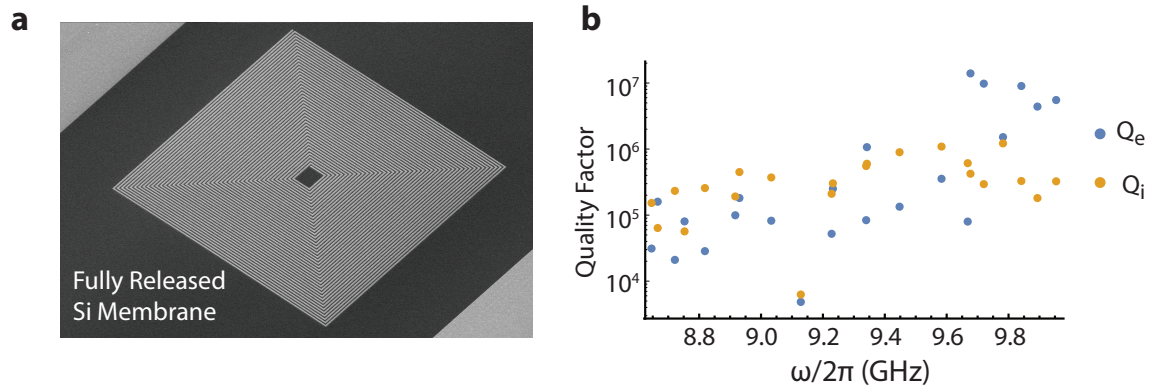

Figure 6.1: **a**, A SEM of a microwave resonator on fully released membrane on high-resistivity $R >$ 5kΩ.Cm SOI. **b** Quality factor of a series of microwave resonator at single photon power with narrow frequency range between 8.8 GHz and 10 GHz and various coupling efficiency Q_e ranging from 20k to 10m.

we used a SOI wafer with resistivity $R > 5$ kΩ.cm to improving the resistance by an order of magnitude. Additionally we noticed that the losses are magnified substantially by placing the circuit close to the SiO_2 etch front, owing to the fact that amorphous materials like SiO_2 induce losses by driving transitions of two-level systems (TLS). To alleviate this, we increased the under-cut area around the microwave resonator further to about 20μm into the ground plane. Figure 6.1(a) shows a microwave resonator fabricated on high resistivity SOI and a fully released membrane. To characterize the losses, we fabricated a series of resonator inductively coupled to a 50 Ω waveguide with various coupling to the input feed line. To avoid frequency crowding we have varied the resonance frequency between 8.8 GHz and 10 GHz. We measure the quality factor of these resonator utilizing a vector network analyzer and extract the internal and external coupling to the microwave feed line from the phase and amplitude response of each resonator. Figure 6.1(b) shows internal microwave quality factor Q_i (external quality factor Q_e) of these resonator measured at single photon power. Almost all the microwave resonators have an internal quality factor exceeding 100k, improving by factor of ≈ 30 compared to the microwave resonator made on low resistivity silicon and without the modified ground plane.

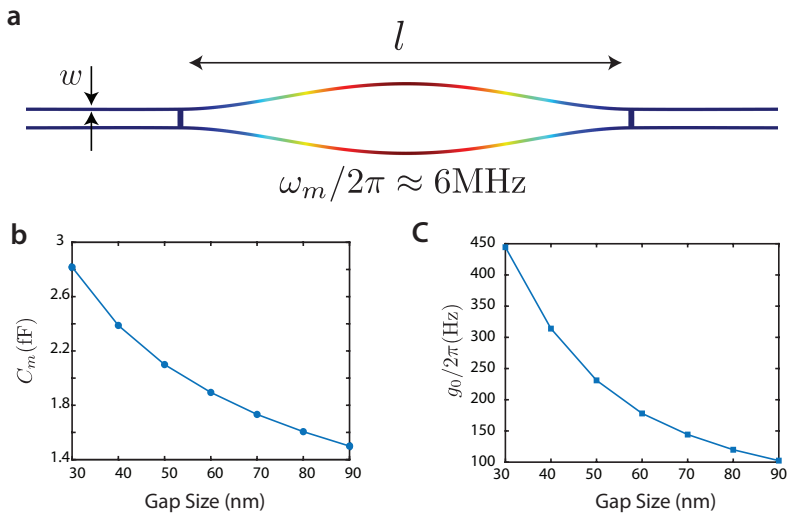

Figure 6.2: **a,** FEM Simulation of the mechanical breathing mode of the 'nano-string' resonator with red(blue) showing the region with maximum(minimum) deformation of the mechanical mode. The length of the moving arms are $l = 20\mu$m and each arm has the width$w = 150$nm and are fully covered with aluminum. **b,** Showing the moving capacitance C_m versus gap size. **c,** shows the single photon electromechanical coupling assuming a microwave resonator with inductance of L=43nH and microwave circuit parasitic capacitance $C_s = 3.01$ fF.

6.3 Mechanical Design

Other than the microwave cavity losses, the 'H-Slot' resonator also suffered from the low electromechanical coupling owing to the low zero point motion of the mechanical oscillator x_{zpf} and big motional capacitors gap, which resulted in requiring additional driving power to back-action cool the mechanical resonator. Zero-point amplitude of the mechanical motion depends crucially on the mechanical frequency and the effective motional mass of the mechanical resonator. To reduce the effective mass of the mechanical oscillator, we have significantly reduced the width of the moving arms of the mechanical cavity. Figure 6.2(a) shows the FEM simulation of the breathing mode of the mechanical resonator with the width of $w = 150$nm fully covered with aluminum with thickness $t_{\text{Al}} = 60$nm and length of $l = 20\mu$m. The small extensions on the two sides of the mechanical resonator are mirror cells with the length $l = 7\mu$m to reduce the parasitic coupling of the mechanical resonator to the rest of the released Silicon membrane and isolating the mechanical mode. The mechanical mode has the frequency $\omega_m/2\pi = 6$MHz, and the effective mass $m_{\text{eff}} = 1.6$ pg, resulting in zero-point amplitude of $x_{\text{zpf}} = 35$ fm. Fig. 6.2(b,c) shows the moving capacitance and single

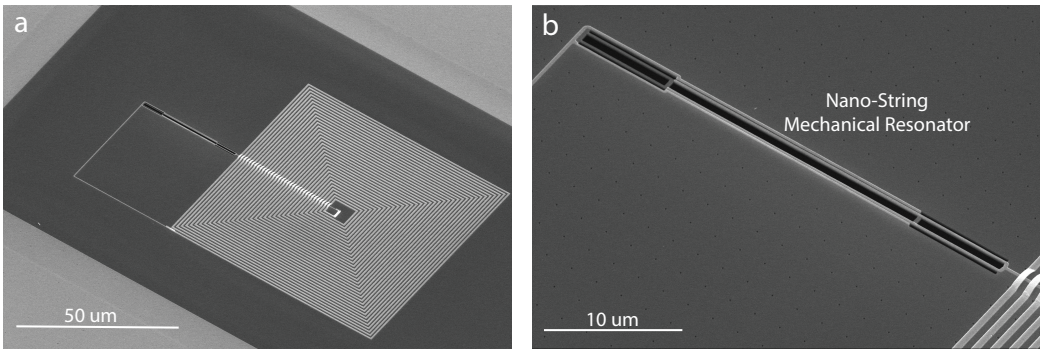

Figure 6.3: **a,** A scanning electron microscope (SEM) image of Nano-string. The aluminum is in white and the released silicon membrane is in black. As it can be seen the etch front of the released membrane extended far back into the ground plane surrounding the electromechanical device reducing the effect of the lossy SiO_2 on the microwave circuit. **b,** A zoom in image of the nano-string mechanical device. Aluminum electrodes (in white) cover the whole arms of the mechanical resonator. The aluminum electrodes are separated by gap of 70 nm. At cold temperature due to the tensile stress of the aluminum electrodes and the compressive stress of the released membrane the gap shrinks to 45 nm.

photon electromechanical coupling $g_0/2\pi$ of the 'Nano-String' resonator versus gap sizes.

A scanning electron microscope image of the fabricated device is shown in Fig. 6.3. As it can be seen, the etch front of the released membranes extends far back into the ground plane to reduce the effect of the lossy SiO_2 on the superconducting microwave circuit.

6.4 Nano-String Measurements

The measurement of the nano-string electromechanical microwave resonator is done in a dilution fridge at temperature of $T_f \approx 10$ mK. The microwave resonance frequency of $\omega_r/2\pi = 10.780$ GHz is measured with external coupling strength of $\kappa_e/2\pi = 60$ kHz in close correspondence to the simulated resonance frequency from FEM simulation in Sonnet [76]. However, the internal quality factor of the microwave resonator is power dependent. We measure an internal microwave cavity loss of $\kappa_i/2\pi = 260$ kHz at single intra-cavity photon number $n_p = 1$ and $\kappa_i/2\pi = 82$ kHz at intra-cavity photon number of $n_p = 1000$ approaching critically coupled regime.

We find the mechanical frequency by stepping a strong pump detuned from the microwave cavity while scanning the microwave cavity with a weak probe tone. When the detuning of the drive power is equal to the mechanical frequency $\Delta_{r,d} = \omega_d - \omega_r = \omega_m$, a transparency window shows up in

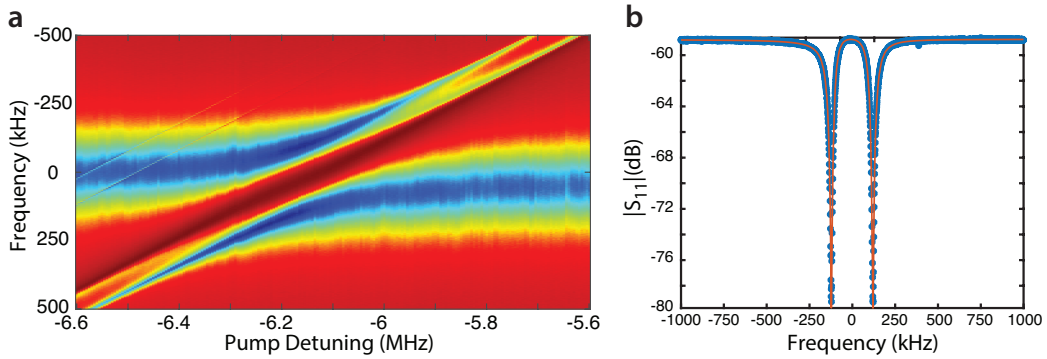

Figure 6.4: **a,** Color plot of normalized coherent response of the microwave cavity versus the drive pump detuning from the microwave cavity. The pump is at 22 dBm of power. **b,** The reflection spectrum of the microwave cavity at $\Delta_{r,d} = \omega_r - \omega_d = \omega_m$.

the coherent reflection response of the microwave cavity analogous to the electromagnetic induced transparency (EIT) [83, 84, 111].

6.4.1 Electromagnetically Induced Transparency and Electromechanical Coupling

To characterize the mechanical properties of the 'Nano-String' mechanical resonator as well as the strength of the coupling to the microwave cavity, we again perform the two-tone pump-probe measurement. A strong drive tone of power P_d is applied at frequency $\omega_d = \omega_r - \omega_m$ on the red motional sideband of the microwave cavity resonance while a weak probe tone scans across the microwave cavity resonance. Interference of the reflected probe signal occurs between that part of the probe field that enters the microwave resonator and is directly re-emitted, and that part of the probe field that enters the cavity, interacts with the mechanical resonator and is then re-emitted from the cavity.

For the case of the red side-band pumping the reflected spectrum is given by equation Eq. (3.24). The measurements spectra are plotted in Fig. 6.5(a). We use the fit to the spectra to extract the back-action induced linewidth γ_{EM} and parametrically enhanced electromechanical coupling G. Figure 6.5(b) shows the measured parametrically enhanced electromechanical coupling G for various drive powers P_d. The parametrically enhanced electromechanical coupling relates to single photon coupling by $G = \sqrt{n_d} g_0$. Calibrating the input power at the sample input and calculating the intra cavity photon number of the microwave resonator, we measure single photon electromechanical coupling $g_0/2\pi = 230$ Hz corresponding to a gap size of roughly 50 nm.

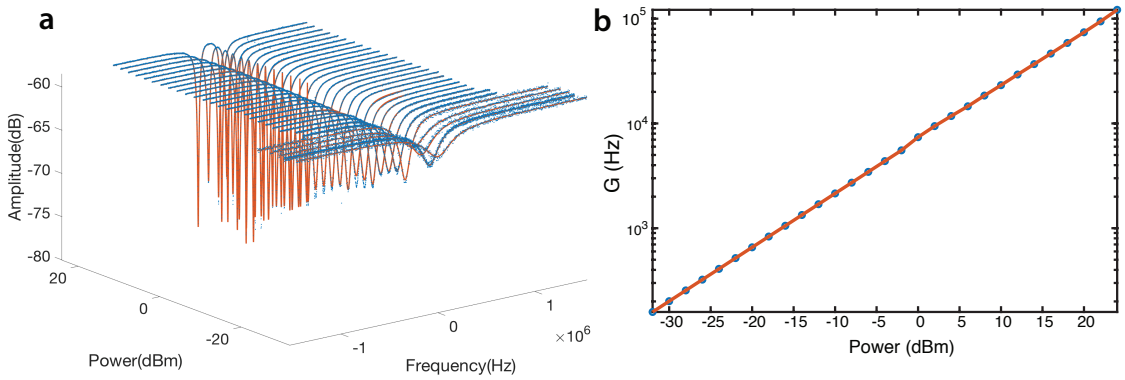

Figure 6.5: **a,** Plot of EIT measured spectra at a series of pump drive power P_d. The measured data are shown as blue dots and the fit to the data are shown as orange lines. **b,** Measured enhanced electromechanical coupling $G/2\pi$ for various powers of drive tone. The measured values are shown as blue circles and a linear fit is used to extract the g_0.

6.4.2 Mechanical Ringdown measurement

We use mechanical ringdown measurement to extract the intrinsic linewidth of the mechanical resonator. This measurement is independent of the mechanical frequency jitter and allows us to directly measure the intrinsic damping rate of the mechanical resonator. In this measurement, we use a strong blue pulse detuned from the microwave cavity by a mechanical frequency to amplify the mechanical resonator motion (lasing) and populate it with phonons. Then we use a weak red tone to read-out to probe the amplitude of the mechanical motion as a function of the time. Fig. 6.6 shows the mechanical ringdown measurement of the Nano-String mechanical resonator.

In this measurement the blue tone at -5 dBm and pulse width of 500 ms is used to populate the mechanical resonator with phonons and red tone at power -36 dBm is used to monitor the decay of the mechanical amplitude. We fit an exponential curve to the measured decay curve to extract the total damping rate γ_m. Subtracting the red side band back-action induced mechanical damping allows us to directly measure the intrinsic mechanical damping rate γ_i. The intrinsic damping for this device is measured to be $\gamma_i = 2.83$ Hz, resulting in mechanical quality factor $Q_m = 2.1$ M.

6.4.3 Strong Coupling limit

At high enough power, the back action induced mechanical damping rate exceeds all other sources of the loss in the system (*i.e.* $\gamma_{em} > \kappa, \gamma_i$). The crossover for our Nano-String device occurs at power

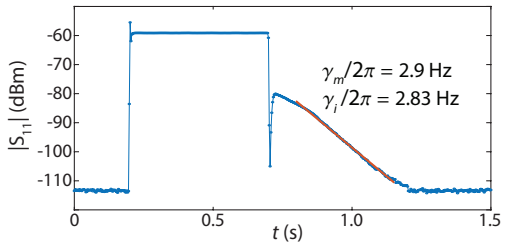

Figure 6.6: Plot of mechanical ringdown measurement of Nano-String electromechanical cavity. A strong blue pulse at $\omega_{pulse} = \omega_r + \omega_m$ and power -5 dBm populates the mechanics for 500 ms and a weak probe tone at $\omega_p = \omega_r - \omega_m$ and power -36 dBm is used to monitor the energy in mechanical resonator. The back-action induced damping rate is calculated from the EIT measurement and subtracted from the total damping rate of the mechanical resonator γ_m.

of 24 dBm, corresponding to microwave intra cavity photon number $n_d = 196000$ and enhanced parametric coupling of $G \approx 134$ kHz. This is a point at which the electromechanical system enters a strong coupling regime. At this power, the eigen modes of the driven electromechanical system are hybrids of mechanical and electromagnetic resonances and the damping rate for each of the modes approaches $(\kappa + \gamma_{\text{em}})/2$. This coupling results in the splitting of the original modes. Figure 6.4(a,b) shows the anti-crossing and normal mode splitting of the microwave cavity mode as we tune the mechanical response into the microwave cavity close to the strong coupling regime.

6.4.4 Incoherent Response of the Electromechanical Circuit and Mechanical Thermometry

To infer the average noise/thermal phonon occupancy n_m of the mechanical resonator as a function of the drive power, we again use the red sideband configuration of the EIT measurement. In the case of red detuned pumping, the pump photons are mechanically up-converted to the cavity resonance and absorb a phonon through the process. We use a spectrum analyzer to measure the amplitude of the scattered drive photons near the frequency of the microwave resonator. The per photon scattering rate is equal to the back-action induced damping rate of the mechanical resonator due to the presence of the pump. Calibrating out the gain of the measurement setup, the added noise of the amplifier and the read-out efficiency of the signal, the area under the observed signal in the spectrum analyzer is proportional to the occupancy of the mechanical resonator. A plot of the inferred mechanical mode occupancy versus the intra-cavity photon number is shown in Fig. 6.7. As we increase the

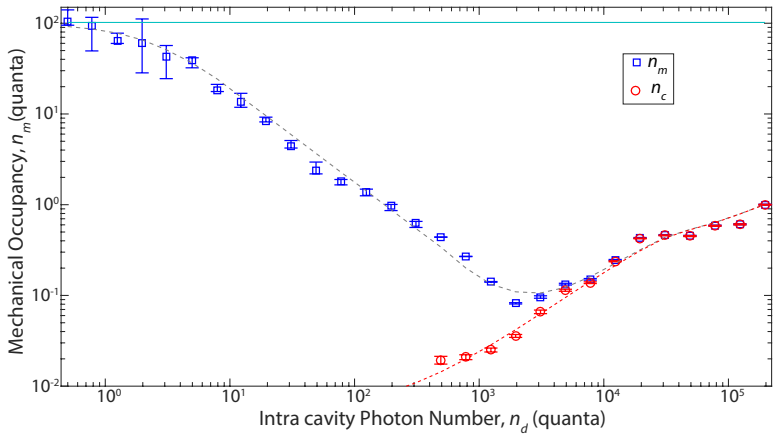

Figure 6.7: Plot of the inferred mechanical mode occupancy from a fit to the mechanical mode thermometry spectra n_m versus intra-cavity photon number n_d. The light blue line is mechanical mode bath occupancy of $n_{f,m} = 100$, corresponding to ambient temperature $T_{f,m} = 30$ mK. Blue squares correspond to inferred mechanical mode occupancy from the thermometry measurement and the dashed gray line shows the expected ideal cooling curve. The red circles are the inferred microwave resonator noise occupancy n_r and the red-dashed line is a polynomial fit to the data.

power of the red detuned pump, the rate of scattering photons into the microwave cavity increases which subsequently increases the cooling rate of the mechanical resonator. During this process the mechanical resonator is coupled to an ambient fridge bath $T_{f,m}$ with the intrinsic damping rate γ_i and effective zero temperature bath of the coherent drive pump with back-action induced damping rate of γ_{em}. In the steady state while we are operating below the strong coupling regime, the mechanical occupancy can simply be obtained by $n_m = n_{f,m}/(1 + C)$, where C is the cooperativity and is defined by γ_{em}/γ_i.

At low drive power where $C < 1$ the effect of the drive tone is negligible and the mechanical resonator is assumed to be thermalized to its ambient dilution fridge mechanical bath $n_{f,m}$. For the 'Nano-String' electromechanical resonator, the ambient mechanical bath is measured to be at $n_{f,m} = 100$ corresponding to the ambient fridge temperature of $T_{f,m} \approx 30$ mK. A dashed-gray line is used to show the expected cooling curve of the mechanical resonator versus the intra cavity

photon number n_d. For this curve, we use the independently verified parameters G, κ, γ_i. As it can be seen, the measured mechanical occupancy is in good agreement with the expected occupancy. At the highest drive powers we measure Lorentzian microwave cavity noise, which leads to noise squashing in the measured output spectrum and heating of the mechanical resonator [84]. To calculate the mechanical occupancy at these powers, we use the Eq. (3.31) derived in chapter 3.

Compared to the 'H-Slot' electromechanical resonator, with the improved single photon electromechanical coupling of $g_0/2\pi = 230$ Hz and the on the intrinsic microwave resonance loss rate, we are able to reach $C = 1$ at $n_d = 2$ photons and ground-state cooling at $n_d = 200$ photons. The minimum mechanical occupancy measured in this experiment is $n_m = 0.1$ phonons. However, at intra cavity photon number $n_d = 1000$ photons, we observe the anomalous pump induced heating effects increasing the microwave cavity noise occupancy.

6.5 Nano-String Electro-Opto-Mechanical Transducer

Our results with Nano-String electromechanical resonator indicates that SOI represents a unique platform for integrating microwave, mechanical and optical circuits. This is particularly interesting in the context of utilizing the mechanical elements as quantum converters between the electrical and optical photons. In this section, I talk about the design and fabrication of an integrated platform for converting optical photons and microwave photons which is based on the Nano-String design principles. The key aspect of this platform is the shared mechanical mode between the optical resonator and the microwave electrical circuit. The coupling between the microwave resonator and the mechanical element is capacitive (similar to Nano-String mechanical resonator) in which the deformation of the structure to mechanical motion modulates the capacitor gap and similarly the microwave resonance frequency. On the optical side, the motion of the mechanical resonator modulates the effective dielectric constant of the optical modes and subsequently modulates the optical resonance frequency. In the following subsection, I will talk about the main aspects of the design in more detail.

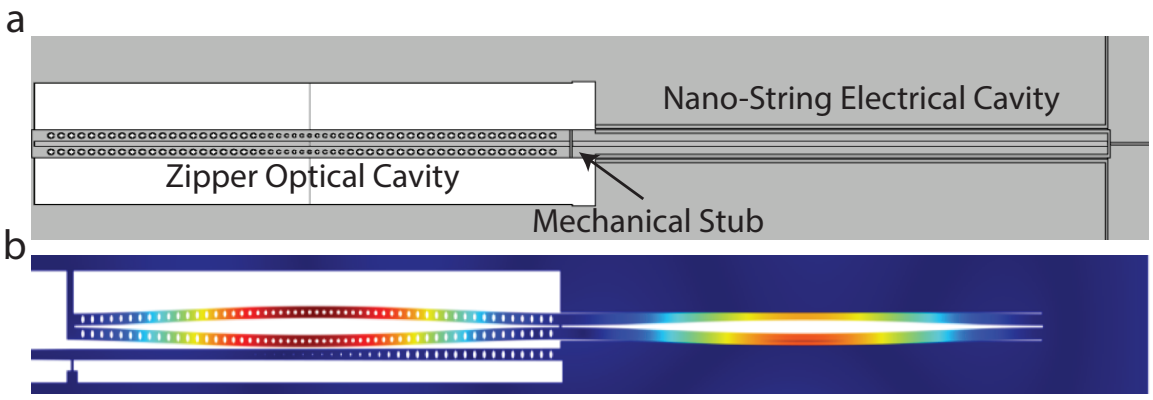

Figure 6.8: **a,** shows the schematics of the elements of the Nano-String Electro-Opto-Mechanical Transducer. On the left side the zipper optomechanical cavity is attached via a mechanical stub to an electromechanical Nano-String resonator. The Zipper optical cavity is patterned with circular holes with a defect to form an optical cavity at the center. The optical cavity has the length of $l_o = 19.5\ \mu$m and width of $W = 550$ nm resulting in a differential mechanical mode at 7.0 MHz. The length of the Nano-String electromechanical cavity is slightly larger at $l_e = 20.4\ \mu$m due to aluminum electrodes that cover the outer sides of the beams. The mechanical stub between the two sides couple the two mechanical modes. The coupling strength between the two sides can be adjusted by varying the width of the mechanical stub. With the chosen width of $w = 100$ nm the coupling between the two mechanical mode is approximately 1.09 MHz resulting in in mechanical frequency 8.09 MHz (5.91 MHz) for Even (Odd) mechanical modes. **b,** shows an exaggerated displacement deformation of the symmetric mechanical mode of the structure where the red(blue) color shows the area with maximum (minimum) displacements.

6.5.1 Mechanical Mode Design and Analysis

The Opto-Electro-Mechanical transducer consists of a doubly-clamped zipper optical cavity [112] which is connected by a mechanical stub to Nano-String electromechanical resonator and clamped at both ends. The length of the zipper optical cavity and Nano-String electromechanical resonator are chosen such that they result in a degenerate mechanical frequency for breathing (differential mode of each side) mode. In this situation, the mechanical mode of the zipper optical cavity and Nano-String electromechanical resonator will hybridize to form an even and odd symmetry mechanical modes that is shared with both the electrical circuit and the optical cavity. The strength of the coupling and consequently frequency splitting between the two mechanical modes can be adjusted by the width of the mechanical stub. The mechanical simulation of the structure is done by Finite-Element Method (FEM) using COMSOL Multiphysics software [54]. The even and odd hybridized mechanical modes are at 8.09 MHz and 5.91 MHz mechanical frequency and have zero point amplitudes of

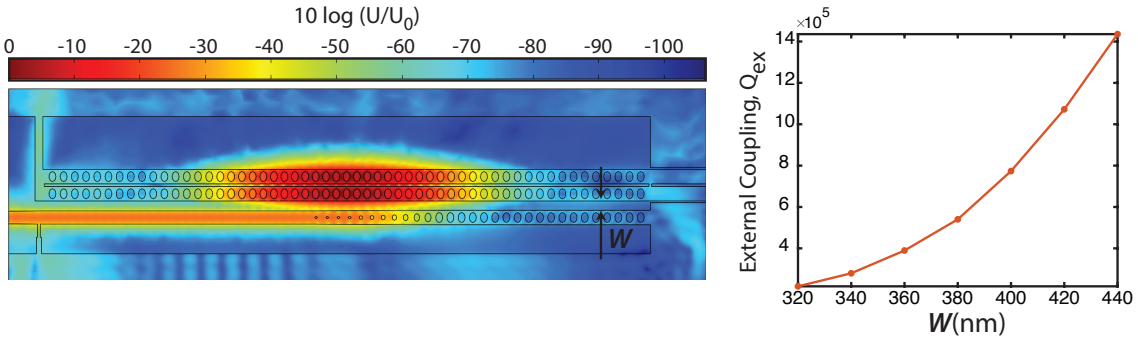

Figure 6.9: **a,** shows the schematics of the elements of the Nano-String Electro-Opto-Mechanical Transducer. On the left side the zipper optomechanical cavity is attached via a mechanical stub to an electromechanical Nano-String resonator. The Zipper optical cavity is patterned with circular holes with a defect to form an optical cavity at the center. The optical cavity has the length of $l_o = 19.5\ \mu$m and width of $W = 550$ nm resulting in a differential mechanical mode at 7.0 MHz. The length of the Nano-String electromechanical cavity is slightly larger at $l_e = 20.4\ \mu$m due to aluminum electrodes that cover the outer sides of the beams. The mechanical stub between the two sides couple the two mechanical modes. The coupling strength between the two sides can be adjusted by varying the width of the mechanical stub. With the chosen width of $w = 100$ nm the coupling between the two mechanical mode is approximately 1.09 MHz resulting in in mechanical frequency 8.09 MHz (5.91 MHz) for Even (Odd) mechanical modes. **b,** shows an exaggerated displacement deformation of the symmetric mechanical mode of the structure where the red (blue) color shows the area with maximum (minimum) displacements.

$x_{\text{zpf}} = 11.2, 14.2$ fm, respectively.

The aluminum electrodes on the outer edge of the Nano-String electromechanical resonator form a motional capacitance which is in parallel to a high impedance spiral inductor similar to Nano-String electromechanical resonator which would enables us to easily achieve electromechanical coupling on the order $g_{em}/2\pi = 100$ Hz. On the other hand, the patterning of the zipper optical cavity confines the optical fields at the center where the differential mode has the maximum displacement. With the relatively large refractive index of the silicon, vacuum optomechanical coupling on the order of $g_{om}/2\pi = 1$ MHz [113] are expected.

6.5.2 Design of the Optical Cavity and the Optical Coupler

As described, the zipper optomechanical cavity is patterned in such a way that supports an optical mode at 1550 nm wavelength band. The design of the optical cavity is identical to the device presented in Ref. [113]. The optical coupling to the device and read-out are done using an optical

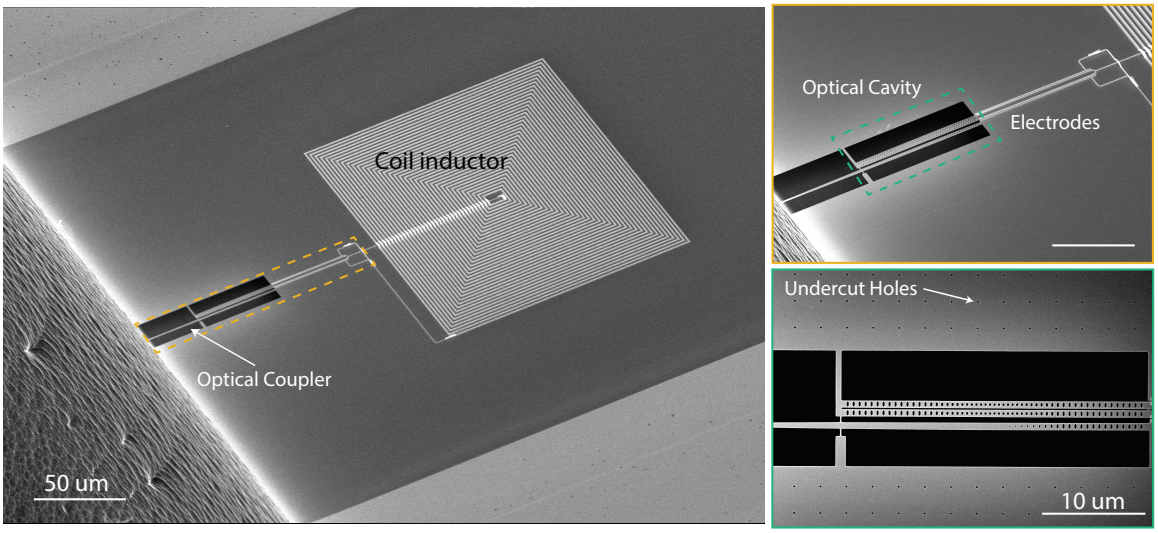

Figure 6.10: **a,** Show a zoom-out scanning electron microscope image of the device. A coil inductor is capacitively coupled to the Nano-String elctromechanical resonator which is mechanically coupled to a 'zipper' optomechanical cavity. The optical coupling to the device is done using a tapered optical coupler which terminates with highly reflective photonic crystal end-mirror. **b,** A zoomed-in version of the device showing the optomechanical cavity and the 'Nano-String' electromechanical resonator. The Al wires forming the motional capacitance are in white.**c)** A zoom-in SEM image of the optical cavity and the optical coupler.

waveguide placed on the side of the zipper optomechanical cavity.

FEM simulation of the optomechanical zipper cavity is plotted in Fig. 6.9(a). The color depicts the normalized electromagnetic energy density. The waveguide is terminated by highly reflective photonic crystal end mirror to excite and collect light efficiently from the side coupled optical cavity. Placing the waveguide in the near field of the optical cavity allows for evanescent coupling between the waveguide and the optomechanical cavity with the coupling strength of $\kappa_{e,o}$ and external quality factor $Q_{ex,o}$.

Tuning the separation of the optical waveguide from the optical cavity W, we can control the coupling strength. The optical coupler presented in this chapter is placed 370 nm away from the optical cavity resulting in $Q_{ex,o} = 520 \times 10^3$. The width of the waveguide is adiabatically tapered to allow for efficient input-output coupling to a lensed fiber, as shown in the SEM as described in Ref. [114].

6.5.3 Fabrication

Fabrication of the 'Nano-String' Electro-Opto-Mechanical transducer is done on the top device later of a SOI wafer as discussed in detail in chapter (5). Before releasing the Si membrane, we follow the processes described in Ref. [101] to define a mesa region of the chip to which a tapered lensed can access, as can be seen in the SEM of the device shown in Fig. 6.10(a).

6.5.4 Experimental Setup

The measurements of the fabricated SOI chip are performed in a dilution refrigerator down to a temperature of $T_f = 10$ mK. The sample is mounted on a printed circuit board (PCB) consisting of multiple $50 - \Omega$ coplanar waveguides. Each coplanar waveguide of the PCB is wire-bonded to another coplanar waveguide on the chip.

The coplanar waveguides are terminated by extending the center conductor with a 2 μm wide wire and then shorted to the ground. The wire is passed within the near field of the coil inductor, providing large inductive coupling of the strength $\kappa_{ex,e} = 100$ kHz to the electromechanical circuit. The input microwave signal is attenuated through each stage of the dilution refrigerator to eliminate Johnson thermal noise from the room temperature environment. The total calibrated attenuation of the measurement setup is $\mathcal{A} = 76.5$ dB. The reflected microwave signal is redirected using a pair of circulators at the mixing chamber of the dilution refrigerator and then sent to the amplifier chain with the total gain of $\mathcal{G} = 56.7$ dB. The amplified signal is then measured using a Vector Network Analyzer (VNA) or spectrum analyzer.

The PCB is mounted on a copper column assembly to allow for in-situ optical fiber coupling. We utilize an end-fire coupling scheme to probe the optomechanical 'zipper' cavity. The lensed fiber tip is clamped down on a position encoded piezo xyz-stage inside the dilution refrigerator allowing for nano-positioning of the fiber with respect to the sample. The lensed fiber used for this experiment has the focal length $l = 15$ μm and a beam waist of 2.5 μm.

At room temperature, we roughly align the fiber to within few hundred microns of the tip of the tip of the optical waveguide coupler. After cooling the experimental setup from the room temperature, we monitor the reflected optical power on a photo detector as we slowly move the fiber to match the height of the device layer. The distinct reflection of the device layer allows for iteratively

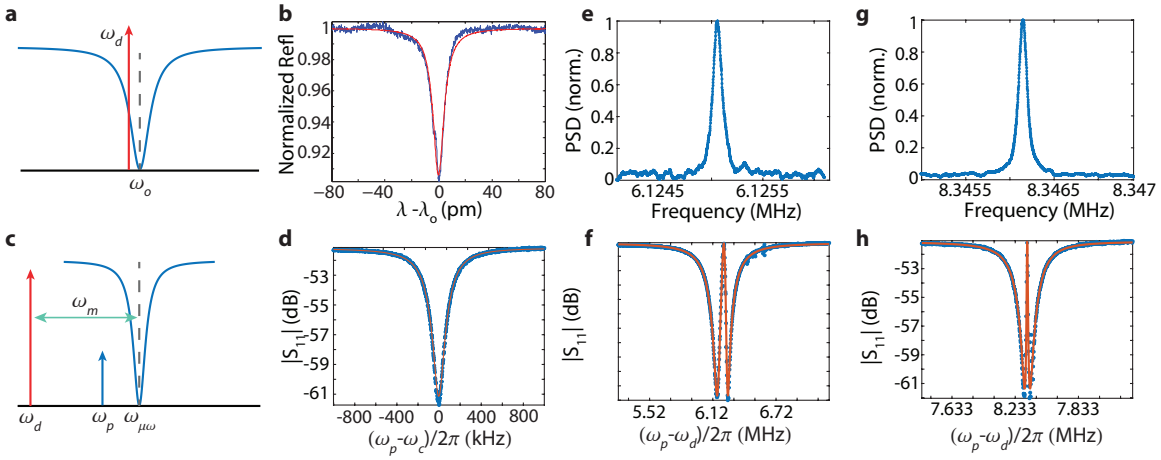

Figure 6.11: **a,** Shows a schematic of the optical measurement. A laser at frequency ω_d is scanned across the optical cavity. **b,** The normalized reflected spectrum of the optical cavity measured from a photodetector. The optical cavity is observed at a wavelength of 1537.6 nm and has quality factor $Q_o = 154 \times 10^3$. The coupling the optical cavity is $Q_{ex,o} = 6.4 \times 10^6$. **c,** shows a schematic of two-tone EIT measurement procedure from the electrical side of the transducer. A strong microwave drive tone at ω_d is placed on the red sideband of the microwave cavity and the cavity response is swept by weak VNA probe at ω_p **d,** The amplitude response of the microwave resonator. The cavity frequency, intrinsic loss rate $\kappa_{i,e}$ and external coupling rate $\kappa_{ex,e}$ are extracted by fitting the curve with Lorentzian cavity model. **e,** The mechanical response to the optical signal laser, through the reflected optical signal field as measured on the spectrum analyzer for the first mechanical mode at $\omega_m/2\pi = 6.1241$ MHz. **f,** The plot of EIT spectra as measured by VNA for the first mechanical mode. **g,** The mechanical response of the second mechanical mode to the optical field. The mechanical mode is observed at mechanical frequency $\omega_m/2\pi = 8.3463$ MHz. **h,** The plot of EIT spectra for the second mechanical mode of the structure

adjusting the fiber position and optimizing the coupling to the device.

6.5.5 Optical Characterization

The optical characterization of the our device is done by sweeping the laser frequency across the optical resonance (Fig. 6.11a) while detecting the reflected light in a photodetector. This light is simultaneously sent to a wavemeter to record the absolute wavelength and accurately determine the linewidth and the center frequency of the resonance. A spectrum of the optical cavity is shown in Fig. 6.11(b). For the device presented in this chapter, the optical cavity is observed at the wavelength of $\lambda_o = 1537.6$ nm and has the quality factor of $Q_o = 154 \times 10^3$. The coupling rate to the optical is $\kappa_{ex,o}/2\pi = 30.4$ MHz corresponding to external quality factor $Q_{ex,o} = 6.4 \times 10^6$.

6.5.6 Electrical Characterization

Similar to 'Nano-String' electromechanical resonator, coherent electrical response of the device is measured by sweeping a narrow band microwave source across the 6-12 GHz frequency range and measuring in reflection through the VNA (Fig. 6.11c). We find a high-Q microwave resonance at frequency $\omega_e/2\pi = 10.6645$ GHz. We fit a Lorentzian to the amplitude response of the microwave cavity and extract the external coupling $\kappa_{ex,e} = 94.6$ kHz and intrinsic loss rate of $\kappa_{i,e} = 101.1$ kHz.

6.5.7 Mechanical Characterization

The characterization of the mechanical modes are done independently from both the electrical and optical side.

Optical characterization of the mechanical motion is done by parking the optical probe laser detuned from the optical cavity and observing the transduction of the reflected optical fields using the photo-diode. In this scheme, the mechanical motion is imprinted as intensity modulations of the probe laser. Here, we choose the detuning point corresponding to $\Delta_L = \omega_L - \omega_o = \kappa_o/2\sqrt{3}$ where ω_L is the probe laser frequency. This detuning choice ensures (maximal) linear transduction of small fluctuations in the frequency of the optical cavity resonance and allows us to relate linear transduction of the motion to optomechanical coupling rate G_o. In this measurement, a probe power of $P_L = 200$ nW is used to avoid any nonlinear effects due to optical absorption and the reflected light is first amplified through an erbium-doped fiber amplifier (EDFA) before being detected on a high-gain photo-reciever. The resulting photo-current signal is sent to a spectrum analyzer. The FFT of the measured electrical signals for the mechanical modes are plotted in Fig. 6.11 (e,g). The mechanical modes are observed at frequency of $\omega_{m,1}/2\pi = 6.1241$ MHz and $\omega_{m,2}/2\pi = 8.3463$ MHz very close to the expected frequency from the FEM simulations.

The optomechanical coupling rates, G_o, are measured by the mechanical response to the signal laser. We keep the optical power constant at $P_L = 200$ nW, while we take measurements at several different detunings Δ_L. The radiation pressure force causes an optical spring effect, resulting in a frequency shift of the mechanical resonance [13] according to the equation :

$$\delta\omega_m = |G_o|^2 \mathbf{Im}\left[\frac{1}{i(\Delta_L - \omega_m) + \kappa_o/2} - \frac{1}{-i(\Delta_L + \omega_m) + \kappa_o/2}\right]. \tag{6.1}$$

By fitting the frequency shift of the mechanical resonances and calibrating the intra-cavity photon number due to the presence of the laser probe, we obtain single photon optomechanical coupling of $g_{0,o1} = 80.4$ kHz and $g_{0,o2} = 80.4$ kHz for the first mechanical mode at 6.1241 MHz and second mechanical mode at 8.3463 MHz mechanical modes respectively.

We use the two tone pump-probe scheme to study the coherent interaction between the microwave electrical circuit and the coupled mechanical resonator. Using the same method as in section (6.4.1), we use weak probe tone across the microwave cavity while stepping a strong pump drive red detuned from the cavity to accurately measure the mechanical frequency. When the detuning from the microwave matches the mechanical frequency, the circuit produces a two-photon resonance condition with the weak probe tone as it is swept across the microwave resonance. Interference in the reflected probe signal occurs between the photon that is reflected directly from the microwave cavity and the photon that interacts with the mechanical resonator and is re-emitted from the cavity. Figure 6.11(f,h) shows the plot of the coherent response of the electromechanical circuit when the detuning from the cavity are 6.1241 MHz and 8.3463 MHz, respectively, indicating the coupling to the same mechanical mode as the zipper optomechanical cavity.

To extract the parametrically enhanced electromechanical coupling, we fit the coherent response of the cavity with the Eq. (3.24). Repeating the same measurement for various powers of the drive tone allows us to extract the vacuum electro-mechanical coupling $g_{0,e}$ for each mechanical mode and is found to be $g_{0,e1} = 100$ Hz and $g_{0,e2} = 87$ Hz for the first and the second mechanical mode of the transducer.

6.5.8 Effect of Optical Light on the Superconducting Microwave Circuit

The integration of an electromechanical and optomechanical circuit place us in a unique position to study the effects of the optical light on the superconducting microwave circuit. In this measurement, the optical laser is on resonance with optical cavity while we scan the superconducting microwave resonator with a weak probe through VNA.

Figure 6.12(a), shows the coherent response of the microwave cavity as measured with and without the presence of the optical light. The microwave loss rate increases greatly with the presence of optical light even with optical small laser powers down at 100 nW. The mechanism can be in-

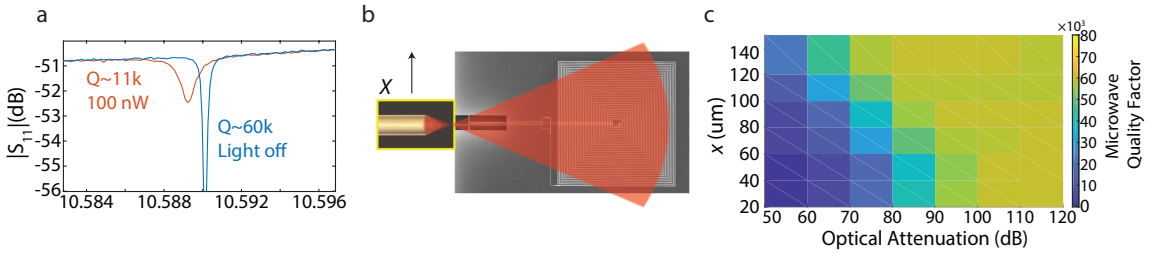

Figure 6.12: **a,** The electrical response of microwave cavity with and without the presence of optical light. In this measurement, the fiber is coupled to optical waveguide and the laser is on resonance with the optical cavity. With 100 nW of optical power at the sample input, the microwave quality factor degrades by a facor of 5. **b,** Diagram showing the positioning of the lensed optical fiber (not to scale) with respect to the superconducting electromechanical circuit. The red region showing the scattered photon from the optical fiber. **c,** A color plot of the microwave resonator quality factor versus the vertical distance of the fiber from the optical waveguide and the optical power.

tuitively understood in that each optical photons incident on the superconducting aluminum wires have enough energy to locally break the cooper pairs. This results in a formation of locally non-superconducting region which consequently increases the loss rate and shifts the frequency of the microwave cavity resonance. The sources of these scattered photons can be either through the leakage from the optomechanical cavity and the tapered optical waveguide or the light directly scattered from the fiber. To identify the source of the parasitic incident light, we moved the fiber laterally away from the waveguide, while measuring the quality factor of the microwave resonator as a function of the displacement and the optical power (see Fig. 6.12(b)). The results of this measurement are shown in Fig. 6.12(c), indicating a weak dependence on the lateral distance of the fiber from the optical waveguide. This result indicates that the scattered light from the optical fiber are the main source for the loss rate of the microwave circuit, since the optical coupling to the waveguide drops rapidly when the lateral distance becomes more than the beam waist of the optical beam, which conforms to the result of the FEM simulation shown in Fig. 6.9(a).

Chapter 7

High-Frequency Mechanics on Silicon on Insulator

7.1 Introduction

So far we have demonstrated superconducting microwave resonators employing nanoscale vacuum-gap capacitors and reaching vacuum coupling levels as large as a few hundred Hz to MHz-frequency mechanical oscillators. These devices have been utilized for a variety of applications ranging from conversion between microwave and optical photons [27, 30] to the generation and detection of squeezed states of mechanical motion [19, 90, 91]

Similar work in the optical domain has sought to increase the radiation pressure within optical resonators by scaling the optical mode volume down to the nanoscale [82]. An example of this is the optomechanical crystal (OMC) [97], in which optical and acoustic fields are co-localized at the wavelength scale due to Bragg scattering in a periodically patterned host material, and vacuum coupling rates of $g_0 \sim 1$ MHz between near-infrared photons and X-band microwave phonons has been realized. Owing to the factor of $\sim 10^5$ between the speed of light and sound in solid-state materials, optical photons and microwave phonons are matched in wavelength, enabling the construction of integrated photonic and phononic circuits which can be used to route signals around on a chip or to inter-convert optical and acoustic waves [115–118]. For quantum applications, high frequency microwave acoustic devices also have several advantages; lower thermal excitation levels and lack of fringing fields in vacuum reduce decoherence and cross-talk. For these reasons, the integration of Josephson-junction based superconducting quantum circuits [119] and microwave acoustic devices is actively being explored [120–128].

A significant challenge in this effort is to obtain large, decoherence-free motional coupling. The use of piezoelectric materials [129], as in wireless communication systems [130], can enable MHz-rate coupling levels suitable for quantum information processing [115, 124–128, 131, 132]. The piezoelectric coupling, however, cannot be turned off nor is it perfectly mode selective, and polycrystalline piezoelectric materials can harbor lossy defects [133]. Both these effects can lead to parasitic electrical or acoustic damping and decoherence. Parametric radiation pressure coupling can be dynamically controlled and can avoid some materials issues as it is relatively materials agnostic, but it is challenging to reach the requisite level of coupling due to the large mismatch in microwave electromagnetic and acoustic wavelengths. Using an aluminum (Al) on silicon-on-insulator (SOI) process which has been effective in forming low-loss superconducting quantum circuits [134], here we demonstrate an electromechanical resonator that utilizes hypersound frequency ($\gtrsim$ GHz) [135] phononic crystals to engineer the localization and parametric coupling of mechanical motion at $\omega_m/2\pi = 0.425$ GHz to an integrated superconducting microwave high impedance circuit. This electromechanical crystal (EMC) structure, akin to the optical OMCs, achieves simultaneously the large photon-phonon coupling ($g_0/2\pi = 17.3$ Hz) and minimal acoustic damping ($\gamma_{m,i}/2\pi = 68$ Hz) required of quantum electromechanics applications.

7.2 Design

The electromechanical crystal studied in this work is formed from superconducting Al wiring on a patterned sub-micron thick silicon (Si) membrane, and consists of three primary elements: (i) a central nanobeam phononic crystal cavity and capacitor with nanoscale vacuum gap, (ii) an acoustic shield with a phononic bandgap for all polarizations and propagation directions of acoustic waves, and (iii) a nanoscale-pitch spiral coil inductor with minimal stray capacitance and large intrinsic impedance.

7.2.1 Electromechanical Crystal Design

Here we focus on the design of the nanobeam cavity. Figure 7.1(a) depicts the patterned nanobeam cavity geometry and Al wiring layout of the vacuum-gap capacitor. The resulting hypersonic ‘breathing’ acoustic cavity mode is also shown, visualized as an exaggerated deformation of the beam struc-

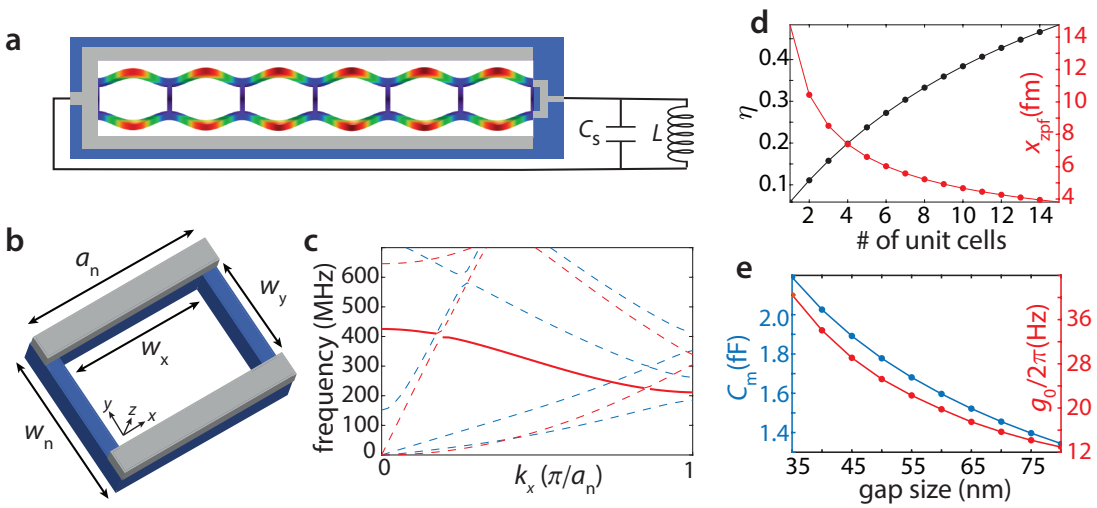

Figure 7.1: **a**, Schematic of the central nanobeam region showing the breathing mode. Mechanical motion is indicated by an exaggerated displacement of the beam structure, with red (blue) color indicating regions of large (small) amplitude of the motion. The Al capacitor electrodes (grey) are connected in parallel to a coil inductor of inductance L and parasitic capacitance C_s. **b**, Unit cell of the nanobeam phononic crystal lattice with Si device layer (Al electrode) shown as blue (grey). **c**, Acoustic band structure for an infinitely periodic nanobeam phononic crystal with parameters: $a_n = 1.55$ μm, $W_n = 900$ nm, $W_x = 600$ nm and $W_y = 1.45$ μm. The Si device layer and Al electrode thicknesses are $t_{\mathrm{Si}} = 220$ nm and $t_{\mathrm{Al}} = 60$ nm, respectively. The red and blue curves correspond to symmetric and antisymmetric modes with respect to the x-z symmetry plane. The band from which the breathing mode is formed is shown as a solid red curve. **d**, Participation ratio (η) and zero-point motion amplitude (x_{zpf}) of the breathing mode as a function of number of unit cells in the beam for a fixed parasitic capacitance $C_s = 3.1$ fF and a vacuum gap size of 45 nm. **e**, Motional capacitance, C_m, and zero-point coupling, g_0, of the electrical circuit as a function of the gap size. Here the coil inductance, L, is adjusted for each gap to keep the LC-resonance frequency fixed at $\omega_{r,0} = 10.77$ GHz.

ture. Referring to the nanobeam unit cell and acoustic bandstructure of Figs. 7.1(b-c), this breathing mode is formed from an acoustic band (solid bold red curve) near the Γ-point at wavevector $k_x = 0$. For a lattice constant of $a_n = 1.55$ μm, beam width of $W_n = 600$ nm, silicon membrane thickness $t_{\mathrm{Si}} = 220$ nm and Al wire thickness $t_{\mathrm{Al}} = 60$ nm, numerical finite-element method (FEM) simulations place the Γ-point frequency of the breathing mode band at $\omega_m/2\pi = 0.425$ GHz. Although other acoustic bands (dashed curves) are also present, the relative isolation of the breathing Γ-point modes in reciprocal space still allows for the formation of highly localized cavity modes near the band-edge. Several subtle features of the nanobeam design are key to realizing large electromechanical coupling, the magnitude of which is given by [136],

$$g_0 = -\eta x_{\text{zpf}} \frac{\omega_{r,0}}{2C_m} \frac{\partial C_m}{\partial u}, \tag{7.1}$$

where $\omega_{r,0}$ is the resonance frequency of the coupled LC circuit, u is the displacement amplitude of the acoustic mode of interest, x_{zpf} is the zero-point amplitude of this mode, and C_m is the vacuum-gap capacitance affected by the beams motion. η is a motional participation ratio defined by $\eta = C_m/C_{\text{tot}}$, where C_s is the stray and $C_{\text{tot}} = C_s + C_m$ the total capacitance of the LC circuit. Firstly, a minimum motional mass (m_{eff}) is desired to increase the zero-point amplitude ($x_{\text{zpf}} = [\hbar/2m_{\text{eff}}\omega_m]^{1/2}$). In the case of the patterned nanobeam this corresponds to minimizing the thickness of the Si and Al layers and minimizing the width of the beam features. Secondly, a large participation ratio is desired in the presence of minimum realizable stray capacitance. Owing to the use of a Γ-point acoustic mode the electromechanical coupling from each unit cell is additive and increasing the number of unit cells in the acoustic cavity results in an increased motional capacitance and participation ratio. FEM simulations of x_{zpf} and η versus the number of nanobeam unit cells are shown in Fig. 7.1(d) for a stray capacitance $C_s = 3.1$ fF and a fixed vacuum gap $s = 45$ nm. Here, C_s is dominated by the stray capacitance of the planar spiral coil inductor forming the LC resonator. Figure 7.1(e) shows the resulting simulated vacuum coupling rate versus gap size of the breathing mode for a nanobeam structure consisting of 11 unit cells. Beyond 11 unit cells we find the acoustic mode becomes too sensitive to disorder, and tends to breaks up into localized resonances when fabricated.

7.2.2 Phononic Bandgap Acoustic Shield

As mentioned above, the nanobeam phononic crystal does not have a full phononic bandgap in the vicinity of the breathing mode. In order to provide additional acoustic isolation from the surrounding Si membrane and substrate the nanobeam cavity and vacuum-gap capacitor are embedded in the middle of a 'cross-pattern' phononic bandgap crystal [137]. A unit cell of the cross shield, shown in Fig. 7.2(a), consists of a large square plate region with four narrow connecting tethers. Through adjustment in the width of the square plate, and length and width of the connecting tethers, a substantial bandgap can be opened up between the low frequency tether modes and the localized modes of each

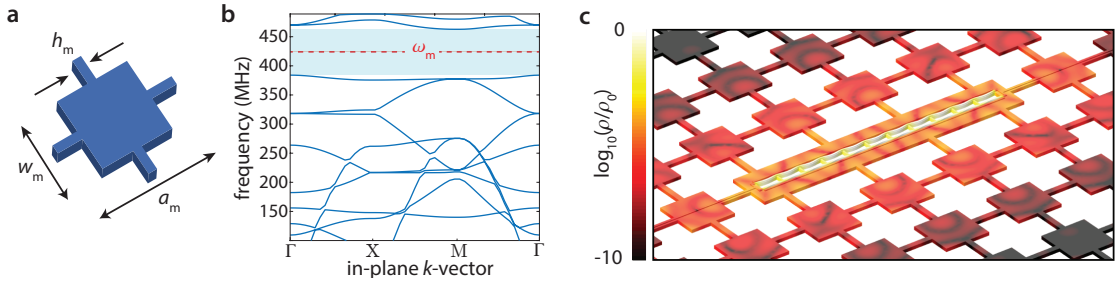

Figure 7.2: **a**, Schematic and dimensions of a unit cell in the phononic crystal shield (mirror cell) surrounding the nanobeam central cavity. **b**, Acoustic band structure of the acoustic shield for mirror unit cell parameters: $a_m = 5.13$ μm, $W_m = 2.1$ μm, $=$ 360 nm and $t_{\mathrm{Si}} = 220$ nm. The acoustic band gap is shaded in blue and the localized breathing mode frequency is marked with a dashed red line. **c**, Logarithmic scale color plot of the acoustic energy density for the nanobeam breathing of (a) embedded in the acoustic shield of (b). Acoustic energy density, ρ, is normalized to its peak value, ρ_0, located in the nanobeam. Displacement of the structure is also used to visualize the breathing mode profile.

square plate. A FEM-simulated acoustic bandstructure of an optimized cross structure is shown in Fig. 7.2(b), where a bandgap of nearly 0.1 GHz around the breathing mode frequency of 0.425 GHz is obtained. Embedding the nanobeam phononic crystal cavity in the middle of a cross phononic crystal, Fig. 7.2(c) shows a simulation of the resulting radiation pattern of the localized breathing mode. As can be clearly seen, the energy density of the breathing mode reduces dramatically upon entering the acoustic shield, dropping by 10 orders of magnitude in only a few periods.

7.2.3 Mechanical-Q Simulation

Periodic structures can be made to have a phononic band gap where mechanical energy loss by linear elastic coupling to the environment can be made arbitrary small. To prevent the radiation of the mechanical energy to the surrounding substrate we first have to minimize the interaction of the mechanical resonator (here electromechanical nanobeam) to its surrounding substrate. Lack of the mechanical band gap for the mechanical mode means that the localized mechanical mode of the beam can couple with propagating modes of equal frequency due to imperfections in the structure that can cause acoustic scattering and break the beam symmetry. Additionally, there are always "body modes" of the membrane which purely exist because of the boundary condition of the membrane (and thus are not captured by the band-structure). If the exterior boundary of the membrane allows for the energy in the propagating and body modes to be lost, the modes that couple to the

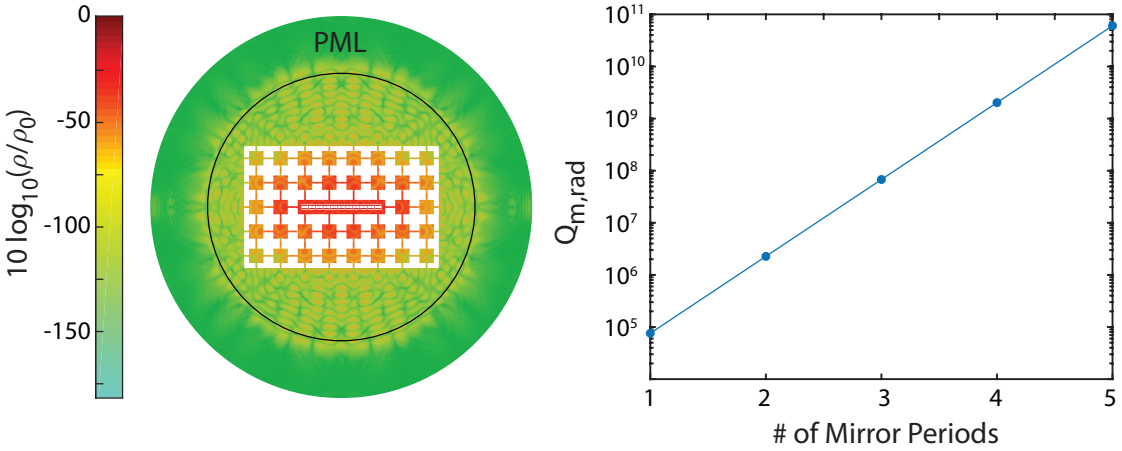

Figure 7.3: **a,** FEM Simulation of the mechanical beam resonator surrounded by 2 period phononic band gap structure, silicon membrane and a perfectly matched layer (PML). Color indicated the normalized mechanical energy density with red (green) color indicating the areas with highest (lowest) mechanical energy density. **b,** Simulated radiational mechanical quality factor versus the number of the periods of the phononic band gap shield.

localized mechanical mode will act as a parasitic loss channel for the localized mode. To prevent and minimize the interaction of the localized mechanical mode of the beam with the surrounding silicon membrane, we have embedded our mechanical beam resonator in a phononic band gap structures with 5 periods (see Fig. 7.2). To model the mechanical damping of the localized 'breathing' mode due to acoustic radiation we include a large circular "pad" around the structure which is a domain that should absorb all the outgoing acoustic waves. This domain is called a perfectly matched layer (PML). What distinguishes a PML domain from an ordinary absorbing/lossy material is that all the waves incident upon the PML from a non-PML media do not reflect at the interface, hence the PML strongly absorbs all outgoing waves from the interior of the computational region. An example of the FEM simulation is shown in Fig. 7.3a. In this image the nanobeam acoustic resonator and a 2 period phononic shield are surrounded by an inner circular membrane of normal Si material and outer, larger circular PML domain also made of Si. The color indicates the normalized acoustic energy density of the breathing mode throughout the structure. As shown, with using just 2 periods for the phononic shield, the radiated mechanical energy density is suppressed by $\approx$ 100 dB. Fig. 7.3b shows the simulated radiation-limited quality factors of the breathing mode of the mechanical resonator versus the number of phononic shield periods surrounding the mechan-

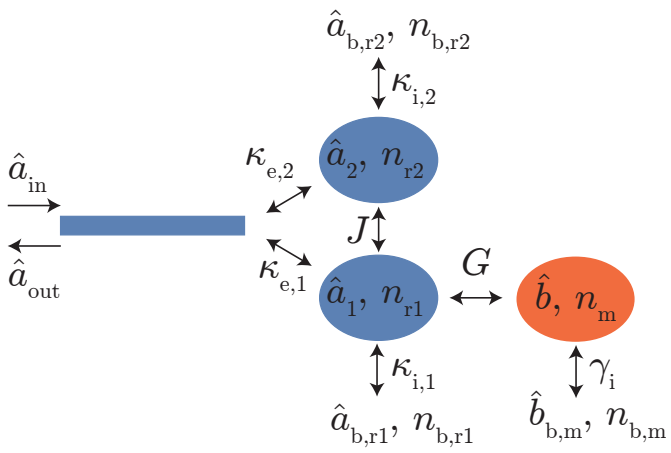

Figure 7.4: In the reflective geometry the microwave cavity mode $\hat{a}_1(\hat{a}_2)$ is coupled to the coherent waveguide modes $\hat{a}_{\mathrm{in}}$ and $\hat{a}_{\mathrm{out}}$ with the external coupling strength $\kappa_{e,1}(\kappa_{e,2})$. It is also coupled to a bath of noise photons, ideally at the refrigerator temperature $n_{b,r1}(n_{b,r2})$, with the intrinsic coupling strength $\kappa_{i,1}(\kappa_{i,1})$. The mechanical resonator mode $\hat{b}$ is coupled to the microwave resonator with the parametrically enhanced electromechanical coupling strength G. In addition, it is coupled to a bath of noise phonons, ideally at the refrigerator temperature $n_{m,\mathrm{bath}}$, with the intrinsic coupling rate $\gamma_{m,i}$.

ical nanobeam. All the finite element method simulations of the mechanical nanobeam are done using COMSOL Multiphysics [54]. The mechanical simulation use the full anisotropic elasticity matrix where $(C_{11}, C_{12}, C_{44}) = (166, 64, 80)$ GPa and assumes a [100] crystalline orientation for the x-axis (direction along the length of the nanobeam).

7.3 Derivation of two-mode electromechanical response

A final design consideration relates to the large hypersound frequency of the breathing mode. Coupling this mode to a microwave circuit of comparable frequency introduces a large effective detuning in the parametric interaction, greatly increasing the required microwave pump power. We circumvent this problem by using a multimode microwave cavity [85] consisting of two coupled single-mode LC resonators. In this scheme, one of the electromagnetic modes is resonant with the microwave pump tone, while the second mode is detuned by the acoustic mode frequency.

We follow previous work [21, 70–72, 85, 136] to calculate coherent response and full noise spectrum of the electromechanical system.

7.3.1 System Hamiltonian of two-mode microwave electromechanical system

The Hamiltonian of the coupled microwave electromechanical system (see Fig. 7.4) can be written as

$$\hat{H} = \hbar\omega_{r,0}\hat{a}_1^\dagger\hat{a}_1 + \hbar\omega_{r,0}\hat{a}_2^\dagger\hat{a}_2 + \hbar J(\hat{a}_1^\dagger\hat{a}_2 + \hat{a}_2^\dagger\hat{a}_1) + \hbar\omega_m\hat{b}^\dagger\hat{b} + \hbar g_0\hat{a}_1^\dagger\hat{a}_1(\hat{b}^\dagger + \hat{b}), \tag{7.2}$$

where $\hat{a}_j(\hat{a}_j^\dagger)$ are the annihilation (creation) operator of the bare microwave cavity modes with bare frequency $\omega_{r,0}$, $\hat{b}(\hat{b}^\dagger)$ are the annihilation (creation) operator of the mechanical mode, J is the coupling between the two microwave cavity, and g_0 is the single photon coupling between the microwave cavity 1 and the mechanical mode. We diagonalize the hamiltonian by introducing the even and odd superposition of the microwave cavity modes of the form $\hat{a}_\pm = \frac{\hat{a}1 \pm \hat{a}2}{\sqrt{2}}$.

The new Hamiltonian is now written as

$$\hat{H}' = \hbar\omega_{r,+}\hat{a}_+^\dagger\hat{a}_+ + \hbar\omega_{r,-}\hat{a}_-^\dagger\hat{a}_- + \hbar\omega_m\hat{b}^\dagger\hat{b} + \hbar\frac{g_0}{2}(\hat{a}_+^\dagger\hat{a}_- + \hat{a}_-^\dagger\hat{a}_+ + \hat{a}_+^\dagger\hat{a}_+ + \hat{a}_-^\dagger\hat{a}_-)(\hat{b}^\dagger + \hat{b}), \tag{7.3}$$

where the new supermode frequencies are $\omega_\pm = \omega_{r,0} \pm J$. We excite the microwave resonators by using a strong coherent drive at frequency ω_d detuned from the microwave resonators frequency by $\Delta_{r\pm,d} = \omega_{r\pm} - \omega_d$. Thus we can write the hamiltonian in the rotating frame

$$\hat{\tilde{H}} = -\hbar\Delta_{r+,d}\hat{a}_+^\dagger\hat{a}_+ - \hbar\Delta_{r-,d}\hat{a}_-^\dagger\hat{a}_- + \hbar\omega_m\hat{b}^\dagger\hat{b} + \hbar\frac{g_0}{2}(\hat{a}_+^\dagger\hat{a}_- + \hat{a}_-^\dagger\hat{a}_+ + \hat{a}_+^\dagger\hat{a}_+ + \hat{a}_-^\dagger\hat{a}_-)(\hat{b}^\dagger + \hat{b}). \tag{7.4}$$

Assuming a strong red detuned drive from the higher frequency microwave cavity and $\Delta_{r+,d} \approx \omega_m \gg \Delta_{r-,d}$ we can linearize the hamiltonian in the rotating frame to obtain

$$\hat{\tilde{H}} = -\hbar\Delta_{r+,d}\hat{a}_+^\dagger\hat{a}_+ - \hbar\Delta_{r-,d}\hat{a}_-^\dagger\hat{a}_- + \hbar\omega_m\hat{b}^\dagger\hat{b} + \hbar G(\hat{a}_- + \hat{a}_-^\dagger + \hat{a}_+^\dagger + \hat{a}_+)(\hat{b}^\dagger + \hat{b}), \tag{7.5}$$

where $G = \frac{g_0}{2}\sqrt{n_{d,-}}$ and $n_{d,-}$ corresponds to intra-cavity photon number of the lower frequency microwave cavity defined by

$$n_{d,-} = \frac{P_d}{\hbar\omega_d}\frac{4\kappa_{e,-}}{\kappa_-^2 + 4\Delta_{r-,d}^2}, \tag{7.6}$$

where P_d is the power at the cavity input, expressed by $P_d = 10^{-3}10^{(\mathcal{A}+P_{in})/10}$ with P_{in} the drive

power in dBm and $\mathcal{A}$ the total attenuation of the input line in dB. For the Hamiltonian in Eq. (7.5), the linearized Langevin equations are given as

$$\dot{\hat{a}}_-(t) = -\left(i\Delta_{r-,d} + \frac{\kappa_-}{2}\right)\hat{a}_-(t) - iG(\hat{b}(t) + \hat{b}^\dagger(t)) - \sqrt{\kappa_{e,-}}\hat{a}_{\text{in}}(t) - \sqrt{\kappa_{i,-}}\hat{a}_{r-,b}(t), \quad (7.7)$$

$$\dot{\hat{a}}_+(t) = -\left(i\Delta_{r+,d} + \frac{\kappa_+}{2}\right)\hat{a}_+(t) - iG(\hat{b}(t) + \hat{b}^\dagger(t)) - \sqrt{\kappa_{e,+}}\hat{a}_{\text{in}}(t) - \sqrt{\kappa_{i,+}}\hat{a}_{r+,b}(t), \quad (7.8)$$

$$\dot{\hat{b}}(t) = -\left(i\omega_m + \frac{\gamma_{m,i}}{2}\right) - iG(\hat{a}_+(t) + \hat{a}_-^\dagger(t)) - \sqrt{\gamma_{m,i}}\hat{b}_{b,m}(t). \quad (7.9)$$

Here, $\hat{a}_{b,r\pm}$ are annihilation operators of the microwave baths coupled to the even and odd microwave cavities. Now, taking the Fourier transform of the linearized Langevin equations and simplifying we obtain

$$\chi_{r-}^{-1}(\omega)\hat{a}_-(\omega) = -iG(\hat{b}(\omega) + \hat{b}^\dagger(\omega)) - \sqrt{\kappa_{e,-}}\hat{a}_{\text{in}}(\omega) - \sqrt{\kappa_{i,-}}\hat{a}_{r-,b}(\omega), \quad (7.10)$$

$$\chi_{r+}^{-1}(\omega)\hat{a}_+(\omega) = -iG(\hat{b}(\omega) + \hat{b}^\dagger(\omega)) - \sqrt{\kappa_{e,+}}\hat{a}_{\text{in}}(\omega) - \sqrt{\kappa_{i,+}}\hat{a}_{r+,b}(\omega), \quad (7.11)$$

$$\chi_{\text{m}}^{-1}(\omega)\hat{b}(\omega) = -iG(\hat{a}_-(\omega) + \hat{a}_-^\dagger(\omega) + \hat{a}_+(\omega) + \hat{a}_+^\dagger(\omega)) - \sqrt{\gamma_{m,i}}\hat{b}_{b,m}(\omega), \quad (7.12)$$

where $\chi_{r\pm}$ and χ_{m} are the uncoupled susceptibilities of microwave cavities and mechanics defined by

$$\chi_{r\pm}^{-1}(\omega) = \kappa_\pm/2 + i(\Delta_{r\pm,d} - \omega), \quad (7.13)$$

$$\chi_{\text{m}}^{-1}(\omega) = \gamma_{m,i}/2 + i(\omega_m - \omega). \quad (7.14)$$

In the sideband-resolved limit $\omega_m \gg \kappa_\pm, G$ and for positive detuning of the drive tone with respect to the high frequency microwave cavity $\Delta_{r+,d} \approx \omega_m$(red side pumping), we have $\chi_{\text{m}}\chi_{r-} \ll \chi_{\text{m}}\chi_{r+}$. Thus the linearized Langevin equation can be simplified further and written approximately

as

$$\hat{a}_+(\omega) = \frac{iG\chi_{r+}\chi_{\rm m}\sqrt{\gamma_{m,i}}\hat{b}_{b,m}(\omega) - \chi_{r+}(\sqrt{\kappa_{e,+}}\hat{a}_{\rm in}(\omega) + \sqrt{\kappa_{i,+}}\hat{a}_{r+,b}(\omega))}{1 + G^2\chi_{r+}\chi_{\rm m}} \tag{7.15}$$

$$\hat{a}_-(\omega) = -\chi_{r-}(\sqrt{\kappa_{e,-}}\hat{a}_{\rm in}(\omega) + \sqrt{\kappa_{i,-}}\hat{a}_{r-,b}(\omega)), \tag{7.16}$$

$$\hat{b}(\omega) = \frac{-\chi_{\rm m}\sqrt{\gamma_{m,i}}\hat{b}_{b,m}(\omega) - iG\chi_{\rm m}\chi_{r+}(\sqrt{\kappa_{e,+}}\hat{a}_{\rm in}(\omega) + \sqrt{\kappa_{i,+}}\hat{a}_{r+,b}(\omega))}{1 + G^2\chi_{r+}\chi_{\rm m}}, \tag{7.17}$$

where we have dropped the terms proportional $\chi_{\rm m}\chi_{r-}$. Since the mechanical transduction of the microwave signal is now observable for even mode microwave cavity, from here on we only focus on response from the even mode microwave cavity. Using the Input-Output formalism and Eq. (7.15) we get

$$\begin{aligned}\hat{a}_{\rm out}(\omega) &= \hat{a}_{\rm in}(\omega) + \sqrt{\kappa_{e,+}}\hat{a}_+(\omega), \\ &= \hat{a}_{\rm in}(\omega) - \kappa_{e,+}\frac{\chi_{r+}\hat{a}_{\rm in}(\omega)}{1 + G^2\chi_{\rm m}\chi_{r+}} - \frac{\sqrt{\kappa_{e,+}\kappa_{i,+}}\chi_{r+}\hat{a}_{r+,b}(\omega)}{1 + G^2\chi_{\rm m}\chi_{r+}} + \hat{b}_{b,m}(\omega)\frac{iG\sqrt{\kappa_{e,+}\gamma_{m,i}}\chi_{\rm m}\chi_{r+}}{1 + G^2\chi_{\rm m}\chi_{r+}}.\end{aligned} \tag{7.18}$$

7.3.1.1 Electromagnetically Induced Transparency

We first calculate the coherent part of the output signal by using Eq. (7.18) and dropping the incoherent terms to get

$$S_{11} = \frac{\langle\hat{a}_{\rm out}(\omega)\rangle}{\langle\hat{a}_{\rm in}(\omega)\rangle} = 1 - \frac{\kappa_{e,+}\chi_{r+}}{1 + G^2\chi_{\rm m}\chi_{r+}}, \tag{7.19}$$

and substituting for the bare microwave and mechanical cavity susceptibilities we get the coherent electromechanical analogue of the electromagnetic induced transparency valid for small probe powers,

$$S_{11} = 1 - \frac{\kappa_{e,+}}{\kappa_+/2 + i(\Delta_{r+,d} - \omega) + \frac{G^2}{\gamma_{m,i}/2 + i(\omega_m - \omega)}}. \tag{7.20}$$

7.3.1.2 Quantum derivation of observed noise spectra

To calculate the incoherent noise spectra of the mechanical resonator we write calculate the autocorrelation of the detected normalized field amplitude (or the photo current) $\hat{I}(t) = \hat{a}_{\rm out}(t) + \hat{a}^\dagger_{\rm out}(t)$,

$$S_{II} = \int_{-\infty}^{+\infty} d\omega' \left\langle \left(\hat{a}_{\rm out}(\omega) + \hat{a}^\dagger_{\rm out}(\omega)\right)\left(\hat{a}_{\rm out}(\omega') + \hat{a}^\dagger_{\rm out}(\omega')\right)\right\rangle. \tag{7.21}$$

Substituting for $\hat{a}_{\text{out}}(\omega)$ and $\hat{a}^{\dagger}_{\text{out}}(\omega)$ from Eq. (7.18) and using thermal noise correlation for input noise terms (*i.e.* $\langle \hat{b}_{b,m}(\omega)\hat{b}^{\dagger}_{b,m}(\omega')\rangle = (n_{m,\text{bath}}+1)\delta(\omega+\omega')$, $\langle \hat{b}^{\dagger}_{b,m}(\omega)\hat{b}_{b,m}(\omega')\rangle = n_{m,\text{bath}}\delta(\omega+\omega')$, $\langle \hat{a}_{r+,b}(\omega)\hat{a}^{\dagger}_{r+,b}(\omega')\rangle = (n_{b,r+}+1)\delta(\omega+\omega')$, $\langle \hat{a}^{\dagger}_{r+,b}(\omega)\hat{a}_{r+,b}(\omega')\rangle = n_{b,r+}\delta(\omega+\omega')$, $\langle \hat{a}_{\text{in}}(\omega)\hat{a}^{\dagger}_{\text{in}}(\omega')\rangle = \delta(\omega+\omega')$), the power spectral density is

$$S_{II}(\omega) = \left|\left(1-\frac{\kappa_{e,+}\chi_{r+}}{1+G^2\chi_{\text{m}}\chi_{r+}}\right)\right|^2 + (n_{b,r+}+1)\frac{\kappa_{e,+}\kappa_{i,+}|\chi_{r+}|^2}{|1+G^2\chi_{\text{m}}\chi_{r+}|^2} + (n_{m,\text{bath}}+1)\frac{\kappa_{e,+}\gamma_{m,i}G^2|\chi_{\text{m}}|^2|\chi_{r+}|^2}{|1+G^2\chi_{\text{m}}\chi_{r+}|^2}. \tag{7.22}$$

The mechanical occupancy can also be calculated by using Eq. (7.15) and Eq. (7.17) as in Ref. [71]

$$n_m = n_{m,\text{bath}}\left(\frac{\gamma_{m,i}}{\kappa_+}\frac{4G^2+\kappa_+^2}{4G^2+\kappa_+\gamma_{m,i}}\right) + n_{r,+}\left(\frac{4G^2}{4G^2+\kappa_+\gamma_{m,i}}\right). \tag{7.23}$$

7.4 Microwave Circuit properties and coil design

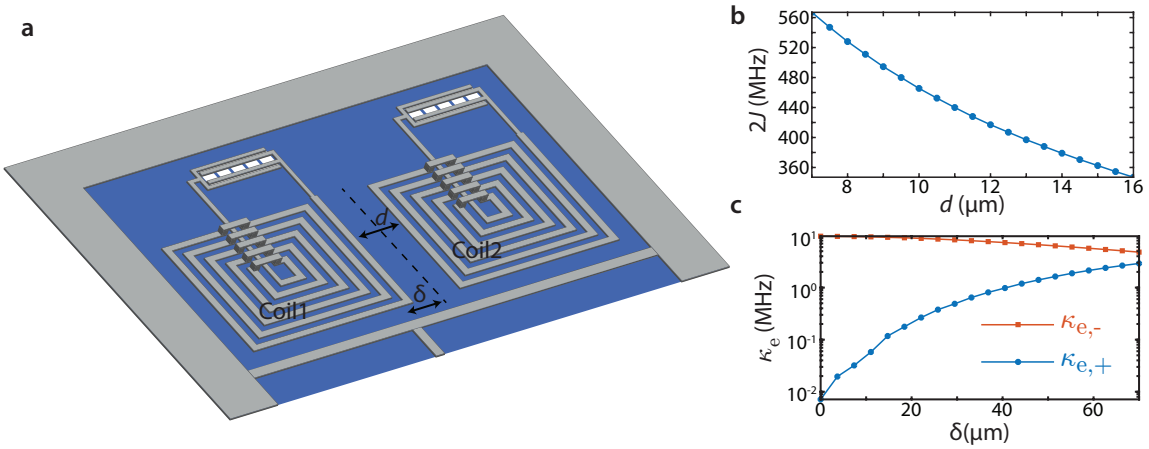

Figure 7.5: **a,** A schematic of the full electromechanical circuit. The microwave circuit is made of aluminum shown in gray color and the silicon membrane is shown in blue. The two LC microwave resonators consist of a high impedance coil which is capacitively coupled to a high frequency mechanical beam. Moreover, the microwave resonators are inductively coupled to each other. Tuning the distance between the two coils d allows for control over the strength of the coupling between the two LC resonators. Additionally, positioning of the two LC resonator system with respect to the branching point of the coupler wire allows for fine tuning of coupling of the even and odd supermodes to the microwave feed line. **b**, Shows the frequency splitting of the even and odd super modes $2J = \omega_{r,+} - \omega_{r,-}$ versus the distance between the coils. **c,** External coupling of even (odd) $\kappa_{e,+}(\kappa_{e,-})$ to the microwave feed line versus the separation between branching point of the coupler wire and the center of the two LC resonators δ.

The electromechanical circuit is composed of two identical LC coil resonators, each capacitively coupled to a mechanically compliant nanobeam supporting a mechanical mode with slightly different frequencies of 420 MHz and 425 MHz. Fig. 7.5a shows a schematic of the microwave electromechanical circuit. The coil Al wires are 500 nm wide and 120 nm thick, with a 1 μm pitch and 35 turns forming a square of dimension 74 μm$\times$74 μm. According to the finite element simulations, the coils have a self resonance frequency at $\omega_{srf}/2\pi = 13.98$ GHz. This simulation includes the cross-overs and the coupler wires. Using the modified Wheeler formula [77], the self inductance of the coil is $L = 41.8$ nH. Using the simple relation $\omega_{srf} = (LC_l)^{-\frac{1}{2}}$, we obtain the total stray capacitance of $C_s = C_c + C_p = 3.1$ fF, where C_c is the parasitic capacitance from the coil inductor and C_p is the extra parasitic capacitance due to the extra wiring. The modulating capacitance C_m for different gap size of the electrodes is shown in Fig. 7.1(d). From the measured g_0 in our experiment we estimate the capacitor gap to be $s \approx 40$ nm, from which we estimate the modulating capacitance to be $C_m = 2.1$ fF. This yields a participation factor of $\eta \approx 0.4$ and a bare LC coil resonance frequency of $\omega_{r,0}/2\pi = 10.77$ GHz (when adding the estimated motional capacitance to stray capacitance C_s of the coil and extra wiring). Using the simulated value of $2J$, we estimate $\omega_{r,+} = 10.9975$ GHz and $\omega_{r,-} = 10.5625$ GHz.

The two mechanical beams are designed to have the same length and gap size such that the modulating capacitance and the frequency of both microwave resonators are identical. By placing the two microwave resonator near each other, the two coils are inductively coupled forming an even and odd symmetry microwave supermodes. By adjusting the distance between the two inductors, we can control the strength of the mutual inductance hence, controlling the frequency splitting between the even and odd microwave mode. Figure 7.5(b) shows the frequency splitting between the two microwave modes as a function of the distance between the coil inductors. For the device presented in this manuscript, the distance is chosen to be $d = 12$ μm yielding a simulated frequency splitting of $2J/2\pi = 415$ MHz between the microwave modes. Moreover, the placement of the two inductors with respect the branching point of the coupler wire denoted by δ allows us to independently control the coupling of the microwave supermodes to the microwave feed line. Fig. 7.5(c) shows the coupling of the even and odd microwave modes to the microwave feed line versus the displacement of the coil inductors δ. For the chosen $\delta = 16.5$ μm, we expect the coupling of $\kappa_{e,+}/2\pi = 102$ kHz

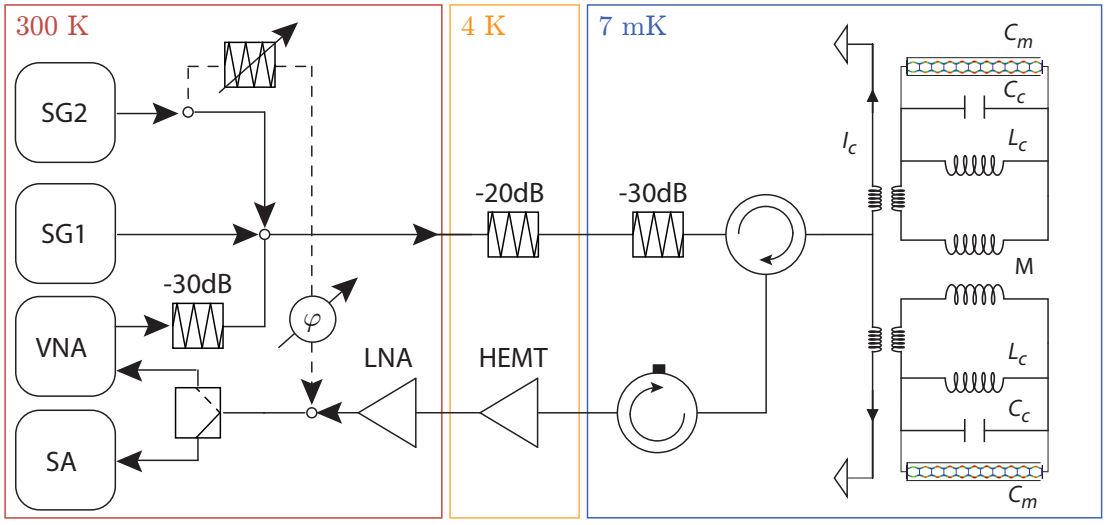

Figure 7.6: The output tone of a microwave signal generators (SG1 and SG2) and the output tone of a vector network analyzer (VNA) are combined at room temperature, attenuated, routed to the sample at about 7 mK and inductively coupled to the LC circuit on the silicon membrane. We detect the reflected output tone which is routed and isolated with two microwave circulators and after amplification with a high electron mobility transistor amplifier (HEMT) at 4K stage, switchable pump tone cancelation (dashed lines), and further amplification with a low noise amplifier (LNA). The measurement is done either phase coherently with the VNA, or we detect the incoherent power spectrum with the spectrum analyzer (SA).

for the even mode at higher frequency and $\kappa_{e,-}/2\pi = 9.6$ MHz for the odd mode at lower frequency. All the microwave LC resonator simulations are performed using the SONNET software package [76]. In these simulations we have assumed a relative permittivity of $\epsilon_{\mathrm{Si}} = 11.7$ for the silicon membrane.

7.5 Experimental Setup

For measuring the coherent and incoherent response of our circuit, we combine the output of a vector network analyzer with two other microwave sources and feed the microwave signals to the base plate of a cryogen free dilution refrigerator at $T_f \approx 10$ mK using coaxial cables with feedthroughs and attenuators for thermalization at each temperature stage yielding total attenuation of $\mathcal{A} = 76$ dB and suppressing room temperature Johnson noise (see Fig. 7.6) to about $n_{noise} = 0.05$ photons. We couple to the sample in a reflective geometry using a circulator and a low loss copper printed

circuit board (PCB). On the PCB and the chip we use 50 Ω coplanar waveguides (CPW) to route the microwave tones to the membrane with very little reflections (< 25 dB). Near the LC circuit, we extend the center conductor of the CPW waveguide and short it to ground with a narrow wire passing near the inductor coils and inductively couple to the microwave resonators.

On the output side, we use an isolator for isolating the sample from the 4 K stage noise. Niobium titanium superconducting cables are used to connect the isolator directly to a low noise, high electron mobility transistor amplifier (HEMT) at 4 K stage. The microwave signal is again amplified with a low noise room temperature amplifier (LNA). In order to suppress spurious response peaks for high drive power measurements, we cancel the high drive power tone by adding a phase and amplitude adjusted part of the pump tone to the output signal before the room temperature amplifier, as shown in Fig. 7.6. After the final amplification we use an electronically controlled microwave switch to distribute the signal to either the spectrum analyzer or the second vector network analyzer port. The total gain of the system is $\mathcal{G} = 57.6$ dB.

7.6 Fabrication

Figure 7.7(a) shows a scanning electron microscope (SEM) image of a fabricated version of the double-cavity device. This device is fabricated using an Al-on-SOI process introduced in Ref. [23] and Chapter (4) and consists of two LC lumped element microwave resonators which are inductively coupled to each other and capacitively coupled to a pair of hypersonic phononic crystal cavities of slightly different (5 MHz) design frequency. The Al layer is deposited using electron-beam evaporation, and patterning of the Si membrane and Al wiring is performed using electron beam lithography and a combination of plasma dry etching and lift-off. A SOI wafer with high resistivity ($\gtrsim 5$ kΩ) Si device and handle layers is used to reduce the microwave losses, and the buried-oxide (BOX) layer underlying the Si device layer is removed using an anhydrous hydroflouric acid vapor etch to avoid Al etching and stiction during the membrane release. Removal of the BOX layer is performed over an extended region covering the entire double-cavity structure in order to avoid the significant microwave losses in the BOX layer. Figure 7.7 shows a zoomed-in SEM image of one of the nanobeam acoustic cavities, indicating the placement of the Al capacitor electrodes and the approximately 70 nm vacuum-gap measured at room temperature.

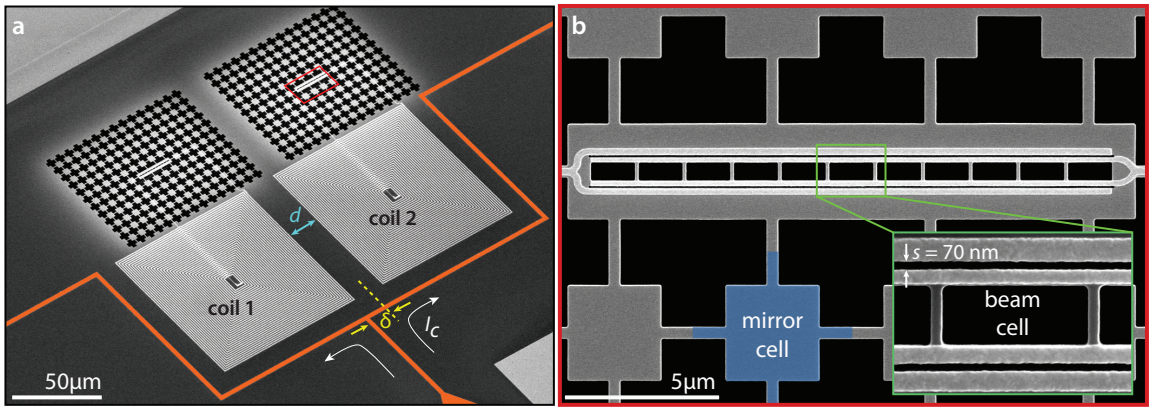

Figure 7.7: **a**, Zoomed-out SEM image of the entire double-cavity device fabricated on a SOI membrane. The two Al spiral coils, labeled coil 1 and coil 2, are shunted via the vacuum-gap capacitor of two independent nanobeam acoustic cavities which are embedded inside acoustic shields. Inductive coupling between the two coils is set by the gap d. External coupling of the two coils to a 50-Ω microwave drive line is performed by shorting the end of a CPW and splitting the current in the center trace into two paths (shunting wire shown in orange). The offset δ from the center of the coils where the wire path splits in two results in asymmetric coupling to the two coils, allowing for an adjustable amount of coupling between the even and odd supermodes of the coupled LC resonators. Parameters for this device are $d = 12$ μm and $\delta = 16.5$ μm, resulting in a simulated coil coupling of $2J/2\pi = 415$ MHz and external coupling rates of $\kappa_{e,-}/2\pi = 9.6$ MHz ($\kappa_{e,+}/2\pi = 102$ kHz) for the odd (even) mode. The bare (decoupled) frequency of the LC resonators is designed to be $\omega_{r,0}/2\pi = 10.86$ GHz for a capacitor vacuum gap of $s = 70$ nm. **b**, Zoomed-in SEM image of the nanobeam phononic crystal region of the acoustic cavity coupled to coil 2. The Si device layer and Al electrodes appear dark and light grey, respectively. A mirror cell of the surrounding acoustic bandgap shield is shaded in blue. Inset: SEM of a unit cell of the nanobeam phononic cavity indicating the $s = 70$ nm gap size at room temperature.

7.7 Measurement of Electromechanical Coupling and Acoustic Damping

As detailed in the caption of Fig. 7.7, microwave signals are launched onto a 50-Ω coplanar waveguide (CPW) on the SOI chip, the center conductor of which is extended and shorted to the ground in the near-field of the cavity. Electrical excitation of the circuit is provided by inductive coupling to the two spiral inductors, which for asymmetric placement of the shorting wire (see Fig. 7.7(a)) can lead to stronger loading of the anti-symmetric, lower frequency supermode which is used for pumping of the circuit. Read-out is performed in reflection. Vector network analyzer (VNA) microwave delay measurements of the device in Fig. 7.7 are plotted in Figs. 7.8(a) and 7.8(b), showing the presence of a heavily loaded low-Q resonance at $\omega_{r,-}/2\pi = 10.5788$ GHz and a more weakly coupled

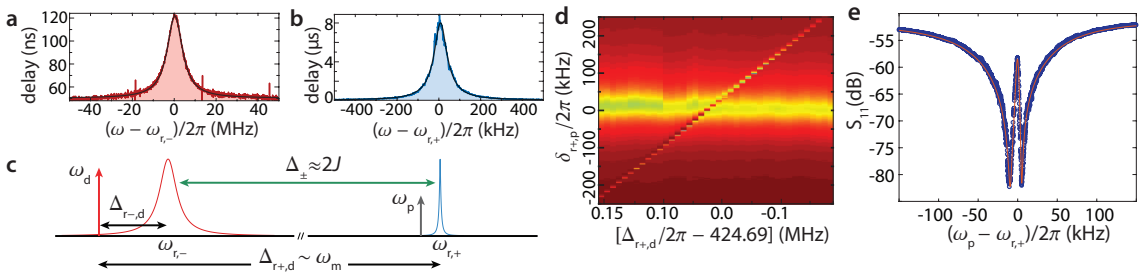

Figure 7.8: **a**, VNA measurement of the time delay response of the lower frequency, odd-symmetry-like microwave resonance centered at $\omega_{r,-}/2\pi = 10.5788$ MHz. **b**, Delay measurement of the higher frequency, even-symmetry-like resonance centered at $\omega_{r,+}/2\pi = 10.9930$ MHz. **c**, Schematic showing the drive and probe frequencies and relevant LC resonance detunings used in the two-tone microwave spectroscopy measurements. Here, ω_d is the drive frequency, which is placed near the low frequency LC resonance ($\omega_{r,-}$) and close to resonance with the lower motional sideband (red sideband) of the high frequency LC resonance ($\omega_{r,+}$). The high frequency cavity response is registered by sweeping the frequency (ω_p) of the weak probe tone. **d**, Color plot of the measured normalized reflection spectrum, $|S_{11}|$, of a weak coherent probe tone as a function of the detuning ($\Delta_{r+,d}$) of the strong drive tone. **e**, Plot of the measured probe tone spectrum around the high frequency LC resonance for a drive detuning at two-photon resonance, $\Delta_{r+,d} \approx \omega_m = 424.7$ MHz. In (**d**) and (**e**) the strength of the drive tone corresponds to an intra-cavity photon number in the lower LC anti-symmetric resonance of $n_{d,-} = 2.25 \times 10^5$.

high-Q resonance at $\omega_{r,+}/2\pi = 10.9930$ GHz. With a measured splitting of $\Delta_{\pm}/2\pi = 414.2$ MHz in close correspondence to the design tunnel-coupling rate of $2J/2\pi = 415$ MHz, the local modes of this device can be assumed to be strongly hybridized. Fitting the measured delay curves to a Lorentzian lineshape, we infer a total damping rate of $\kappa_+/2\pi = 230$ kHz and an external coupling rate of $\kappa_{e,+}/2\pi = 85$ kHz for the microwave mode at $\omega_{r,+}$. For the more strongly loaded resonance at $\omega_{r,-}$ we measure $\kappa_-/2\pi \approx \kappa_{e,-}/2\pi = 8.9$ MHz. The asymmetry and magnitude of the external coupling of both resonances are again close to the design values for the even and odd modes of the two coil resonator of Fig. 7.5. In order to probe the acoustic properties of the EMC we use a two-tone pump and probe scheme [83, 84, 111] illustrated schematically in Fig. 7.8(c). In this scheme a strong drive tone (ω_d) is applied at a variable detuning from the lower frequency microwave resonance while a weaker probe tone (ω_p) is scanned across the upper frequency microwave resonance. At two-photon resonance when the pump-probe difference frequency matches that of the capacitively-coupled acoustic mode frequency, $\omega_p - \omega_d = \omega_m$, beating of the drive and probe tones inside the microwave cavity coherently drive the acoustic mode, leading to interference effects in the externally detected probe tone spectrum due to emission of motional sidebands of the

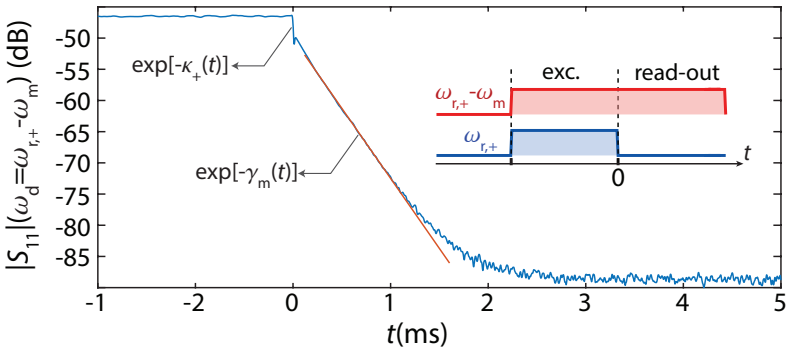

Figure 7.9: Pulsed excitation and read-out measurement of the ringdown of the acoustic energy in the nanobeam mechanical resonator. In this measurement the drive tone at 6 dBm power corresponding to intra-cavity photon number of $n_{d,-} = 1.42 \times 10^5$ is kept on after the excitation and the decay includes back action damping due to the drive tone. The initial steep decay results from the leakage of the photons from the microwave cavity. The decay rate of the mechanical resonator γ_m is extracted by fitting an exponential curve to the slow decay section of the signal versus time.

intracavity drive field. This results in the emergence of a transparency window in the reflected probe spectrum due to the acoustic 'dark state', similar to the phenomena of electromagnetically-induced transparency in atomic physics. In the weak-coupling, sideband-resolved limit the reflected probe spectrum is given by Eq. (7.20). Figure 7.8(d) shows a color plot of a series of probe scans as the pump detuning is stepped in frequency, showing the emergence and anti-crossing of an acoustic dark state resonance near $\Delta_{r+,d}/2\pi = 424.69$ MHz. A plot of the reflected probe spectrum for $\Delta_{r+,d}/2\pi = \omega_m/2\pi = 424.7$ MHz and $n_{d,-} = 2.25 \times 10^5$ photons is shown in Fig. 7.8(e). Fitting Eq. (7.20) to the measured probe spectrum we find a total linewidth of $\gamma/2\pi = 6.8$ kHz for the acoustic mode. This linewidth contains contributions from electromechanical back-action ($\gamma_{\rm em}$), intrinsic energy damping of the acoustic mode ($\gamma_{m,i}$), and any pure dephasing of the acoustic mode.

As frequency jitter is observed in the dark state resonance of the probe spectrum at low pump power, a more direct measure in the time-domain of the intrinsic acoustic damping and the electromechanical back-action is employed. As in the EIT-like spectroscopy, here we apply a 100 ms two-tone pulse to ring up the mechanics with a strong drive tone at $\omega_d = \omega_{r,+} - \omega_m$ and a weak probe tone at $\omega_p = \omega_{r,+}$. Detection of the acoustic mode occupancy is performed with a read-out pulse in which the weak probe tone is turned off and motionally scattered photons from the strong drive tone (still at $\omega_d = \omega_{r,+} - \omega_m$) are detected on a spectrum analyzer in zero-span mode with center frequency at $\omega_{r,+}$ and resolution bandwidth (RBW) set to 30 kHz ($\gg \gamma/2\pi$). An exam-

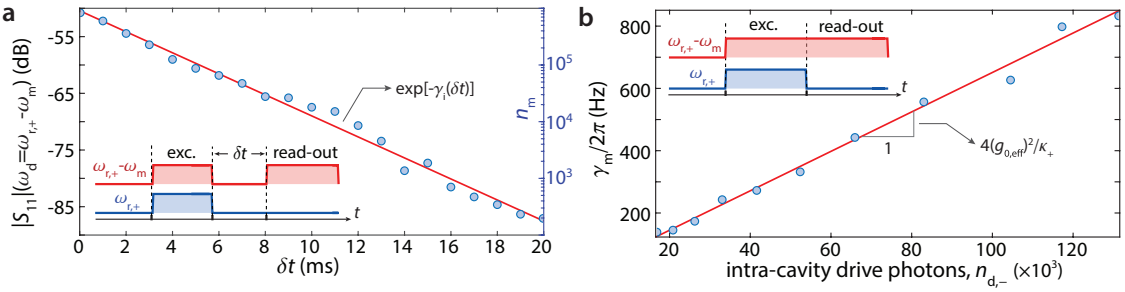

Figure 7.10: **a**, Pulsed excitation and read-out measurement of the ringdown of the acoustic energy in the nanobeam resonator. Here ringdown occurs 'in the dark' with all microwave fields off. **b**, The measured energy decay rate of the acoustic resonator, γ, as a function of the power of the drive tone. Here the drive tone is kept on after excitation and the energy decay includes parametric back-action (and parasitic) damping due to the drive tone. The vacuum electromechanical coupling g_0 is extracted by fitting the measured decay rate γ versus the estimated intra-cavity photon number of the drive tone ($n_{d,-}$).

ple of the the time-domain measurement is plotted in Fig. 7.9. Figure 7.10(a) shows a plot of the measured ringdown of the acoustic mode energy as a function of the delay, δt, between the end of the ring up pulse and the beginning of the read-out pulse (see inset). This 'ringdown in the dark' measurement yields the intrinsic energy damping rate of the mechanics, which for the breathing mode at $\omega_m/2\pi = 424.7$ MHz is measured to be $\gamma_{m,i}/2\pi = 68$ Hz (phonon lifetime $\tau = 2.3$ ms), corresponding to a Q-factor of 6.25×10^6.

To extract the back-action induced damping rate of the breathing mode, the read-out pulse delay is set to $\delta t = 0$ and the motionally scattered photons within the read-out pulse are measured as a function of time. Fitting an exponential decay curve to the time-varying detected read-out signal on the spectrum analyzer for varying read-out pulse powers, Fig. 7.10(b) plots the back-action damped acoustic energy decay rate, $\gamma_m = \gamma_{m,i} + \gamma_{\rm em}$, versus pulse amplitude in units of intra-cavity photon number, $n_{d,-}$. As the back-action damping rate for red-sideband pumping is given by $\gamma_{\rm em} \approx 4g_{0,\pm}^2 n_{d,-}/\kappa_+$, the slope of this plot yields a vacuum electromechanical coupling rate for the breathing mode of $g_{0,\pm}/2\pi = 17.3$ Hz (corresponding to $g_0/2\pi = 34.6$ Hz). Referring to Fig. 7.1(d), this value is substantially larger than that expected for the vacuum-gap size of $s = 70$ nm measured via SEM at room temperature. We attribute this difference to a shrinking of the gap to $s \approx 40$ nm due to an increase in the tensile strain of the Al wires on the nanobeam as the device is cooled to cryogenic temperatures. This is consistent with the observation that devices with gaps

smaller than $s \lesssim 60$ nm at room temperature did not show any acoustic resonances when cooled down (the lack of a second acoustic resonance in the device studied here being an example).

7.8 Mechanical Frequency Jitter

As captured by the cooperativity, $C \equiv \gamma_{\text{em}}/\gamma_{m,i}$, the long phonon lifetime and large electromechanical back-action measured in Fig. 7.10 indicate that coherent manipulation of the breathing mode via microwave drive fields is possible. For quantum applications one is also interested in the quantum cooperativity defined as $C_{\text{eff}} \equiv C/n_b$, where n_b is a noise occupancy (Bose factor) of the bath coupled to the acoustic mode. $C_{\text{eff}} > 1$ allows for coherent manipulations of the mechanics on a timescale faster than decoherence caused by the bath, or in terms of dissipative processes, back-action cooling of the mechanical mode to its quantum ground state. Characterization of the noise baths coupled to the EMC are explored here by monitoring the noise power spectrum generated on the upper motional sideband of a pump tone at $\omega_d = \omega_{r,+} - \omega_m$ (as in the read-out pulse of the ringdown measurements, but with the spectrum analyzer swept over a finite span with narrow RBW).

Plotted in Fig. 7.11(a) is the noise power spectral density (NPSD) measured at the upper motional sideband of the pump tone ($\approx \omega_{r,+}$). In this plot the blue shaded spectrum labelled S_{th} is the back-action damped noise spectrum of the breathing mode, magnified by a factor of $\times 40$ for visibility. The measured linewidth of this spectrum is 6.7 kHz, substantially larger than the estimated linewidth from back-action and intrinsic damping alone ($[\gamma_{m,i} + \gamma_{\text{em}}]/2\pi \approx 2$ kHz). This broadening of the mechanical spectrum is due to time-averaging of the aforementioned frequency jitter. Although a microscopic understanding of the source of the measured frequency jitter is beyond the scope of this work, an estimate of the time scale of the jitter noise can be determined using the method described in Refs. [138, 139] in which a weak coherent tone is applied close to the upper motional sideband. The resulting NPSD is shown in Fig. 7.11(a), where the spectrum is separated into a broad thermal-like spectrum (S_{bb}; red curve) and a narrower spectrum around the applied coherent tone (S_{nb}; green curve). Acoustic frequency fluctuations faster than the instantaneous linewidth (given by $\gamma_{m,i}+\gamma_{\text{em}}$) contribute to S_{bb}, whereas slower frequency fluctuations add to the narrow spectrum S_{nb}, from which we estimate that 15% (58%) of the measured total linewidth is a result of fast (slow) frequency jitter

noise. see section. 7.8.1 for details.

7.8.1 Analysis

Our analysis of the frequency noise of the breathing mode follows that from Refs. [138, 139]. A main takeaway from the referenced work is that frequency fluctuations slower than the decay rate of the the mechanical resonance ($\delta\omega \ll \gamma_m$), can be considered as slow fluctuations in the mechanical susceptibility leading to slow variation in amplitude and phase of the driven response. Thus an applied near resonant tone is spectrally broadened around its frequency ω_F. For frequency fluctuations faster than the decay rate of the mechanical oscillator ($\delta_\omega \gg \gamma_m$), the driving term quickly looses the memory of the driving frequency and becomes more similar to the thermal spectrum with the only difference being that the amplitude of the signal is dependent more on the driving amplitude than the temperature of the mechanical oscillator. Therefore, fast fluctuations in the mechanical oscillator frequency lead to added noise over the entire broadened mechanical response.

Figure 7.11a shows the narrowband (slow) and broadband (fast) spectra of the mechanical frequency response in the presence of a weak coherent tone applied near resonance. We denote the area of the narrowband and broadband peaks by S_{nb} and S_{bb}, respectively. We can estimate the broadband component of the frequency jitter of the mechanical oscillator by measuring the area underneath the narrowband and broadband peaks and using the relation

$$\frac{\tilde{\gamma}_m}{\gamma_m} \approx 1 + \frac{S_{bb}}{S_\delta}\left(1 - \frac{S_{nb}}{S_\delta}\right), \tag{7.24}$$

where $\tilde{\gamma}_m$ is the broadened mechanical linewidth and S_δ corresponds to the area underneath the applied coherent tone in the absence of mechanical interaction, measured by detuning the tone frequency away from the mechanical resonance.

7.9 Mechanical Thermometry

Calibration of the reflected signal amplification (along with the electromechanical back-action rate) allows us to relate the area under the NPSD spectrum S_{th} to an estimate of the noise phonon occupancy of the breathing mode, n_m [82]. A plot of the inferred n_m versus drive photon number $n_{d,-}$

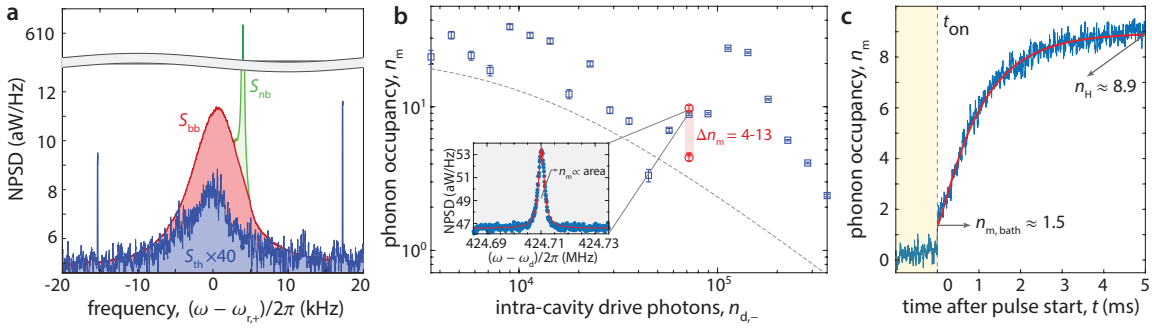

Figure 7.11: **a**, Measured electrical NPSD spectrum at the upper LC resonance ($\omega_{r,+}$) under red-detuned pumping with drive frequency $\Delta_{r+,d} \approx \omega_m$ and $n_{d,-} = 4.3 \times 10^5$, with and without an additional weak tone at $\omega_{r,+}/2\pi + 4$ kHz. With the weak tone off, the measured NPSD is just that of the back-action damped acoustic resonance ($S_{\rm th}$; blue curve, magnified by $\times 40$). With the weak tone on, the measured noise spectrum can be separated into two distinct components, a broad thermal-like spectrum $S_{\rm bb}$ (red curve) and a narrow noise peak around the weak coherent tone $S_{\rm nb}$ (green curve). **b**, Back-action cooling curve showing measured phonon occupancy versus drive tone power for a pump frequency $\Delta_{r+,d} \approx \omega_m$. Dashed grey curve corresponds to expected back-action cooling curve for bath temperature $T_b = 500$ mK. Inset: measured NPSD at a drive power of $n_{d,-} = 7.1 \times 10^4$. **c**, Calibrated noise power in units of breathing mode phonon number, n_m, versus time during a red-detuned ($\omega_d = \omega_{r,+} - \omega_m$) drive pulse. Here a pulse train with pulse period $T_{\rm per} = 30$ ms and on-pulse length $T_{\rm on} = 15$ ms is utilized. Pulse amplitude corresponds to an intra-cavity drive photon number $n_{d,-} = 7.1 \times 10^4$. The solid red curve shows a heating model fit to the data with pump-induced hot bath occupancy $n_H = 8.9$. See Sec. 7.9.1 for details of the heating model

is shown in Fig. 7.11(b). Although significant back-action cooling [70] is expected based upon the measured cooperativity, the variation in n_m versus drive power is highly irregular. The breathing mode starts out hot at low power, following a weak cooling trend with large fluctuations between different drive powers. Repeated measurement of n_m at a single drive power also show fluctuations (see red data points at $n_{d,-} = 7.1 \times 10^4$ in Fig. 7.11(b)). In order to confirm that the breathing mode is thermalized close to the fridge temperature in absence of microwave driving of the circuit, we plot in Fig. 7.11(c) the total measured acoustic noise power versus time as the red-sideband cooling pump tone is pulsed on. The calibrated breathing mode occupancy at the onset of the pulse is measured to be $n_m = 1.5$ (mode temperature $T_m \approx 40$ mK), and then heats over several milliseconds up to an occupancy $n_H = 8.9$. Over a train of pulses the value of n_H is seen to fluctuate on timescales of a few seconds to minutes, with a variance consistent with the continuous-wave mode occupancy measurements.

7.9.1 Heating Model

The heating curve observed in Fig. 7.11(c) fits well to the phenomenological heating model introduced in Ref. [140]. This model assumes the coupling between the mechanical oscillator and three different thermal baths. First, the red side-band drive turns on the radiation pressure coupling between the mechanical oscillator and the effective zero-temperature coherent drive with rate γ_{em} cooling the mechanical oscillator. Second, the mechanical oscillator itself is coupled to the ambient fridge bath with occupancy $n_{m,\text{bath}}$ at an intrinsic rate $\gamma_{m,i}$ and third, it is coupled to a pump induced hot bath with occupancy $n_{m,p}$ and coupling rate γ_p. Moreover, to best capture the dynamics of the heating curve, it is assumed that the hot bath has a finite equilibration time. Thus the red curve fitted to the data assumes that a fraction of the hot thermal bath turns on almost instantaneously, while the remainder has a slow exponential increase to its steady state value. Thus we can write a simple phenomenological rate equation:

$$\dot{n}_m = -\gamma n_m + \gamma_p n_{m,p}(1 - \delta_b e^{-\gamma_s t}) + \gamma_{m,i} n_{m,\text{bath}}, \tag{7.25}$$

where $\gamma = \gamma_{m,i} + \gamma_{em} + \gamma_p$, δ_b is the slow growing fraction of $n_{m,p}$ and γ_s is the turn-on rate. Assuming a constant γ_p, this rate equation has a simple solution of the form

$$n_m(t) = n_{m,\text{bath}} e^{-\gamma t} + n_H(1 - e^{-\gamma t}) + n_\delta(e^{-\gamma_s t} - e^{-\gamma t}), \tag{7.26}$$

where n_δ and n_H are defined by

$$n_\delta = \frac{\gamma_p n_p \delta_b}{\gamma_s - \gamma} \tag{7.27}$$

$$n_H = \gamma^{-1}(\gamma_p n_p + \gamma_{m,i} n_{m,\text{bath}}). \tag{7.28}$$

Chapter 8

Conclusion

Radiation pressure has been used to effectively couple the quantum motion of mechanical elements to the field of optical and microwave light. Integration of all three degrees of freedom (*i.e.*, mechanical, optical, and microwave) would enable a quantum interconnect between the microwave and optical quantum systems. This dissertation is the culmination of a concentrated effort towards developing an integrated platform compatible both with superconducting qubits and photonics operating at communication wavelength band. The design, fabrication, and characterization of integrated electromechanical circuits capable of coupling to photonic crystal cavities based on silicon nitride nanomembranes and free standing silicon membranes formed from a silicon-on-insulator wafer are presented.

Utilizing Si_3N_4 nanomembranes as a substrate for superconducting microwave circuits, we demonstrate the formation of a high impedance circuit element with large per photon electric field strength. In this work, the reduced thickness and low dielectric constant of the nanomembrane help realize a microwave resonator with an estimated vacuum field strength as large as $E_{\text{vac}} \approx 260$ V/m. This feature gives rise to a large electromechanical coupling that we observe to the fundamental flexural mode of an integrated phononic crystal nanobeam. Dynamical backaction cooling via a strong microwave drive tone results in an occupancy of $n_m = 0.58$ for the 4.48 MHz flexural mode of the beam, limited here by heating of the circuit due to absorption of the microwave drive at the highest powers while measured in a dilution refrigerator at $T_f = 10$ mK. Substantial further reduction in the coil and stray capacitance should be possible through tighter coil wiring and a more optimized layout of the capacitor wiring, respectively, greatly reducing the required drive power (and the corresponding heating) for backaction cooling to the quantum ground state.

I describe our work on developing aluminum-on-silicon fabrication process for creation of a high-Q aluminum (Al) superconducting microwave resonator on thin film silicon membranes in Chapter.5. Utilizing this novel fabrication process described in Chapter. 6, we demonstrate a high impedance, high-Q 10 GHz coil resonator that is coupled capacitively with a large participation ratio to a ≈ 6 MHz micro-mechanical resonator. We use two-tone microwave spectroscopy and radiation pressure back action to characterize the coupled electromechanical system in the dilution refrigerator and we measure the vacuum electromechanical coupling rate of $g_0/2\pi = 230$ Hz to the mechanical resonator with the high Q-factor of $Q_m = 2.1 \times 10^6$. Utilizing microwave radiation pressure back-action cooling of the mechanical resonator, we realize a minimum phonon occupancy of $n_m = 0.1$ phonon with only 3×10^3 microwave photons. Thus, SOI represents a unique platform for integrating microwave, mechanical, and optical circuits, which is particularly interesting in the context of recent proposals and experimental efforts to utilize mechanical elements as quantum converters between the microwave and optical photons [30, 83, 107–110, 141]. For this application one has three main metrics of interest: conversion efficiency, conversion bandwidth, and added noise. All three parameters rely on realizing a large optomechanical and electromechanical vacuum coupling rate. In the case of optomechanical coupling, the relatively large refractive index and elasto-optic coefficients of Si have enabled substantially larger optomechanical coupling, at the level of $g_0/2\pi = 1$ MHz [25], in comparison to other thin-film photonic devices such as those formed in silicon nitride [75]. Moreover, the relatively low optical loss of silicon (Si) in the telecom band [142, 143], in comparison to GaAs for instance [115, 144], is key in reducing the parasitic heating of the mechanical resonator, which ultimately limits the added noise in the conversion process [28, 140]. In addition, the demonstration of relatively large electromechanical coupling, comparable to the state of the art aluminum drumhead resonators [84, 145], low microwave resonator loss, and very low mechanical damping, indicates that efficient and low noise microwave photon-phonon conversion is possible on a SOI platform.

However, in order to utilize these devices as a part of hybrid quantum circuits architecture, capable of interfacing superconducting qubits and optical photons, GHz level mechanical resonance frequency is required to operate in the sideband-resolved limit of optomechanics [82], a crucial parameter regime for realizing noise-free microwave to optical quantum signal conversion [28, 146].

Toward this effort, the use of piezoelectric materials can enable MHz-level electromechanical coupling and operation at GHz-level frequencies. The piezoelectric coupling, however, cannot be turned off, nor is it perfectly mode selective, and poly-crystalline piezoelectric materials harbor lossy defects in comparison to the radiation pressure parametric coupling which can be dynamically controlled. Both these effects can lead to parasitic electrical and acoustic decoherence. In comparison, parametric radiation pressure coupling can be dynamically controlled and is relatively materials agnostic. To that end, utilizing the aluminum (Al) on silicon process which has been effective in forming low-loss superconducting quantum circuits, we demonstrate a form of electromechanical crystal for coupling microwave photons and hypersonic phonons by embedding the vacuum-gap capacitor of a superconducting resonator within a phononic crystal acoustic cavity. Utilizing a two-photon resonance condition for efficient microwave pumping and a phononic bandgap shield to eliminate acoustic radiation, we demonstrate large cooperative coupling ($C \approx 30$) between a pair of electrical resonances at $\omega_{r,0} \approx 10$ GHz and an acoustic resonance at $\omega_m/2\pi = 0.425$ GHz. Electrical read-out of the phonon occupancy shows that the hypersonic acoustic mode has long intrinsic energy decay time of 2.3 ms and thermalizes close to its quantum ground state of motion (occupancy $n_m = 1.5$) at a fridge temperature of $T_f = 10$ mK. Despite this, the measured noise power spectral density of the mechanical mode indicates the broadening of the spectrum due to frequency jitter and anomalous mechanical heating.

The source(s) of the frequency jitter and the heating observed in the current device is not well understood at this point; however, there are a few candidate sources to consider. Two-level tunneling systems (TLS) [133] found within amorphous surface oxide layers are known to cause excess damping and noise in microwave superconducting quantum circuits [103]. TLS also couple to strain fields, and the high frequency of the hypersonic breathing mode may lead to coupling (via nonlinear phonon-phonon or TLS-phonon scattering) to the same TLS bath as that of the microwave pump. The observed fluctuation in the breathing mode occupancy is also reminiscent of the bursty nature of quasi-particle (QP) generation measured in thin films of superconducting aluminum [147, 148] due to high energy particle impacts. Modeling of the interaction of QPs with sub-gap electromagnetic radiation indicates that even weak microwave probe fields can lead to non-equilibrium QP and phonon distributions above that of the thermal background [149]. Both TLS and QP considerations

Material	T_c (K)	Δ (μeV)	$\tau_{QP,max}$
Al	1.11	168	3.5 ms
Nb	9.2	1395	1 ns
TiN	0.7-4.5	100-650	200 μs
NbTiN	14.5	2200	1 ns

Table 8.1: Typical parameters of critical temperature T_c, superconducting energy gap Δ and the relaxation time of the quasi particle for various materials.

indicate that moving to a different superconducting material with short QP relaxation time and a clean surface — such as NbTiN [150] — may significantly reduce acoustic mode heating and frequency jitter. Table 8.1 lists the relaxation time of QPs in different materials in comparison to the aluminum [147]. An additional attribute of NbTiN is its large kinetic inductance [151], which can be employed to further reduce parasitic capacitance and increase the electromechanical coupling.

Moreover, the electromechanical crystal (EMC) presented here offers the prospect of high bandwidth transduction in the MHz range required for integration with superconducting qubits. Improvements in circuit design can help further increase the backaction rate and the operational bandwidth. One approach would be to use a lower frequency drive or a DC source [122, 152] as the parametric pump (effectively replacing the lower frequency microwave resonance in the current devices), which could dramatically reduce the heating caused by absorption of drive photons. A simple scaling of the device used here indicates that for an applied bias of 10 V, electromechanical coupling at the MHz-level should be possible to acoustic modes at frequencies up to several GHz.

Bibliography

[1] Kepler, J. *De Cometis Libelli Tres* (Augsburg, 1619).

[2] Maxwell, J. C. *A treatise on electricity and magnetism*, vol. 2 (Clarendon Press, Oxford, 1873).

[3] Nichols, E. F. & Hull, G. F. A preliminary communication on the pressure of heat and light radiation. *Phys. Rev.* **13**, 307–320 (1901).

[4] Lebedev, P. Untersuchungen über die Druckkräfte des Lichtes. *Ann. Phys.* **6**, 433–458 (1901).

[5] Ashkin, A. Trapping of atoms by resonance radiation pressure. *Phys. Rev. Lett.* **40**, 729–732 (1978). URL `https://link.aps.org/doi/10.1103/PhysRevLett.40.729`.

[6] Wineland, D. J. & Itano, W. M. Laser cooling of atoms. *Phys. Rev. A* **20**, 1521–1540 (1979).

[7] Braginsky, V. B. *Eksp. Teor. Fiz.* **53**, 1434 (1967).

[8] Braginsky, V. B., Manukin, A. B. & Tikhonov, M. Y. Investigation of dissipative ponderomotive effects of electromagnetic radiation. *Sov. Phys. JETP* **31**, 829 (1970).

[9] Cuthbertson, B. D., Tobar, M. E., Ivanov, E. N. & Blair, D. G. Parametric backâ□□action effects in a highâ□□q cyrogenic sapphire transducer. *Review of Scientific Instruments* **67**, 2435–2442 (1996). URL `https://doi.org/10.1063/1.1147193`. `https://doi.org/10.1063/1.1147193`.

[10] Caves, C. M., Thorne, K. S., Drever, R. W. P., Sandberg, V. D. & Zimmermann, M. On the measurement of a weak classical force coupled to a quantum-mechanical oscillator. I. Issues of principle. *Rev. Mod. Phys.* **52**, 341–392 (1980).

[11] Braginsky, V. & Manukin, A. *Measurement of weak forces in Physics experiments* (Univ. of Chicago Press, 1977).

[12] Braginsky, V. & Khalili, F. *Quantum Measurements* (Cambridge University Press, 1995).

[13] Aspelmeyer, M., Kippenberg, T. J. & Marquardt, F. Cavity optomechanics. *arXiv:1303.0733* (2013).

[14] B. Abbott, et al. Observation of a kilogram-scale oscillator near its quantum ground state. *New J. Phys.* **11**, 073032 (2009).

[15] Arcizet, O., Cohadon, P.-F., Briant, T., Pinard, M. & Heidmann, A. Radiation-pressure cooling and optomechanical instability of a micromirror. *Nature* **444**, 71–74 (2006).

[16] Blair, D. G. *et al.* High sensitivity gravitational wave antenna with parametric transducer readout. *Phys. Rev. Lett.* **74**, 1908– (1995).

[17] Brown, K. R. *et al.* Passive cooling of a micromechanical oscillator with a resonant electric circuit. *Phys. Rev. Lett.* **99** (2007).

[18] Usenko, O., Vinante, A., Wijts, G. & Oosterkamp, T. H. A superconducting quantum interference device based read-out of a subattonewton force sensor operating at millikelvin temperatures. *Appl. Phys. Lett.* **98**, 133105 (2011). URL `http://link.aip.org/link/?APL/98/133105/1`.

[19] Lecocq, F., Clark, J. B., Simmonds, R. W., Aumentado, J. & Teufel, J. D. Quantum nondemolition measurement of a nonclassical state of a massive object. *Phys. Rev. X* **5**, 041037 (2015).

[20] Teufel, J. D., Donner, T., Castellanos-Beltran, M. A., Harlow, J. W. & Lehnert, K. W. Nanomechanical motion measured with an imprecision below that at the standard quantum limit. *Nat Nano* **4**, 820–823 (2009). URL `http://www.citebase.org/abstract?id=oai:arXiv.org:0906.1212`.

[21] Teufel, J. D. *et al.* Sideband cooling of micromechanical motion to the quantum ground state. *Nature* **475**, 359–363 (2011).

[22] Fink, J. M. *et al.* Quantum electromechanics on silicon nitride nanomembranes. *arXiv:1512.04660* (2015).

[23] Dieterle, P. B., Kalaee, M., Fink, J. M. & Painter, O. Superconducting cavity electromechanics on a silicon-on-insulator platform. *Phys. Rev. Applied* **6**, 014013 (2016). URL `http://link.aps.org/doi/10.1103/PhysRevApplied.6.014013`.

[24] Chan, J. *et al.* Laser cooling of a nanomechanical oscillator into its quantum ground state. *Nature* **478**, 89–92 (2011). URL `http://dx.doi.org/10.1038/nature10461`.

[25] Chan, J., Safavi-Naeini, A. H., Hill, J. T., Meenehan, S. & Painter, O. Optimized optomechanical crystal cavity with acoustic radiation shield. *Appl. Phys. Lett.* **101**, 081115 (2012).

[26] Davanço, M., Chan, J., Safavi-Naeini, A. H., Painter, O. & Srinivasan, K. Slot-mode-coupled optomechanical crystals. *Opt. Express* **20**, 24394–24410 (2012). URL `http://www.opticsexpress.org/abstract.cfm?URI=oe-20-22-24394`.

[27] Safavi-Naeini, A. H. & Painter, O. Proposal for an optomechanical traveling wave phonon-photon translator. *New Journal of Physics* **13**, 013017 (2011). URL `http://stacks.iop.org/1367-2630/13/i=1/a=013017`.

[28] Hill, J. T., Safavi-Naeini, A. H., Chan, J. & Painter, O. Coherent optical wavelength conversion via cavity optomechanics. *Nature Commun.* **3**, 1196 (2012). `1206.0704`.

[29] Lecocq, F., Clark, J. B., Simmonds, R. W., Aumentado, J. & Teufel, J. D. Mechanically mediated microwave frequency conversion in the quantum regime. *Phys. Rev. Lett.* **116**, 043601 (2016). URL `https://link.aps.org/doi/10.1103/PhysRevLett.116.043601`.

[30] Andrews, R. W. *et al.* Bidirectional and efficient conversion between microwave and optical light. *Nature Physics* **10**, 321–326 (2014).

[31] Thompson, J. D. *et al.* Strong dispersive coupling of a high-finesse cavity to a micromechanical membrane. *Nature* **452**, 72–75 (2008).

[32] Miao, H., Danilishin, S., Corbitt, T. & Chen, Y. Standard quantum limit for probing mechanical energy quantization. *Phys. Rev. Lett.* **103**, 100402 (2009). URL http://link.aps.org/doi/10.1103/PhysRevLett.103.100402.

[33] Ludwig, M., Safavi-Naeini, A. H., Painter, O. & Marquardt, F. Enhanced quantum nonlinearities in a two-mode optomechanical system. *Phys. Rev. Lett.* **109**, 063601 (2012). URL http://link.aps.org/doi/10.1103/PhysRevLett.109.063601.

[34] Sankey, J. C., Yang, C., Zwickl, B. M., Jayich, A. M. & Harris, J. G. E. Strong and tunable nonlinear optomechanical coupling in a low-loss system. *Nature Phys.* **6**, 707Ð712 (2010). URL http://dx.doi.org/10.1038/nphys1707.

[35] Flowers-Jacobs, N. E. *et al.* Fiber-cavity-based optomechanical device. *Appl. Phys. Lett.* **101**, – (2012). URL http://scitation.aip.org/content/aip/journal/apl/101/22/10.1063/1.4768779.

[36] Clerk, A. A., Marquardt, F. & Harris, J. G. E. Quantum measurement of phonon shot noise. *Phys. Rev. Lett.* **104**, 213603 (2010). URL http://link.aps.org/doi/10.1103/PhysRevLett.104.213603.

[37] Yanay, Y., Sankey, J. C. & Clerk, A. A. Quantum backaction and noise interference in asymmetric two-cavity optomechanical systems. *Phys. Rev. A* **93**, 063809 (2016). URL https://link.aps.org/doi/10.1103/PhysRevA.93.063809.

[38] Purdy, T. P. *et al.* Tunable cavity optomechanics with ultracold atoms. *Phys. Rev. Lett.* **105**, 133602 (2010). URL http://link.aps.org/doi/10.1103/PhysRevLett.105.133602.

[39] Thompson, J. D. *et al.* Strong dispersive coupling of a high-finesse cavity to a micromechanical membrane. *Nature* **452**, 72Ð75 (2008). URL http://dx.doi.org/10.1038/nature06715.

[40] Bhattacharya, M., Uys, H. & Meystre, P. Optomechanical trapping and cooling of partially reflective mirrors. *Phys. Rev. A* **77**, 033819 (2008). URL http://link.aps.org/doi/10.1103/PhysRevA.77.033819.

[41] Nunnenkamp, A., Børkje, K., Harris, J. G. E. & Girvin, S. M. Cooling and squeezing via quadratic optomechanical coupling. *Phys. Rev. A* **82**, 021806 (2010). URL `http://link.aps.org/doi/10.1103/PhysRevA.82.021806`.

[42] Asjad, M. *et al.* Robust stationary mechanical squeezing in a kicked quadratic optomechanical system. *Phys. Rev. A* **89**, 023849 (2014). URL `http://link.aps.org/doi/10.1103/PhysRevA.89.023849`.

[43] Vanner, M. R. Selective Linear or Quadratic Optomechanical Coupling via Measurement. *Phys. Rev. X* **1**, 021011 (2011).

[44] Doolin, C. *et al.* Nonlinear optomechanics in the stationary regime. *Phys. Rev. A* **89**, 053838 (2014). URL `http://link.aps.org/doi/10.1103/PhysRevA.89.053838`.

[45] Kaviani, H. *et al.* Nonlinear optomechanical paddle nanocavities. *Optica* **2**, 271–274 (2014).

[46] Santamore, D. H., Goan, H.-S., Milburn, G. J. & Roukes, M. L. Anharmonic effects on a phonon-number measurement of a quantum-mesoscopic-mechanical oscillator. *Phys. Rev. A* **70**, 052105 (2004).

[47] Jayich, A. M. *et al.* Dispersive optomechanics: a membrane inside a cavity. *New J. Phys.* **10**, 095008 (2008).

[48] Gangat, A. A., Stace, T. M. & Milburn, G. J. Phonon number quantum jumps in an optomechanical system. *New J. Phys.* **13**, 043024 (2011).

[49] Stannigel, K. *et al.* Optomechanical quantum information processing with photons and phonons. *Phys. Rev. Lett.* **109**, 013603 (2012). URL `http://link.aps.org/doi/10.1103/PhysRevLett.109.013603`.

[50] Ludwig, M. *Collective quantum effects in optomechanical systems*. Ph.D. thesis, University of Erlangen-Nuremberg (2013).

[51] Kalaee, M., Paraïso, T. K. & Painter, O. Design of a quasi-2d photonic crystal optomechanical cavity with tunable, large x^2-coupling (2015).

[52] Johnson, S. G. & Joannopoulos, J. D. Block-iterative frequency-domain methods for maxwell's equations in a planewave basis. *Opt. Express* **8**, 173–190 (2001). URL http://www.opticsexpress.org/abstract.cfm?URI=OPEX-8-3-173.

[53] The MIT Photonic-Bands (MPB) software package, http://ab-initio.mit.edu/mpb.

[54] COMSOL Multiphysics 3.5, http://www.comsol.com/.

[55] Safavi-Naeini, A. H., Alegre, T. P. M., Winger, M. & Painter, O. Optomechanics in an ultrahigh-q two-dimensional photonic crystal cavity. *Appl. Phys. Lett.* **97**, – (2010). URL http://scitation.aip.org/content/aip/journal/apl/97/18/10.1063/1.3507288.

[56] Winger, M. *et al.* A chip-scale integrated cavity-electro-optomechanics platform. *Opt. Express* **19**, 24905–24921 (2011). URL http://www.opticsexpress.org/abstract.cfm?URI=oe-19-25-24905.

[57] Aspelmeyer, M., Kippenberg, T. J. & Marquardt, F. Cavity optomechanics. *Rev. Mod. Phys.* **86**, 1391–1452 (2014). URL http://link.aps.org/doi/10.1103/RevModPhys.86.1391.

[58] Eichenfield, M., Chan, J., Camacho, R., Vahala, K. & Painter, O. Optomechanical crystals. *Nature* **462**, 78–82 (2009).

[59] Fan, L., Fong, K. Y., Poot, M. & Tang, H. X. Cascaded optical transparency in multimode-cavity optomechanical systems. *Nature Communications* **6**, 5850 (2015). URL http://dx.doi.org/10.1038/ncomms6850http://10.0.4.14/ncomms6850https://www.nature.com/articles/ncomms6850{#}supplementary-information.

[60] Ojanen, T. & Børkje, K. Ground-state cooling of mechanical motion in the unresolved sideband regime by use of optomechanically induced transparency. *Phys. Rev. A* **90**, 013824 (2014). URL https://link.aps.org/doi/10.1103/PhysRevA.90.013824.

[61] Johnson, S. G. *et al.* Perturbation theory and Maxwell's equations with shifting material boundaries. *Phys. Rev. E* **65**, 066611 (2002).

[62] Zhao, B. *et al.* A millisecond quantum memory for scalable quantum networks. *Nat. Phys.* **5**, 95–99 (2009). URL http://dx.doi.org/10.1038/nphys1153.

[63] Chang, D., Safavi-Naeini, A. H., Hafezi, M. & Painter, O. Slowing and stopping light using an optomechanical crystal array. *New J. Phys.* **13**, 023003 (2011).

[64] Michael, C. P., Borselli, M., Johnson, T. J., Chrystal, C. & Painter, O. An optical fiber-taper probe for wafer-scale microphotonic device characterization. *Opt. Express* **15**, 4745–4752 (2007). URL http://www.opticsexpress.org/abstract.cfm?URI=oe-15-8-4745.

[65] Eichenfield, M., Camacho, R., Chan, J., Vahala, K. J. & Painter, O. A picogram- and nanometre-scale photonic-crystal optomechanical cavity. *Nature* **459**, 550–555 (2009). URL http://dx.doi.org/10.1038/nature08061.

[66] Lee, D. *et al.* Multimode optomechanical dynamics in a cavity with avoided crossings. *Nat. Commun.* **6**, 6232 (2015). URL http://www.nature.com/ncomms/2015/150224/ncomms7232/full/ncomms7232.html#f1.

[67] Walls, D. F. & Milburn, G. J. *Quantum Optics* (Springer, 1994).

[68] Fano, U. Effects of configuration interaction on intensities and phase shifts. *Phys. Rev.* **124**, 1866–1878 (1961). URL http://link.aps.org/doi/10.1103/PhysRev.124.1866.

[69] Geerlings, K. *et al.* Improving the quality factor of microwave compact resonators by optimizing their geometrical parameters. *Applied Physics Letters* **100** (2012). URL http://scitation.aip.org/content/aip/journal/apl/100/19/10.1063/1.4710520.

[70] Marquardt, F., Chen, J. P., Clerk, A. A. & Girvin, S. M. Quantum theory of cavity-assisted sideband cooling of mechanical motion. *Phys. Rev. Lett.* **99**, 093902 (2007).

[71] Dobrindt, J. M., Wilson-Rae, I. & Kippenberg, T. J. Parametric Normal-Mode Splitting in Cavity Optomechanics. *Phys. Rev. Lett.* **101**, 263602 (2008).

[72] Rocheleau, T. *et al.* Preparation and detection of a mechanical resonator near the ground state of motion. *Nature* **463**, 72–75 (2010). URL http://dx.doi.org/10.1038/nature08681.

[73] Fink, J. M. *et al.* Quantum-to-classical transition in cavity quantum electrodynamics. *Phys. Rev. Lett.* **105**, 163601 (2010). URL `http://prl.aps.org/abstract/PRL/v105/i16/e163601`.

[74] Camacho, R. M., Chan, J., Eichenfield, M. & Painter, O. Characterization of radiation pressure and thermal effects in a nanoscale optomechanical cavity. *Optics Express* **17**, 15726–15735 (2009).

[75] Grutter, K. E., Davanco, M. I. & Srinivasan, K. Slot-mode optomechanical crystals: a versatile platform for multimode optomechanics. *Optica* **2**, 994–1001 (2015).

[76] Sonnet Software Inc., http://www.sonnetsoftware.com/.

[77] Mohan, S., del Mar Hershenson, M., Boyd, S. & Lee, T. Simple accurate expressions for planar spiral inductances. *Solid-State Circuits, IEEE Journal of* **34**, 1419–1424 (1999).

[78] Pitanti, A. *et al.* Strong opto-electro-mechanical coupling in a silicon photonic crystal cavity. *Opt. Express* **23**, 3196–3208 (2015).

[79] Yan, G.-Z., Chan, P. C., Hsing, I.-M., Sharma, R. K. & Sin, J. An improved tmah si-etching solution without attacking exposed aluminum. In *Micro Electro Mechanical Systems, 2000. MEMS 2000. The Thirteenth Annual International Conference on*, 562–567 (2000).

[80] Fujitsuka, N., Hamaguchi, K., Funabashi, H., Kawasaki, E. & Fukada, T. Aluminum protected silicon anisotropic etching technique using tmah with an oxidizing agent and dissolved si. *R&D Review of Toyota CRDL* **39** (2004).

[81] Teufel, J. D., Harlow, J. W., Regal, C. A. & Lehnert, K. W. Dynamical Backaction of Microwave Fields on a Nanomechanical Oscillator. *Phys. Rev. Lett.* **101**, 197203 (2008).

[82] Aspelmeyer, M., Kippenberg, T. J. & Marquardt, F. Cavity optomechanics. *Rev. Mod. Phys.* **86**, 1391–1452 (2014). URL `http://link.aps.org/doi/10.1103/RevModPhys.86.1391`.

[83] Safavi-Naeini, A. H. *et al.* Electromagnetically induced transparency and slow light with optomechanics. *Nature* **472**, 69–73 (2011).

[84] Teufel, J. D. *et al.* Circuit cavity electromechanics in the strong-coupling regime. *Nature* **471**, 204–208 (2011).

[85] Dobrindt, J. M. & Kippenberg, T. J. Theoretical analysis of mechanical displacement measurement using a multiple cavity mode transducer. *Phys. Rev. Lett.* **104**, 033901 (2010). URL http://link.aps.org/doi/10.1103/PhysRevLett.104.033901.

[86] Sarabi, B., Ramanayaka, A. N., Burin, A. L., Wellstood, F. C. & Osborn, K. D. Spectroscopy of random two-level systems in insulating films. arXiv:1501.05865 (2015).

[87] Private communication with John Teufel (NIST).

[88] Rocheleau, T. *et al.* Preparation and detection of a mechanical resonator near the ground state of motion. *Nature* **463**, 72–75 (2010).

[89] Safavi-Naeini, A. H. *et al.* Laser noise in cavity-optomechanical cooling and thermometry. *New J. Phys.* **15**, 035007 (2013).

[90] Wollman, E. E. *et al.* Quantum squeezing of motion in a mechanical resonator. *Science* **349**, 952–955 (2015).

[91] Pirkkalainen, J. M., Damskägg, E., Brandt, M., Massel, F. & Sillanpää, M. A. Squeezing of quantum noise of motion in a micromechanical resonator. *Phys. Rev. Lett.* **115**, 243601 (2015).

[92] Grabovskij, G. J., Peichl, T., Lisenfeld, J., Weiss, G. & Ustinov, A. V. Strain tuning of individual atomic tunneling systems detected by a superconducting qubit. *Science* **338**, 232–234 (2012). URL http://www.sciencemag.org/content/338/6104/232.abstract. http://www.sciencemag.org/content/338/6104/232.full.pdf.

[93] Blais, A. *et al.* Quantum-information processing with circuit quantum electrodynamics. *Phys. Rev. A* **75**, 032329 (2007). URL http://pra.aps.org/abstract/PRA/v75/i3/e032329.

[94] Schuster, D. I. *et al.* AC Stark shift and dephasing of a superconducting qubit strongly coupled to a cavity field. *Phys. Rev. Lett.* **94**, 123602 (2005). URL http://link.aps.org/abstract/PRL/v94/e123602.

[95] Safavi-Naeini, A. H., Alegre, T. P. M., Winger, M. & Painter, O. Optomechanics in an ultrahigh-Q slotted 2D photonic crystal cavity. *Appl. Phys. Lett.* **97**, 181106 (2010).

[96] Winger, M. *et al.* A chip-scale integrated cavity-electro-optomechanics platform. *Opt. Express* **19**, 24905–24921 (2011). URL `http://www.opticsexpress.org/abstract.cfm?URI=oe-19-25-24905`.

[97] Eichenfield, M., Chan, J., Camacho, R. M., Vahala, K. J. & Painter, O. Optomechanical crystals. *Nature* **462**, 78–82 (2009). URL `http://dx.doi.org/10.1038/nature08524`.

[98] SOITEC, http://www.soitec.com/.

[99] Kippenberg, T. J., Rokhsari, H., Carmon, T., Scherer, A. & Vahala, K. J. Analysis of radiation-pressure induced mechanical oscillation of an optical microcavity. *Phys. Rev. Lett.* **95**, 033901 (2005).

[100] Grudinin, I. S., Lee, H., Painter, O. & Vahala, K. J. Phonon laser action in a tunable two-level system. *Phys. Rev. Lett.* **104**, 083901 (2010).

[101] Cohen, J. D. *et al.* Phonon counting and intensity interferometry of a nanomechanical resonator. *Nature* **520**, 522–525 (2015).

[102] Gao, J. *The Physics of Superconducting Microwave Resonators*. Ph.D. thesis, California Institute of Technology (2008).

[103] Gao, J. *et al.* Experimental evidence for a surface distribution of two-level systems in superconducting lithographed microwave resonators. *Appl. Phys. Lett.* **92**, 152505 (2008). URL `http://link.aip.org/link/?APL/92/152505/1`.

[104] Wisbey, D. S. *et al.* Effect of metal/substrate interfaces on radio-frequency loss in superconducting coplanar waveguides. *J. Appl. Phys.* **108**, 093918 (2010). URL `http://link.aip.org/link/?JAP/108/093918/1`.

[105] Bruno, A. *et al.* Reducing intrinsic loss in superconducting resonators by surface treatment and deep etching of silicon substrates. *App. Phys. Lett.* **106**, 182601 (2015).

[106] Cochran, J. F. & Mapother, D. E. Superconducting transition in aluminum. *Phys. Rev.* **111**, 132–142 (1958).

[107] Wang, Y.-D. & Clerk, A. A. Using dark modes for high-fidelity optomechanical quantum state transfer. *New Journal of Physics* **14**, 105010 (2012). URL `http://stacks.iop.org/1367-2630/14/i=10/a=105010`.

[108] Bochmann, J., Vainsencher, A., Awschalom, D. D. & Cleland, A. N. Nanomechanical coupling between microwave and optical photons. *Nature Physics* **9**, 712–716 (2013).

[109] Bagci, T. *et al.* Optical detection of radio waves through a nanomechanical transducer. *Nature* **507**, 81–85 (2014). URL `http://dx.doi.org/10.1038/nature13029`.

[110] Černotík, O. & Hammerer, K. Measurement-induced long-distance entanglement of superconducting qubits using optomechanical transducers. *arXiv:1512.00768* (2015).

[111] Weis, S. *et al.* Optomechanically Induced Transparency. *Science* **330**, 1520–1523 (2010).

[112] Perahia, R., Cohen, J. D., Meenehan, S., Alegre, T. P. M. & Painter, O. Electrostatically tunable optomechanical "zipper" cavity laser. *Applied Physics Letters* **97**, 191112 (2010). URL `http://link.aip.org/link/?APL/97/191112/1`.

[113] Safavi-Naeini, A. H. *et al.* Squeezed light from a silicon micromechanical resonator. *Nature* **500**, 185–189 (2013).

[114] Meenehan, S. M. *et al.* Pulsed excitation dynamics of an optomechanical crystal resonator near its quantum ground-state of motion. *arXiv:1503.05135* (2015).

[115] Balram, K. C., Davanco, M. I., Song, J. D. & Srinivasan, K. Coherent coupling between radiofrequency, optical and acoustic waves in piezo-optomechanical circuits. *Nature Photon.* **10**, 346–352 (2016).

[116] Fang, K., Matheny, M. H., Luan, X. & Painter, O. Optical transduction and routing of microwave phonons in cavity-optomechanical circuits. *Nature Photonics* **10**, 489 (2016). URL `http://dx.doi.org/10.1038/nphoton.2016.107http:`

//10.0.4.14/nphoton.2016.107https://www.nature.com/articles/nphoton.2016.107{#}supplementary-information.

[117] Fang, K. *et al.* Generalized non-reciprocity in an optomechanical circuit via synthetic magnetism and reservoir engineering. *Nature Physics* **13**, 465 (2017). URL http://dx.doi.org/10.1038/nphys4009http://10.0.4.14/nphys4009https://www.nature.com/articles/nphys4009{#}supplementary-information.

[118] Patel, R. N. *et al.* Single-mode phononic wire. *Phys. Rev. Lett.* **121**, 040501 (2018).

[119] Schoelkopf, R. J. & Girvin, S. M. Wiring up quantum systems. *Nature* **451**, 664 (2008).

[120] LaHaye, M. D., Suh, J., Echternach, P. M., Schwab, K. C. & Roukes, M. L. Nanomechanical measurements of a superconducting qubit. *Nature* **459**, 960–964 (2009). URL http://dx.doi.org/10.1038/nature08093.

[121] O'Connell, A. D. *et al.* Quantum ground state and single-phonon control of a mechanical resonator. *Nature* **464**, 697 (2010). URL http://dx.doi.org/10.1038/nature08967.

[122] Pirkkalainen, J.-M. *et al.* Hybrid circuit cavity quantumelectrodynamics with a micromechanical resonator. *Nature* **494**, 211–215 (2013).

[123] Gustafsson, M. V. *et al.* Propagating phonons coupled to an artificial atom. *Science* **346**, 207–211 (2014). URL http://www.sciencemag.org/content/346/6206/207.abstract.

[124] Chu, Y. *et al.* Quantum acoustics with superconducting qubits. *Science* (2017). URL http://science.sciencemag.org/content/early/2017/09/20/science.aao1511.

[125] Manenti, R. *et al.* Circuit quantum acoustodynamics with surface acoustic waves. *Nat. Commun.* **8**, 975 (2017).

[126] Satzinger, K. J. *et al.* Quantum control of surface acoustic wave phonons. *arXiv:1804.07308* (2018).

[127] Moores, B. A., Sletten, L. R., Viennot, J. J. & Lehnert, K. Cavity quantum acoustic device in the multimode strong coupling regime. *Phys. Rev. Lett.* **120**, 227701 (2018).

[128] Arrangoiz-Arriola, P. *et al.* Coupling a superconducting quantum circuit to a phononic crystal defect cavity. *arXiv:1804.03625* (2018).

[129] Eom, C.-B. & Trolier-McKinstry, S. Thin-film piezoelectric mems. *MRS Bulletin* **37**, 1007–1017 (2012).

[130] Piazza, G., Felmetsger, V., Muralt, P., III, R. H. O. & Ruby, R. Piezoelectric aluminum nitride thin films for microelectromechanical systems. *MRS Bulletin* **37**, 1051–1061 (2012).

[131] Han, X., Zou, C.-L. & Tang, H. X. Multimode strong coupling in superconducting cavity piezoelectromechanics. *Phys. Rev. Lett.* **117**, 123603 (2016). URL `https://link.aps.org/doi/10.1103/PhysRevLett.117.123603`.

[132] Arrangoiz-Arriola, P. & Safavi-Naeini, A. Engineering interactions between superconducting qubits and phononic nanostructures. *Phys. Rev. A* **94**, 063864 (2016).

[133] Phillips, W. A. Tunneling states in amorphous solids. *Journal of Low Temperature Physics* **7**, 351–360 (1972).

[134] Keller, A. J. *et al.* Al transmon qubits on silicon-on-insulator for quantum device integration. *Appl. Phys. Lett.* **111**, 042603 (2017).

[135] Maldovan, M. Sound and heat revolutions in phononics. *Nature* **503**, 209–217 (2013).

[136] Fink, J. M. *et al.* Quantum electromechanics on silicon nitride nanomembranes. *Nat. Commun.* **7**, 12396 (2016).

[137] Safavi-Naeini, A. H. & Painter, O. Design of optomechanical cavities and waveguides on a simultaneous bandgap phononic-photonic crystal slab. *Opt. Express* **18**, 14926–14943 (2010).

[138] Zhang, Y., Moser, J., Güttinger, J., Bachtold, A. & Dykman, M. I. Interplay of driving and frequency noise in the spectra of vibrational systems. *Phys. Rev. Lett.* **113**, 255502 (2014). URL `https://link.aps.org/doi/10.1103/PhysRevLett.113.255502`.

[139] Zhang, Y. & Dykman, M. I. Spectral effects of dispersive mode coupling in driven mesoscopic systems. *Phys. Rev. B* **92**, 165419 (2015). URL `https://link.aps.org/doi/10.1103/PhysRevB.92.165419`.

[140] Meenehan, S. M. *et al.* Pulsed excitation dynamics of an optomechanical crystal resonator near its quantum ground state of motion. *Phys. Rev. X* **5**, 041002 (2015).

[141] Stannigel, K., Rabl, P., Sørensen, A. S., Zoller, P. & Lukin, M. D. Optomechanical transducers for long-distance quantum communication. *Phys. Rev. Lett.* **105**, 220501 (2010). URL `http://link.aps.org/doi/10.1103/PhysRevLett.105.220501`.

[142] Bogaerts, W. *et al.* Nanophotonic waveguides in silicon-on-insulator fabricated with cmos technology. *Journal of Lightwave Technology* **23**, 401–412 (2005).

[143] Sekoguchi, H., Takahashi, Y., Asano, T. & Noda, S. Photonic crystal nanocavity with a q-factor of $\sim$9 million. *Opt. Express* **22**, 916–924 (2014).

[144] Michael, C. P. *et al.* Wavelength- and material-dependent absorption in gaas and algaas microcavities. *App. Phys. Lett.* **90**, 051108 (2007).

[145] Weinstein, A. J. *et al.* Observation and interpretation of motional sideband asymmetry in a quantum electromechanical device. *Phys. Rev. X* **4**, 041003 (2014). URL `http://link.aps.org/doi/10.1103/PhysRevX.4.041003`.

[146] Safavi-Naeini, A. H. & Painter, O. Proposal for an optomechanical traveling wave phonon-photon translator. *New J. Phys.* **13**, 013017 (2011).

[147] de Visser, P. *et al.* Microwave-induced excess quasiparticles in superconducting resonators measured through correlated conductivity fluctuations. *App. Phys. Lett.* **100**, 162601 (2012).

[148] Grünhaupt, L. *et al.* Quasiparticle dynamics in granular aluminum close to the superconductor to insulator transition. *arXiv:1802.01858* (2018).

[149] Goldie, D. J. & Withington, S. Non-equilibrium superconductivity in quantum-sensing superconducting resonators. *Supercond. Sci. Technol.* **26**, 015004 (2013).

[150] Barends, R. *et al.* Reduced frequency noise in superconducting resonators. *Appl. Phys. Lett.* **97**, 033507 (2010). URL `http://link.aip.org/link/?APL/97/033507/1`.

[151] Samkharadze, N. *et al.* High-kinetic-inductance superconducting nanowire resonators for circuit qed in a magnetic field. *Phys. Rev. Applied* **5**, 044004 (2016). URL `https://link.aps.org/doi/10.1103/PhysRevApplied.5.044004`.

[152] Rouxinol, F. *et al.* Measurements of nanoresonator-qubit interactions in a hybrid quantum electromechanical system. *Nanotechnology* **27**, 364003 (2016). URL `http://stacks.iop.org/0957-4484/27/i=36/a=364003`.

[153] Clerk, A. A., Devoret, M. H., Girvin, S. M., Marquardt, F. & Schoelkopf, R. J. Introduction to quantum noise, measurement, and amplification. *Rev. Mod. Phys.* **82**, 1155–1208 (2010).

Appendix A

Mathematical Conventions

A.1 Fourier Transform

We use the following convention for the Fourier transform. Given an operator $\hat{A}$ we define

$$\hat{A}(t) = \frac{1}{\sqrt{2\pi}} \int_{-\infty}^{+\infty} d\omega e^{-i\omega t} \hat{A}(\omega) \tag{A.1}$$

$$\hat{A}(\omega) = \frac{1}{\sqrt{2\pi}} \int_{-\infty}^{+\infty} dt e^{i\omega t} \hat{A}(t) \tag{A.2}$$

$$\hat{A}^{\dagger}(\omega) = \frac{1}{\sqrt{2\pi}} \int_{-\infty}^{+\infty} dt e^{i\omega t} \hat{A}^{\dagger}(t) \tag{A.3}$$

$$\left(\hat{A}(\omega)\right)^{\dagger} = \hat{A}^{\dagger}(-\omega). \tag{A.4}$$

A.2 Definition of Spectral Densities

The power spectral density of an operator $\hat{A}$ can be written as

$$S_{AA}(t) = \int_{-\infty}^{+\infty} d\tau e^{i\omega\tau} \left\langle \hat{A}^{\dagger}(t+\tau)\hat{A}(t) \right\rangle, \tag{A.5}$$

and utilizing Fourier transform defined above, we can re-define the power spectral density of an operator $\hat{A}$ in terms of frequency as

$$S_{AA}(\omega) = \int_{-\infty}^{+\infty} d\omega' \left\langle \hat{A}^{\dagger}(\omega)\hat{A}(\omega') \right\rangle. \tag{A.6}$$

Thus, we can write the auto-correlation of the detected normalized field amplitude (or the photo current) $\hat{I}(t) = \hat{a}_{\text{out}}(t) + \hat{a}^{\dagger}_{\text{out}}(t)$ as

$$S_{II} = \int_{-\infty}^{+\infty} d\omega' \left\langle \left(\hat{a}_{\text{out}}(\omega) + \hat{a}^{\dagger}_{\text{out}}(\omega) \right) \left(\hat{a}_{\text{out}}(\omega') + \hat{a}^{\dagger}_{\text{out}}(\omega') \right) \right\rangle . \tag{A.7}$$

A.3 Some Useful Commutation Relationships

$$\dot{\hat{A}}(t) = \frac{i}{\hbar} \left[\hat{H}, \hat{A}(t) \right] \tag{A.8}$$

$$\left[\hat{a}, \hat{a}^{\dagger} \right] = 1 \tag{A.9}$$

$$\left[\hat{a}^{\dagger}\hat{a}, \hat{a} \right] = -\hat{a} \tag{A.10}$$

$$\left[\hat{a}\hat{a}^{\dagger}, \hat{a} \right] = \hat{a}^{\dagger} \tag{A.11}$$

Appendix B

Dilution Fridge Experimental Setup

The cryogenic setup used for the experiments in this thesis is equipped with cryogenic microwave components that route the microwave signal from room temperature to the cryogenic base environment at 10 mK temperature and back. Such a cryogenic environment requires careful selection of microwave components that are compatible with the cryogenic environments and their quality are not degraded due to the low temperature of the environment. Moreover, it is important to consider heat-loads and the microwave power dissipation at each stage to ensure the proper operation of the DR (dilution refrigerator).

In this appendix, I mainly focus on noise reduction of the attenuation microwave input signal and subsequent low noise amplification of the measured response from the device under test (DUT) to compensate insertion losses and the input attenuation. At room temperature, all microwave signals from the RF-sources and the vector network analyzer are combined with a ZC4PD-153-S+ power divider and combiner before entering the cryogenic part of the microwave setup. With RF semi-rigid coaxial cables and high vacuum feed through connectors, the microwave signals are routed to the 10mK base stage. It is important to attenuated the microwave signals gradually at each stage, to attenuate the thermal noise before the DUT at the 10 mK base stage. However, the attenuation of the signal must be done gradually such that the dissipated power at each stage of the DR does not exceed the cooling power at each stage. Additionally, the cables material are chosen such that they do not make a thermal contact between each stage of the DR unit.

After filtering of the thermal noise, microwave signals are forwarded to the sample via RADITEK cryogenic circulator with 8-12 GHz bandwidth. RF circulators are magnetic passive non-reciprocal devices which transmit the signals in a circular way ($1 \rightarrow 2$, $2 \rightarrow 3$, $3 \rightarrow 1$), and the

reverse direction is blocked with an isolation of about 15-20 dB. We use a flexible cable and MMPX microwave connectors to send the signal to PCB with 50Ω impedance coplanar waveguides. The waveguides are wire bonded to another 50 Ω coplanar waveguides on the sample. To couple to microwave devices on the chip, we extend the center conductor of the microwave feed line and short it to the ground near the microwave resonators. This provides inductive coupling between the microwave feed-line and the microwave resonator. The response from the microwave resonator is reflected back and gets separated from the input signal via the microwave circulator and is routed to the output port of the DR.

On the output side, we use another circulator for isolating the sample from the noise coming from the output port from the higher stages of the DR. Moreover, due to low power levels of the microwave response from the sample, it is important to avoid any lossy equipment before amplifying the response from the sample. We use NbTi superconducting cables to directly route the microwave signals from the output of the circulator to 4K stage. The signal is then amplified using the Caltech CIICRYO1-12A HEMT amplifier. The HEMT amplifier used here has a gain of 31 dB and an effective noise temperature of 4 K between 8-12 GHz microwave frequency. The signal is then routed to outside of the DR unit and gets amplified again to compensate for the input attenuation of the input signal. For electromechanics experiments, due to the requirement of strong microwave drive tone to enhance the electromechanical interaction, we need to cancel the pump before the room temperature amplifier to operate at its dynamic range and avoid spurious microwave responses on the microwave signal. In order to suppress spurious response peaks for high drive power measurements, we cancel the high drive power tone by adding a phase and amplitude adjusted part of the pump tone to the output signal before the room temperature amplifier. Depending on the specific measurement the response is routed to a microwave switch to distribute the signal to either the spectrum analyzer or the second port of the vector network analyzer.

B.1 Input Thermal and Phase noise

The noise affecting our experiments has a broad variety of sources. In this section, I discuss only the most relevant noise types, which are Thermal John-Nyquist and Phase noise. Other source of noise such as electronic $1/f$ noise are usually small at 8-12 GHz microwave frequencies. The phase

noise results from the frequency jitter of the microwave sources. The typical phase noise of the microwave sources used in our experimental setup is below -120 dBc/Hz for carrier offset of about 1 MHz. Even for the highest power level of microwave drive tone and relative detuning of 4 - 6 MHz from the microwave resonator, the phase noise is about -200 dBm and negligible to affect the measurements. On the other hand, the effects of thermal noise on the sample can only be mitigated by careful attenuation of the input signal and amplification of the output microwave response.

Every lossy linear system introduces thermal nose from an ambient environment. For a single mode attenuator in thermal equilibrium with a reservoir, the thermal occupancy is given by Bose-Einstein relation:

$$\mathcal{N}_{th} = \frac{\hbar\omega}{e^{\hbar\omega/k_B T} - 1}, \tag{B.1}$$

where T is the temperature of the ambient environment. For a lossy system with a bosonic mode the input-output relation gives [153]

$$S_{out} = \frac{1}{L} S_{in} + \left(1 - \frac{1}{L}\right) \mathcal{N}_{th}. \tag{B.2}$$

In our experimental setup the cables, feed-through connectors, attenuators and circulators introduce thermalized losses and thermal noise. The relation introduced above allows us to estimate the degree of thermalization in each stage of the dilution refrigerator and the additional thermal noise. Taking into account the losses from the cables, feed throughs, attenuators and circulators, the thermal noise from 300 K at microwave frequency of $\omega/2\pi = 10$ GHz is about -226 dBm/Hz resulting in average thermal noise occupancy of $\bar{n}_{th} \approx 0.004$ quanta, allowing single photon operations at the MXC plate ($T_f = 10$ mK).

B.2 Output Amplifiers

The additional noise introduced by an amplifier in the linear operation can be regarded similar to Eq. (B.2), where we replace the losses by gain $G = 1/L$. The additional noise from the amplifier is given by

$$S_{out} = G S_{in} + (G - 1)\mathcal{N}_{add}, \tag{B.3}$$

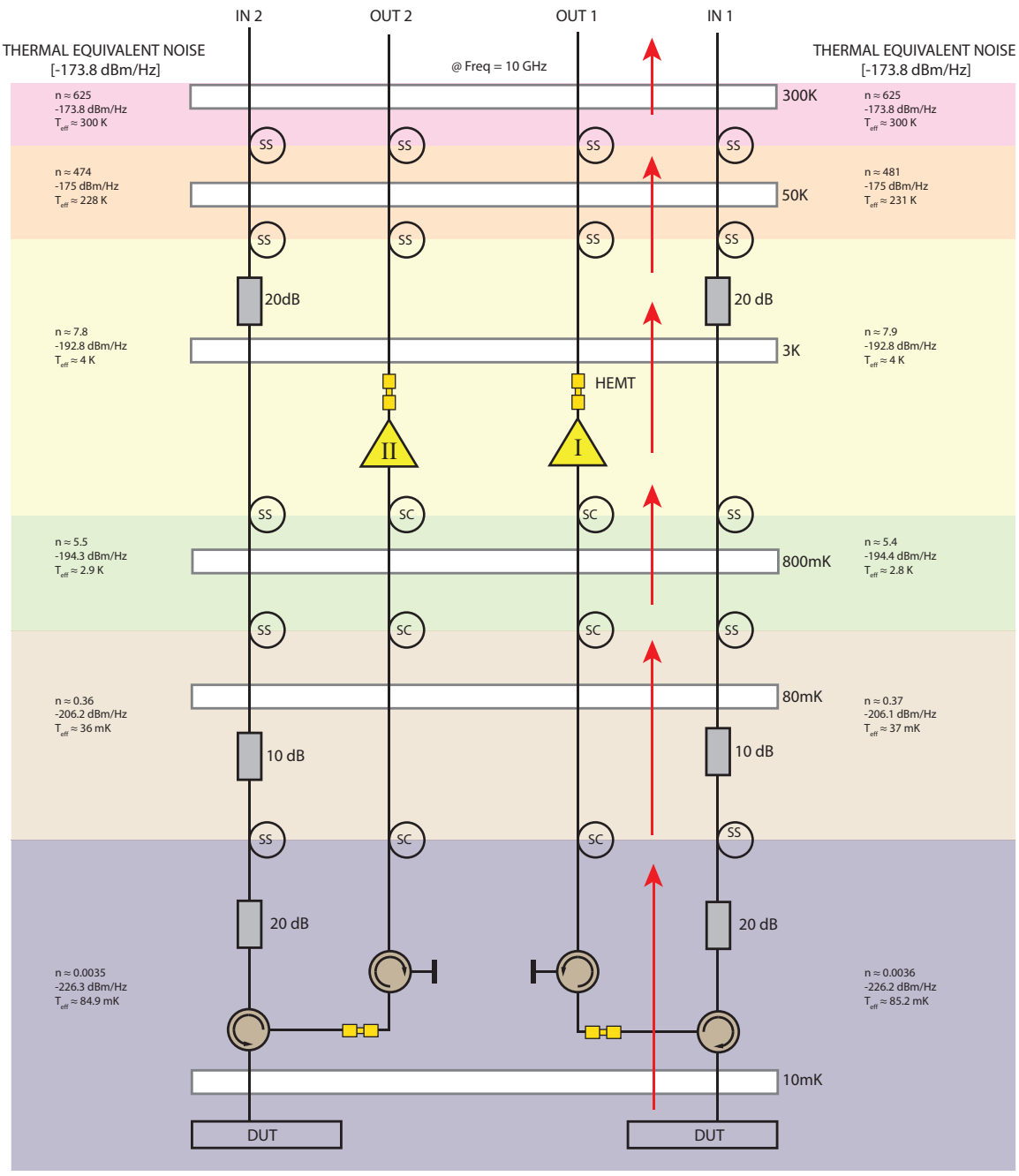

Figure B.1: Schematic setup of the dilution refrigerator. The colored boxes indicate the various dilution refrigerator temperature stages. Estimated thermal microwave noise from input lines in units of dBm/Hz and equivalent noise quanta is is written for each temperature stages.

where $\mathcal{N}_{add}$ contains both the contribution from the thermal noise and the electronic noise from the amplifier. The HEMT amplifier in our setup has an effective noise temperature of 4 K for microwave frequencies 8-12 GHz.